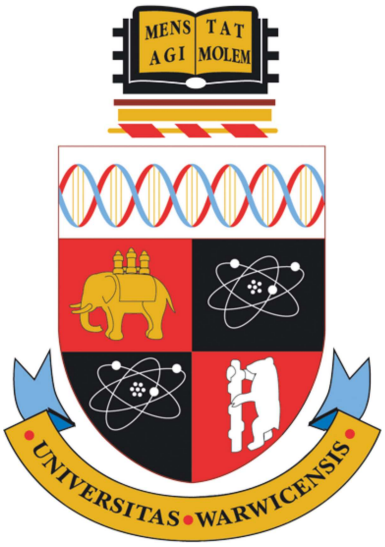

Control of the Offshore Wind Turbine and Its Grid Integration

by

Shuyue Lin

Thesis

Submitted to the University of Warwick

for the degree of

Doctor of Philosophy

School of Engineering

Nov 2018

Contents

List of Tables

List of Figures

Acknowledgments

I would like to express my most sincere gratitude to my supervisor Prof. Xiaowei Zhao, who brought me to the world of academic research. His patient guidance, kind encouragement, and insightful ideas supported me to overcome every difficulty during my 4-year PhD life. The discussion with him were always pleasant, inspiring and enriching, which instructed me to become an efficient researcher. I am so lucky to have him as my supervisor. Nothing would be possible without his assistance. Besides, I would like to express my appreciation to Prof. George Weiss, Dr. Xin Tong, Mr. Pengyuan Qi and Mr. Jun Lin for their cooperation and discussion in my research. I would also like to present my thanks to Mr. Ian Griffith and Mr. Jonathan Meadows for their support in my experiment.

My PhD experience would not be enjoyable and memorable without the support and friendship from my friends and my research group. I am very fortunate to harvest the friendship from Miss Yumeng Song, Miss Shanshan Wu, Mr. Guanchen Wu, Miss Gina Jiang, Dr Yi Lu, Dr. Song Qiu and his wife Ms Fanlin Zhou, Dr. Hu Yuan and his wife Ms Weixian Xu, and all the members in my research group: Dr. Xin Tong, Mr. Pengyuan Qi, Mr. Xing Wei, Dr. Mohammed Edrah, Dr. Xiuxing Yin, Dr. Juan Li, Mr. Jincheng Zhang and Dr. Yinan Wang.

Finally, I would like to express my infinite gratitude and unreserved love to my family, who provided me persistent support during these four years, especially my parents Mr Hongqi Lin and Ms Rongzhuang Qiu. Also, I would like to express my endless miss to my grandfather, Mr. Qiyu Qiu, who still cared about my PhD life when he was seriously ill in bed.

Declarations

This thesis is submitted to the University of Warwick in support of my application for the degree of Doctor of Philosophy. It has been composed by myself and has not been submitted in any previous application for any degree.

Parts of this thesis have been published by the author:

Journal (Peer Reviewed)

1. **S. Lin**, X. Tong, X. Zhao, G. Weiss, The Parallel Virtual Infinite Capacitor Applied to DC-Link Voltage Filtering for Wind Turbines, *Energies,* 2018, Vol. 11, No. 7, pp. 1-19.

2. **S. Lin**, X. Zhao, X. Tong, Feasibility studies of a Converter-free Grid-connected Hydrostatic Wind Turbine, under review, 2018.

3. **S. Lin**, P. Qi, X. Zhao, Power Generation Control of a Hydrostatic Wind Turbine Implemented by Model-free Adaptive Control Scheme, under review, 2018.

Conference (Peer Reviewed)

1. **S. Lin**, X. Tong, X. Zhao, G. Weiss, Application of a Parallel Virtual Infinite Capacitor to DC-link Voltage Filtering for a Doubly Fed Induction Wind Generator, in *18th IEEE International Conference on Environment and Electrical Engineering & 2nd IEEE Industrial and Commercial Power System Europe (EEEIC/I&CPS Europe)*, IEEE, Jun. 2018, Palermo, Italy.

2. **S. Lin**, P. Qi, J. Lin, X. Zhao, G. Weiss, L. Ran, Experimental Ripple Suppression Performance of a Virtual Infinite Capacitor, in *22nd International Conference on Applied Electronics (AE)*, IEEE, Sep. 2017, Pilsen, Czech Republic.

3. **S. Lin**, J. Lin, G. Weiss, X. Zhao, Control of a virtual infinite capacitor used to stabilize the output voltage of a PFC, in *IEEE International Conference on Science of Electrical Engineering (ICSEE)*, IEEE, Nov. 2016, Eilat, Israel.

Abstract

This thesis investigates the way to reduce the maintenance cost and increase the life cycle of the offshore wind turbines, as in the offshore case maintenance is highly difficult and expensive.

Firstly, we study the possibility to replace the vulnerable and expensive DC-link capacitor in wind power integration system by the virtual infinite capacitor (VIC), which is a power electronic circuit functioning as a large filtering capacitor. We propose a control algorithm for the VIC. Before applying it to the wind power system, we firstly test it in a simple power factor compensator (PFC) as the output filter capacitor. The simulation results show the effective filtering performance of VIC in low-frequency range. Then, we validate it experimentally by directly injecting the DC voltage together with a 50 Hz ripples to the VIC. The VIC successfully eliminates the ripple and extracts the DC voltage at the output terminals. Besides, the experiment performances are highly consistent with the corresponding simulations, which demonstrates the possibility to use VIC to replace the DC-link capacitor in wind power integration system and use it in other industrial systems.

Since the VIC mainly filters the ripple in low frequency range while the DC-link voltage usually includes ripples in two distinct frequency ranges, we further develop it into the parallel virtual infinite capacitor (PVIC), aiming to suppress the voltage ripple in a wider frequency range. The PVIC is applied to replace the DC-link capacitor in wind turbine grid integration system. The simulations are conducted under different grid conditions with turbulent wind input. The results show that the PVIC provides

much better voltage suppression performance than the equivalent DC-link capacitor, which facilitates the power generation control under normal operations and reduces the risks of converter failure under grid faults. In this way, the PVIC proves to be a great solution to substitute the vulnerable DC-link voltage in the offshore wind turbine power integration system.

The wind power conversion system from the generator to the grid is composed of a DC-link capacitor and two back-to-back power converters. Though the application of PVIC removes the fragile DC-link capacitor in the power conversion system, the power converters are also fragile and expensive. In addition, the existence of power converters decouples the generator with the grid, which hinders the direct inertia support and frequency regulations from wind turbines. It would be desirable to completely remove the whole power conversion system. Hydrostatic wind turbine (HWT) may provide a suitable solution. The HWT is a wind turbine using hydrostatic transmission (HST) to replace the original heavy and fragile gearbox. The HST can provide the 'continuously variable gearbox ratio' , which allows HWT to be connected to a synchronous generator (SG) and then directly to the grid. We propose a coordinated control scheme for the HWT. The simulations are conducted with turbulent wind under variable system loads. The results indicate that with the proposed coordinated control system, the HWT (without power converters) provides efficient frequency support to the grid, which shows it is a promising solution for the future offshore wind power system.

Finally, we consider to further reduce the maintenance cost and improve the performance of the HWT by using a new and novel control algorithm called model-free adaptive control (MFAC). It is applied to both torque control and pitch control of the HWT. Their control performances are compared to some of the existing algorithms. The simulation results demonstrate that the MFAC controller has much better tracking and disturbance rejection performances than the existing algorithms which can increase the fatigue life of the wind turbine and reduce the maintenance cost.

Abbreviations

AC alternating current

AGC automatic generation control

AW antiwindup

BESS battery energy storage system

CAES compressed air energy storage

CCM continuous conduction mode

CRM critical conduction mode

DC direct current

DCM discontinuous conduction mode

DD digital displacement

DEL damage-equivalent load

DFIG doubly fed induction generator

DLL dynamic-link-library

DSP digital signal processor

ESS energy storage system

FAST Fatigue, Aerodynamics, Structures, and Turbulence

FESS flywheel energy storage system

GCD greatest common divisors

GCRD greatest common right divisor

GHG greenhouse gas

GWEC Global Wind Energy Council

HAWT horizontal axis wind turbine

HESS hydrogen-based energy storage system

HF high frequency

HM hysteresis-modulation

HST hydrostatic transmission

HWT hydrostatic wind turbine

IEC International Electro-technical Commission

LF low frequency

LIDAR Light and Detection Ranging

LLC linearisation length constant

LPF low-pass filter

LWK Landwirtschaftskammer Schleswig-Holstein

MFAC model-free adaptive control

MPC model predictive control

MPPT maximum power point tracking

MTBF mean time between failure

MTTR mean time to repair, (or downtime)

NREL National Renewable Energy Laboratory

PCB printed circuit board

PES pneumatic energy storage

PFC power factor compensator

PFDL partial form dynamic linearisation

PG pseudo gradient

PI proportional-integral

PIAW gain scheduling PI controller with anti-windup

PHES pump hydro energy storage

PMSG permanent magnetic synchronous generator

p.u. per-unit

PV photovoltaics

PVIC parallel virtual infinite capacitor

RMS root-mean-square

SCES supercapacitor energy storage

SCIG squirrel-cage induction generator

SG synchronous generator

SISO single-input-single-output

SMC sliding mode controller

SoC state of charge

SVR support vector regression

ULF ultimate load factor

VAWT vertical axis wind turbine

VIC virtual infinite capacitor

VRFC virtual reference feedback control

WMEP Wissenschaftliches Mess- und Evaluierungsprogramm

WP WindPACT

WT wind turbine

ZCS zero current switching

ZVS zero voltage switching

Chapter 1

Introduction

1.1 Background

The fuel energy is believed to be the main contributor to the global warming and air pollution. To deal with the threats from the environment issues, we have seen a great improvement in the renewable energy technologies [146, 43]. The governments usually provide the policy support and encouragement to the renewable energy technologies and recognise it as the growth industries, which contribute to its fast development [55, 12, 27, 146, 40]. The renewable energy power generation also benefits from the clean energy policies in many countries and obtained a great growth in recent decades.

The renewable energy techniques in power generation are developed into a few categories, which includes bioenergy, wind, geothermal, solar photovoltaics (PV), solar thermal, and hydro [40, 67, 41]. Fig. 1.1 shows the installed capacity share by power-generating source in global renewable power market in 2017, where the wind energy is the largest renewable source [41]. As one of the most mature renewable energy technologies, the wind power generation enjoys the sustained and rapid development in recent years, which becomes a preferable solution for greenhouse gas (GHG) emission reductions in power generation industries. The 2017 Global Wind Report shows that the cumulative installed wind turbine capacity was over 539 GW by end of 2017, which covers over 5% of the electric power demand in the world [46]. Moreover, the wind power capacity is expected to rise to 840 GW in 2020 [158]. In some European countries such as Denmark, Portugal, Ireland and Germany, the wind power penetration rate has reached over 20% in 2017 [46]. Besides, in the 2017 World Energy Outlook [68], the wind power generation is predicted to take place of the fuel energy to become the leading source for power generation after 2030 in European Union, owing to the significant growth in both

onshore and offshore cases in recent years [68].

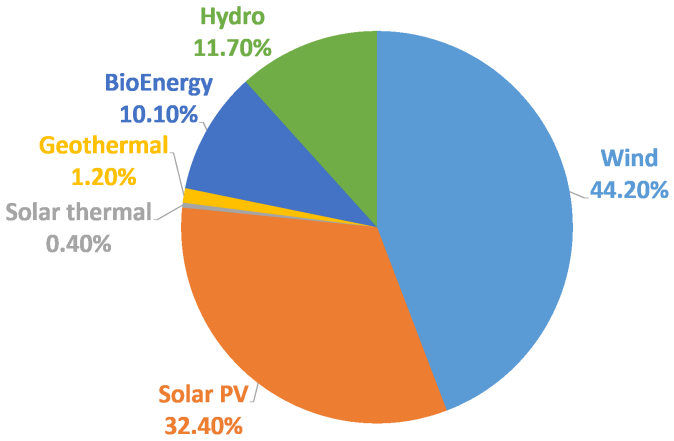

Figure 1.1: Installed capacity share by power-generating source in renewable power market globally in 2017 (%) [41].

1.1.1 Offshore wind power

Due to the limited land resources, exploring the offshore wind energy becomes an important strategy for human sustainable development. Here we list some advantages for the offshore wind power generation:

- The offshore wind speed is usually more steady and faster than onshore. It means the energy is more reliable and more power is available to be captured, which allows the increase in the wind turbine capacity, thus achieving more cost-effective operations [66, 103].
- The offshore wind energy is abundant and sustainable [66, 103].
- The electricity is usually in high demand in coastal areas where the land resources are usually expensive. It can be assisted by the local offshore wind plants [66, 103].
- Many job positions can be created by the offshore wind power industry [157].
- It can stimulate the local economic development without pollutant emissions [157].

Considering these advantages, the first offshore wind farm was installed in Denmark with a total capacity of 4.95 MW in 1991. After that, the offshore wind power

capacity grows enormously across the world [121]. According to the latest Global Offshore Wind Report by Global Wind Energy Council (GWEC) [47], till 2017, the total offshore wind farm capacity around the world reached 18,814 MW. Besides, many momentous progresses in offshore wind industries were achieved in 2017, such as increasingly larger turbines whose size boggles the mind, the worldwide rapid-expanding market with newcomers India, Brazil and Turkey, and a full 'zero subsidy' tender in the Netherlands [47]. See Fig. 1.2 for the global cumulative offshore wind capacity in 2017 [47]. It is clear that the offshore wind power generation enjoys a significant boost in cumulative capacity in 2017 (totally 4,334 MW), especially in Europe and China. The increasing offshore wind capacity and the gradual maturity of the offshore wind technology imply that the offshore wind is among the mainstream energy sources for power generations [47].

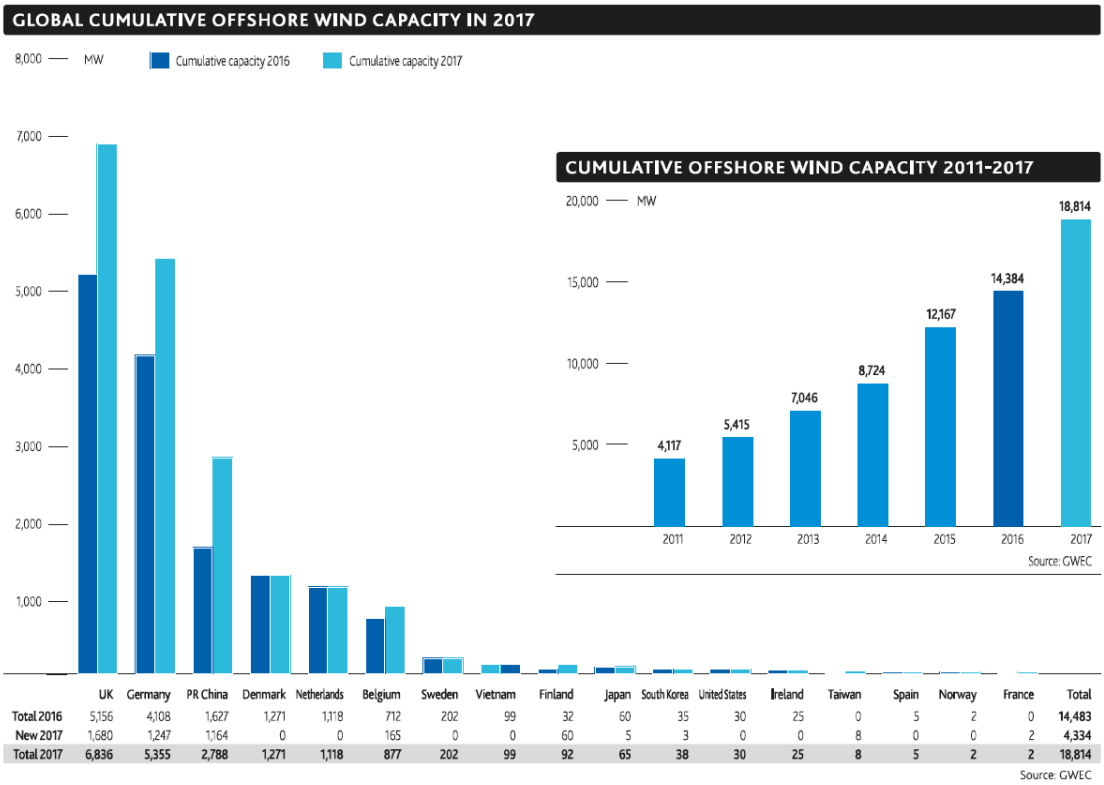

Figure 1.2: Global cumulative offshore wind capacity in 2017. This figure is taken from [47].

1.1.2 Power generation control of wind turbine

The wind turbines are divided into the horizontal and vertical axis designs, which is entitled as HAWT (horizontal axis wind turbine) and VAWT (vertical axis wind turbine) respectively. Now, the HAWT structure with 3 blades dominates the market [40]. See Fig. 1.3 for the major component in a 3-blade horizontal axis wind turbine.

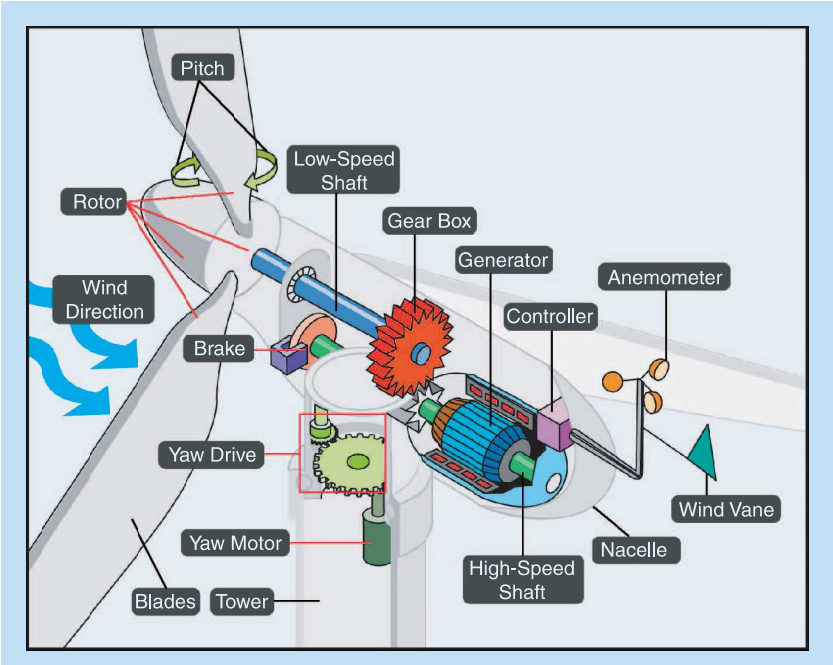

Figure 1.3: Major components of the wind turbine. This figure is taken from [69].

In wind power generation, wind blows the airfoil-shaped blades of the wind turbine to spin, which is mechanically connected to the low-speed shaft in the wind turbine nacelle. Then the fixed-ratio gearbox transformed the low speed in low-speed shaft to the high speed in the high-speed shaft which drives the generator rotor for power generation. It is the basic operation manner of a wind turbine. During this process, there are several levels of control to realise the power generation. The uppermost level of control is to determine the start-up or shut-down of the wind turbine, in case of the insufficient or high wind. It is followed by the turbine-level control, which consists of three control strategies to realise the power extraction, namely yaw control, torque control and pitch control. The lowermost level of control is the generator, actuator and power electronics control [69]. See Fig. 1.4 for the illustrative steady-state power curve [69]. In Fig. 1.4, the start-up and shut-down are referred to the region 1 and high-wind cutout (or entitled as region 4 in some literatures). In region 2, the torque control is realised by the power

electronics (specifically, the high-speed shaft) to against the aerodynamic torque from the wind, aiming to regulates the wind turbine rotor speed. Theoretically, the aerodynamic power available to be captured is limited to be 59.26% which is called the 'Betz limit' [113, 17], while it is around 40% in realistic scenarios [40, 69]. It is represented as the power coefficient C_p in Fig. 1.4. That is, the wind turbine control in this region is designed to maximise the wind power capture by regulating the wind turbine rotor speed, which is known as maximum power point tracking (MPPT). In region 3, the wind is abundant. The pitch actuator operates together with the power electronic to realise the pitch control and torque control, in order to maintain the wind turbine rotor speed and the power extraction around their ratings [52, 132, 69]. The yaw control is always slower than the torque and pitch control, which is of less interest and not considered in this thesis. Then with proper 3-stage control, the desired amount of power can be captured and delivered to the power grid.

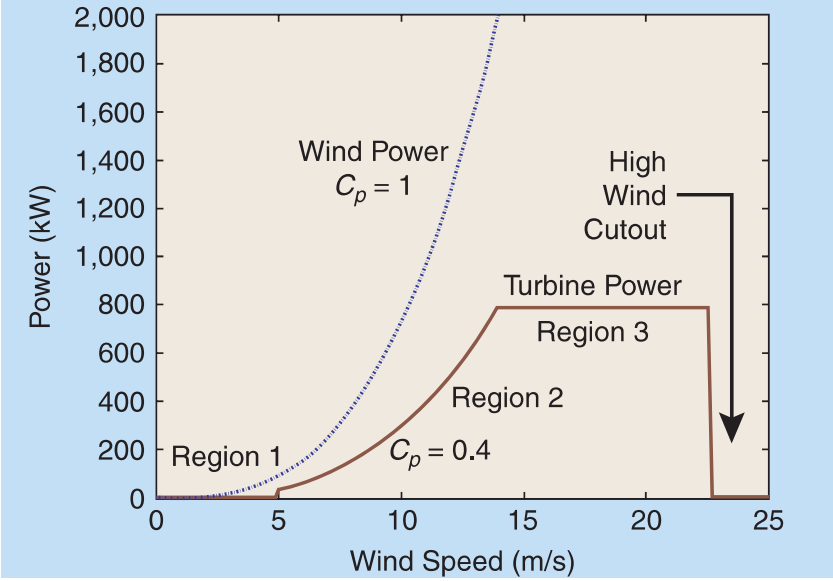

Figure 1.4: Illustrative steady-state power curves of wind turbine. C_p represents the power coefficient, which is defined as ratio between captured power and wind power. This figure is taken from [69].

1.1.3 Grid integration of wind turbine

The electricity got into commercial use in late 1870s, and in 1882 Thomas Edison built the first power grid system in the world, which supplied the 59 customers within the radius of 1.5 km for illumination [76, 145]. After the development for over a centuries,

the power grid is modernised into a greener and more effective system, which includes transmission system, distribution networks, large-scale load centres, advanced energy storage techniques, and multiple forms of power generations [145]. To guarantee the safe and effective operation of modern power system, it is important to investigate the grid integration techniques for different forms of power generations, including wind power generations. Here we mainly focus on the grid integration structures of the wind turbine and the energy storage techniques in wind power integration systems.

Grid integration structures of wind turbine

The grid connection of wind turbine are generally categoried into 4 types which are shown in Fig. 1.5 [14]. The first structure is to use the squirrel-cage induction generator (SCIG) with wound rotor. The capacitor bank serves as the reactive power compensator in this system. It is the structure without power converters. The generator speed in this structure is compulsorily limited to the grid frequency, with only 2% – 4% variations allowed [14] (see Fig. 1.5(a)).

Then the second structure is the SCIG or synchronous generator (SG) connecting to the full-scale converters. It offers high flexibility in wind turbine operations and design, since the connection between generator and grid is completely 'cut off' by the full-scale power converters. It allows the wind turbine to rotate at its optimal aerodynamic speed [14]. However, the existence of full-scale converters inevitably leads to the power loss in operations. Besides, the converters are expensive in both construction and maintenance (see Fig. 1.5(b)).

The vulnerable gearbox is believed to be one of the main causes to the high maintenance of the wind turbines, particularly in the offshore case [56]. It is even more vulnerable due to the higher wind speed in offshore case. Hence, based on the second structure, the third one removes the gearbox by introducing the multipole permanent magnetic synchronous generator (PMSG). It is denoted as 'direct-drive wind turbine' in some literatures [63, 111]. It improves the reliability of the wind turbine system at the expenses of the heavy nacelle and expensive cost for the rare earths permanent magnetic materials [111] (see Fig. 1.5(c)).

The fourth structure is the widely used one in the existing wind power market, called doubly fed induction generator (DFIG) structure. In comparison with the third structure, the weight is lighter and the operation and maintenance (O & M) cost is lower. It connects to the grid via partial-scale converters [111]. In this thesis, we mainly consider to improve the performance of this structure. The speed variations of the

generator in this structure is allowed to be 60% of its synchronous speed, and the power rating of the converters are usually around 40% of the generator rating [14]. However, due to the existence of partial-scale converters, the DFIG configuration is under the risks of over-current in generator & converters and over-voltage in DC-link during grid disturbance [6] (see Fig. 1.5(d)).

Energy storage techniques in wind power integration system

Due to the uncontrollable nature of the wind, the wind power integration inevitably poses a great challenge to the stability and reliability of the power systems with the increase of wind penetration rate [166]. To guarantee the stable operation of the grid system, the grid disturbance ride-through ability is usually specified in grid codes for wind power generations. In some European countries where wind penetration rate is high, the grid codes even request the wind power to participate in the system frequency support [32, 92]. The energy storage system (ESS) plays a key role in these applications, which makes the system more flexible. Also, the power system with ESS benefits from the hedge risk, energy arbitrage, high-energy utilisation, stability with improved power quality [7].

There are various types of energy storage technologies in wind power system. Here we list some technologies with their brief introductions [31, 7], including pump hydro energy storage (PHES), compressed air energy storage (CAES), battery energy storage system (BESS), supercapacitor energy storage (SCES), hydrogen-based energy storage system (HESS), and flywheel energy storage system (FESS).

- PHES regulates the energy by pumping or releasing the water between the lower and higher reservoirs. It is already a mature techniques which has been applied in industries for a long time. However, the response is relatively slow and it is geographical dependent [65, 166].

- CAES regulates energy by compressing and de-compressing the air into the underground caverns. It has high power and energy capacity rating, however, it is highly geological-dependent and it requires extra aboveground devices [166].

- BESS in wind power system are generally connected to the DC-link between two power converters and regulates the energy by charging and discharging the batteries. It is the most widespread energy technique in power system applications due to its fast response and accurate regulations [10, 33]. However, the introduced power electronic devices leads to high cost and low reliability.

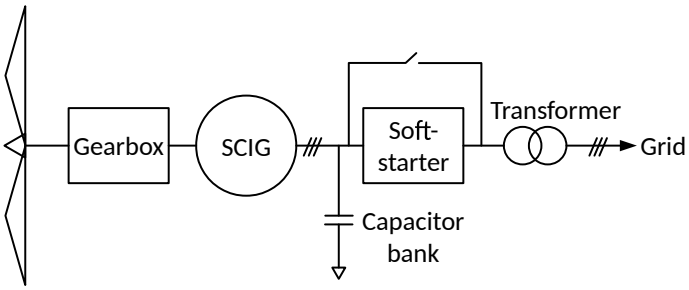

(**a**)

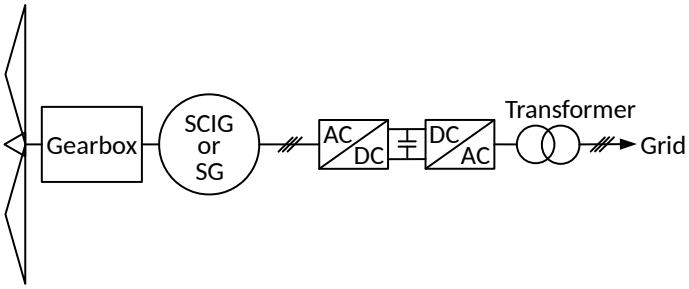

(**b**)

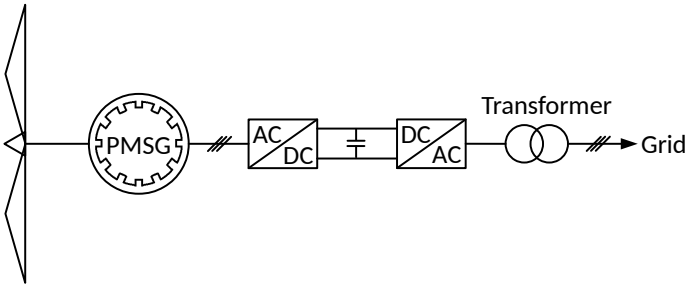

(**c**)

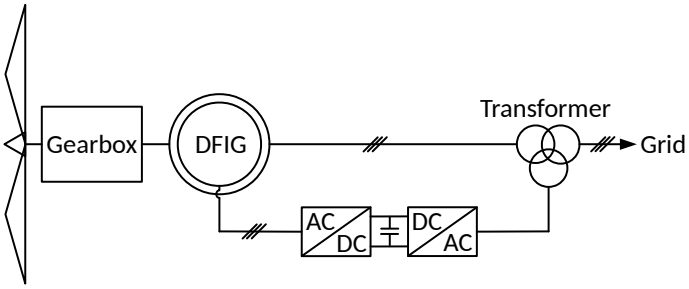

(**d**)

Figure 1.5: Grid integration configurations of wind turbine system [14].

- The application of SCES in wind power system is similar to the BESS, which stores energy by charging and discharging the supercapacitor. It is also connected to the

DC-link between two power converters with more power electronics devices being introduced [3].

- The HESS is a popular chemical energy storage technique. It stores energy by electrolysing water for hydrogen and release the energy in fuel cell or directly burnt it. It has high energy density, however, the substantial energy loss for application of electricity storage limits its widespread use [4].

- FESS is to store energy in form of kinetic energy. The energy is stored or released via accelerating or de-accelerating the flywheel rotor. It has high efficiency, high power density, long life cycle with low maintenance cost. However, it suffers from the short operation duration and high self-discharge losses [166, 7].

Hydrostatic wind turbine

A new possibility for wind turbine grid integration is provided by the hydrostatic wind turbine (HWT). It is to use the hydrostatic transmission (HST) drivetrain instead of the gearbox for wind turbine power transmissions. With proper control, the wind turbine is allowed to connect to the synchronous generator (SG), and then connect to the grid without power converters like a conventional thermal or hydro plant.

The gearbox allows wind turbine to achieve high efficiency. However, it is one of the main reasons for the premature failure and high maintenance cost of the wind turbine [119, 128], thus the PMSG direct-drive structure (Fig. 1.5(c)) is proposed to remove the gearbox. But it brings new problems of heavy nacelle and high cost for rare earths permanent magnetic materials. Then the HST gradually comes into our sight. Actually, in late 1970s, the HST already started to be considered as the substitution for gearbox drivetrain in wind power system. In early 1980s, an experiemental turbine, Bendix SWT-3, started to operate in California, which served as an important historic reference for HST in wind turbines [110]. See Fig. 1.6 for the photo of the Bendix SWT-3 experimental wind turbine. It is a 3-MW wind turbine installed with the complex drivetrain concept incorporated a gearbox which drived a hydrostatic transmission [123, 110]. However, the efficiency of Bendix SWT-3 was only about 60%, which made the HST unaffordable for wind power industry [117]. With the development in HST techniques, the efficiency of HST is improved to be over 80%. For some specific manufacturers like Artemis Intelligent Power, the HST efficiency with its 'Digital Displacement (DD)' technique is claimed to be as high as 91% in partial load condition [110, 142]. In the past decade, the wind turbine with Artemis DD HST technique has been designed, tested and put

into operations [142, 102]. By applying this DD HST technique, the hydrostatic wind turbine benefits from high reliability, high power-weight ratio and high compatibility with synchornous generator, which offers converter-free grid integration. It means the HST drivetrain in wind trubine starts to become a good option for wind power market in overall considerations [18, 116, 118], particularly in the offshore case. Thence, after over 30 years of the experimental turbine Bendix SWT-3, the HST in wind turbine starts to become more and more close to the market. The control and grid integration of HWT will be investigated in this thesis.

Figure 1.6: Photo of the Bendix SWT-3 experimental wind turbine which was put into operation in 1980s. This figure is taken from [110].

1.1.4 Reliability of the wind turbine

The reliability of the wind turbine is determined by some key components, such as the gearbox, electrical system, generator, pitch system, wind turbine rotor, mechanical brakes, yaw system, sensors, control system and hydraulics [21]. There are some surveys

conducted to investigate the reliability of wind turbine and its sub-assemblies. In this section, some key results from three popular and large surveys in Europe are provided, which are the WMEP (Wissenschaftliches Mess- und Evaluierungsprogramm), LWK (Landwirtschaftskammer Schleswig-Holstein) and WindStats newsletter [133, 127, 141, 109, 2, 1]. In these three surveys, the WMEP database contains detailed information about reliability and availability of $1,500$ wind turbines and their subassemblies, the LWK database provides the number of failures per system for over 650 wind turbines in northern Germany, and the WindStats newsletter provides the wind turbine production and operating data quarterly from turbines in Sweden, Denmark, Germany and Finland [127]. Note that there are other surveys conducted in Europe (such as Vindstat [109], ReliaWind [156]) and U.S. (such as CREW [108]), which are not discussed here.

Here we listed a few criteria to describe the wind turbine failures [140]:

- MTBF: mean time between failures.
- λ: failure rate, which calculates from $\frac{1}{MTBF}$.
- MTTR: mean time to repair, (or downtime).
- μ: repair rate, which calculates from $\frac{1}{MTTR}$.
- A: availability, which calculated from $1 - \frac{\lambda}{\mu}$.

Fig. 1.7 shows the failure rate and downtime from WMEP and LWK database [127, 140]. It is clear that the electrical system (power converters included) has the highest failure rate which implies that it is the most vulnerable sub-assemblies in the wind turbine system, and that the gearboxes causes longest downtime per failure, which indicates that gearbox failure is the most critical failure since long downtime for repairs or replacement stops the power generation which is the primary function of wind turbines [21].

Fig. 1.8 presents the aggregated downtime per turbine subsystem from the Windstats Newsletter during 2008 – 2012 [127][2]. It demonstrates that the gearbox is the highest downtime driver, which is followed by the electrical system. The statistics in Fig. 1.9 are also from the Windstats Newsletter [127][1], which shows that the failure rate of electrical system and gearbox ranked top two in the wind turbine subsystems in 2012. These two reasons contribute approximately 10% of the failure events each year.

From these three databases, it is clear that in Europe, the electrical system (power converters included) and gearboxes are the most vulnerable components in the wind turbine system. Long downtime and high failure rate inevitably lead to high

maintenance cost. Particularly in the offshore case, it may require longer time and higher cost for the maintenance [140].

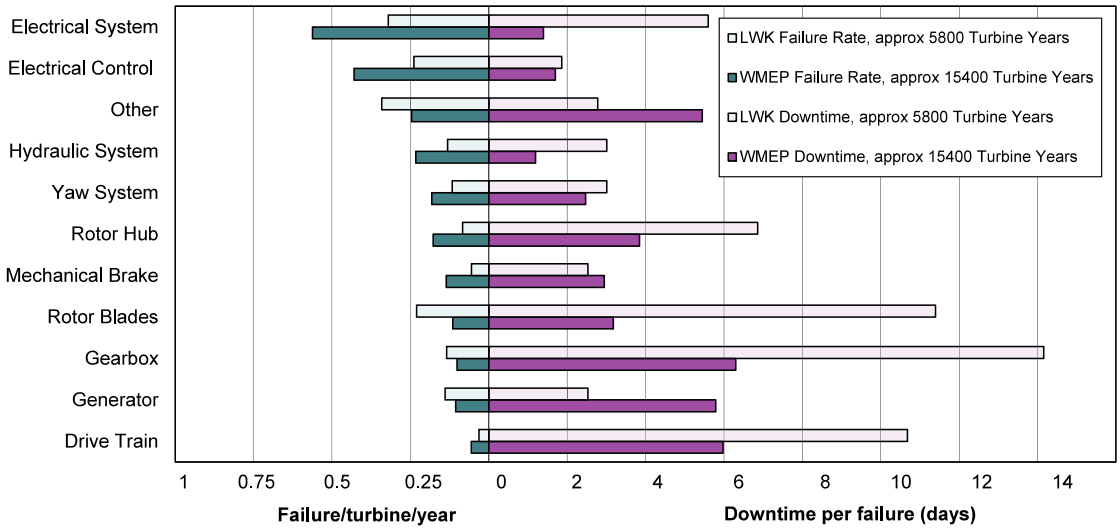

Figure 1.7: Failure/turbine/year and downtime from two large surveys of land-based European wind turbines over 13 years. This figure is taken from [127, 140].

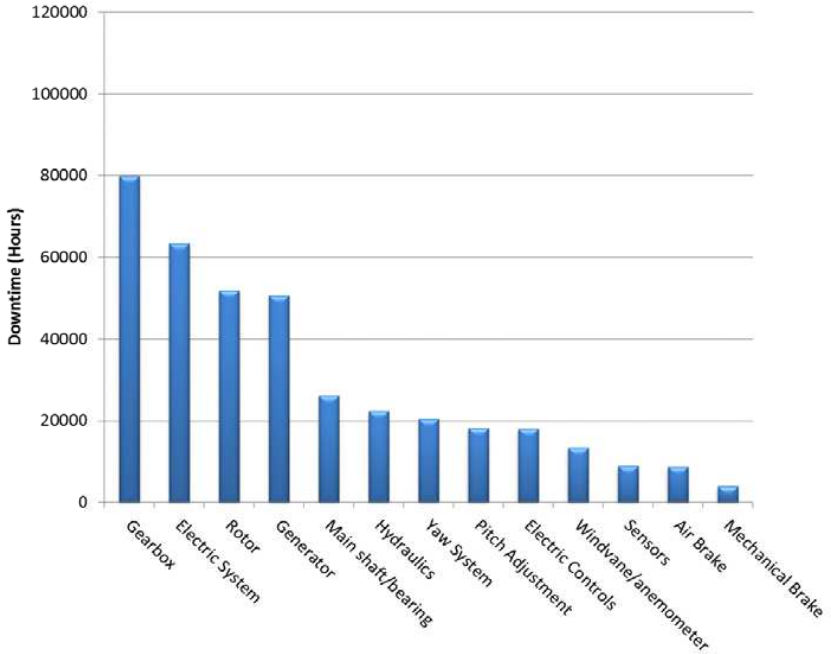

Figure 1.8: Aggregated downtime per turbine subsystem during 2008–2012. This figure is taken from [127][2].

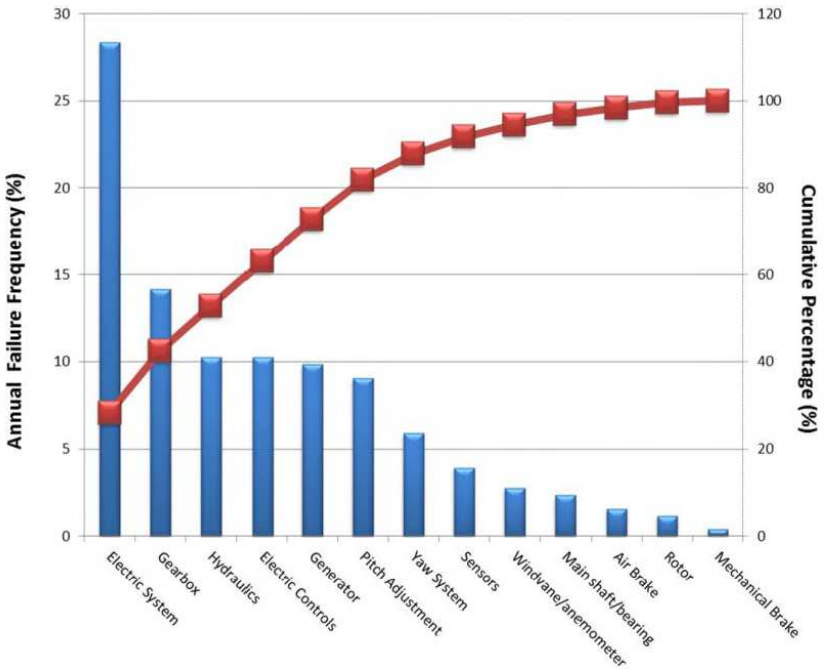

Figure 1.9: Annual failure rate per turbine subsystem in 2012. This figure is taken from [127][1].

1.1.5 Wind turbine models

In this thesis, the dynamic responses of the wind turbine model is simulated by the FAST (Fatigue, Aerodynamics, Structures and Turbulence) code [72]. FAST takes aerodynamics, control & electrical (servo) dynamics, and structural (elastic) dynamics of the turbines into account. It is interfaced with Matlab/Simulink through a Simulink S-Function block. During simulations, this block calls the FAST Dynamic Library, which has integrated all the FAST modules [72] and is compiled as a dynamic-link-library (DLL). FAST provides 26 wind turbine sample models. In this thesis, we mainly employ the popular the WindPACT (WP) 1.5-MW baseline wind turbine model (Test 13 in [72]) and the NREL 5-MW monopile wind turbine model (Test 19 in [72]).

WindPACT wind turbine is a series of baseline wind turbine models designed for investigating the scaling of costs, loads, and/or optimisation routines, with the power ratings of 0.75 MW, 1.5 MW, 3 MW and 5 MW. Amongst these four models, the design of WP 1.5 MW wind turbine model is the closest to the commercial wind turbine technology, which is extensively applied for studies of novel configurations and wind turbine technology innovations [120]. See Table. 1.1 for the gross properties of WP

1.5-MW wind turbine.

The NREL offshore 5-MW gearbox-equipped wind turbine model is the representative of typical utility-scale land- and sea-based MW turbines [71], which is widely used as a reference by research teams throughout the world. The gross properties of the NREL 5-MW wind turbine are listed in Table. 1.2 [71].

Table 1.1: Gross properties of WindPACT 1.5-MW wind turbine [120, 91].

Rating	1.5 MW
Rotor Orientation, Configuration	Upwind, 3 blades
Control	Variable speed, Collective pitch
Drivetrain	High speed, Multi-stage gearbox
Rotor diameter	70 m
Hub height	84 m
Cut-in, Rated, Cut-out wind speed	3 m/s 11.5 m/s 27.6 m/s
Rated rotor speed	20.463 rpm
Rated tip speed	75 m/s
Rotor mass	32,016 kg
Nacelle mass	52,839 kg
Tower mass	125,363 kg
Gearbox ratio	87.965 : 1

1.2 Motivations and research contributions

This thesis mainly focuses on the control of the offshore wind turbine and its grid integration. Two types of wind turbines are considered, namely conventional gearbox-equipped wind turbine and hydrostatic wind turbine (HWT). The research are conducted in the following aspects:

- The wind turbine is connected to the grid via two back-to-back converters with a DC-link capacitor in-between to stabilise the DC-link voltage. The DC-link voltage stabilisation ability will influence the performance of wind turbine torque control, which further influences the wind power capture of the wind turbine. Also, when grid disturbances occur, it is essential to keep DC-link voltage steady so that the risk of converter damage will be reduced and the performance of the voltage ride through algorithm will be guaranteed. However, large DC-link capacitor is

Table 1.2: Gross properties of NREL 5-MW offshore wind turbine [71].

Rating	5 MW
Rotor Orientation, Configuration	Upwind, 3 blades
Control	Variable speed, Collective pitch
Drivetrain	High speed, Multi-stage gearbox
Rotor, Hub diameter	126 m, 3 m
Hub height	90 m
Cut-in, Rated, Cut-out wind speed	3 m/s 11.4 m/s 25 m/s
Cut-in, Rated rotor speed	6.9 rpm, 12.1 rpm
Rated tip speed	80 m/s
Rotor mass	110, 000 kg
Nacelle mass	240, 000 kg
Tower mass	347, 460 kg
Gearbox ratio	97 : 1

always expensive and vulnerable, which increases the cost for the wind integration, especially in the offshore case. Hence, seeking a robust replacement for the DC-link capacitor is of great necessity. We firstly propose a control algorithm for the virtual infinite capacitor (VIC), making it function as a large filtering capacitor. Before applying it to the wind turbine system, it is tested in simulations by replacing the output filtering capacitor in a simple power factor compensator (PFC) circuit. The simulations show that VIC is a good and improved replacement for the large filtering capacitor. Then it is experimentally validated by simply injecting the ripple voltages for VIC to suppress. The VIC's ripple suppression performance in experiment is outstanding and highly consistent with the corresponding simulation results, which demonstrates its possibility to replace the DC-link capacitor in wind power integration system.

- The VIC mainly aims to limit the low frequency ripples in voltage while it is very common that the DC-link voltage ripples of wind turbine are in two distinct frequency ranges. Hence, we proposed the parallel virtual infinite capacitor (PVIC) concept to deal with the voltage ripples in a wider frequency band. We applied two sliding mode controllers (SMC) for the voltage control with a PI charge controller to realise 'plug-and-play' of the PVIC. The simulations are conducted in an offshore WindPACT (WP) 1.5-MW grid-connected wind turbine system. We replace the original DC-link capacitor by the PVIC. The simulations show that the PVIC

provides much better voltage stabilisation capability than the equivalent DC-link capacitor no matter under normal grid operations or under different types of grid faults.

- Although the application of PVIC removes the fragile DC-link capacitor in the power conversion system (which includes two back-to-back converters and a DC-link capacitor), the power converters in power conversion system are also fragile and expensive. Moreover, the power converters decouple the direct inertia support from the wind turbine to the grid, which imposes great challenges in frequency regulations for the modern grid system. Hence, we study the feasibility to completely remove the power converters in the offshore wind turbine grid integration system by using a hydrostatic wind turbine (HWT). We propose a structure with a coordinated control scheme for the HWT. Recall that HWT is a wind turbine which replaces the gearbox drivetrain of conventional wind turbine by the hydrostatic transmission (HST) drivetrain. The simulation model is transformed from the popular NREL 5-MW monopile offshore wind turbine. The control scheme fully takes advantages of the offshore geography to effectively realise the 'continuously variable gearbox ratio', which allows the wind turbine to connect to a synchronous generator (SG). Then, the SG is connected to the grid directly without power converters. The simulation is conducted in a 5-bus grid model with variable load demands under turbulent wind input. The results demonstrate that the HWT with the proposed coordinated control scheme is a feasible solution for the future offshore wind turbine system, which can participate in the grid frequency regulation and directly provides inertia support to the grid.

- Finally, we consider to improve the power generation control performance of HWT by using a novel control algorithm called model-free adaptive control (MFAC) scheme. It is applied to both the torque control and the pitch control of the HWT. We also consider the smooth transition between region 2 and 3 and investigate the fatigue load exerted on the wind turbine tower by different control laws. In comparison with these control laws, MFAC controller provides better tracking and disturbance rejection performances with less fatigue loads exerted on the wind turbine tower. Moreover, MFAC controller benefits from the small computation burdens and easily-applicable characteristics, which proves to be a promising algorithm for the HWT power generation control.

1.3 Thesis outline

The thesis is organised as follows. Chapter 2 develops the control algorithms of the virtual infinite capacitor (VIC) with validations in both simulation and hardware experiment. Chapter 3 proposes the concept of the parallel virtual infinite capacitor (PVIC) and uses it to replace the DC-link capacitor in the 1.5-MW offshore DFIG-based wind turbine grid integration system. Grid faults are generated to inject some random disturbances to the DC-link voltage, to test the voltage stabilisation capability of the PVIC in simulations. Chapter 4 designs a coordinated control system for a 5-MW offshore hydrostatic wind turbine (HWT). The HWT allows to remove the power converters and realise grid frequency regulation like conventional thermal plants do. Chapter 5 considers the application of the model-free adaptive control (MFAC) algorithms for the wind power generation of the HWT, including a MFAC torque controller and a MFAC pitch controller. Their performances are compared with some existing control algorithms, i.e. $\mathcal{H}_\infty$ loopshaping controller and gain-scheduling PI controller. Finally, Chapter 6 concludes this thesis and lists some possible future study areas.

Chapter 2

Control of a Virtual Infinite Capacitor with Experimental Validation

The wind turbine is connected to the grid via two back-to-back converters with a DC-link capacitor in-between for DC-link voltage stabilisation. However, the DC-link capacitor is fragile, which increases the maintenance costs. Hence, seeking a robust alternative solution is of great necessity. In this chapter, we explore the possibility to use the virtual infinite capacitor (VIC) developed in [163] to replace the DC-link capacitor of wind turbine for voltage stabilisation and power filtering. We develop a control algorithm for VIC and add the snubber circuits to the VIC topology to enable the soft switching (zero current or zero voltage switching) and reduce energy loss. Before applying VIC to the wind turbines, we verify the performance of VIC at a simple two-phase interleaved power factor compensator (PFC). The simulation results indicate that VIC performs well in voltage filtering. See the results also in our paper [82].

In addition to the simulation test based on the PFC, we also experimentally check the ripple suppression performance of VIC in a simple and straightforward way. We design a printed circuit board (PCB) for VIC and inject a DC voltage with a 50 Hz sinusoidal voltage to it. With the control designed by us, the sinusoidal ripple is eliminated at its output terminal and the experimental results are highly consistent with the corresponding simulations. The outstanding ripple suppression performance demonstrates the possibility to substitute the fragile DC-link capacitor by VIC. See these results also in out paper [83].

2.1 Introduction

Capacitors are commonly used for DC voltage smoothing (ripple elimination) in power electronic circuits, such as photovoltaic systems, fuel cells, LED drivers, electric (or hybrid) vehicles and their chargers, power factor compensator (PFC), the powertrain of wind power generators, etc. Low-frequency ripple suppression requires large capacitance, which could be provided by electrolytic or super-capacitors. However, such capacitors suffer from low reliability and low operating voltages [75, 16, 26]. Many ideas have been proposed as the alternatives to large capacitors in voltage smoothing (or to achieve better voltage smoothing performance with the same capacitance), see (in chronological order) [28], [152], [167], [23], [61], [107], [20], [114], [19], [168], [160], [136], [101], [115] and the references therein. These papers offer a large variety of ingenious ideas, such as virtual inductors (in [28]), internal models that learn the relevant frequencies of the ripple current and inject a compensating current (in [167]), injecting a compensating current based on a phase locked loop (in [152]), for the output voltage variations of controlled rectifiers (in [20, 168]), and the concept of stacked switched capacitors (in [23, 107, 101]). The circuits are entitled as "power filters", "active capacitors" or "ripple eliminators' in these literatures. We refer to [61, 136] for nice surveys of this area. In this line of research, the *virtual infinite capacitor (VIC)* concept has been introduced in [163], [162]. It is a circuit which is able to eliminate random low-frequency voltage fluctuations [163, 162, 81]. Different from a usual capacitor whose dependence of the voltage V on the charge $Q(t) = \int_0^t i(\sigma)\mathrm{d}\sigma$ is linear, the idea is to create a nonlinear capacitor where the plot of voltage as a function of charge has a flat segment. In this segment, the dynamic capacitance is infinite due to its definitions $C = \frac{dQ}{dV}$ (see Fig. 2.1). We think that the VIC circuit is relatively simple (hence cheap and small) that should suppress unpredictable (random) voltage fluctuations. Indeed, the VIC does not "learn" the harmonic content of the disturbance current, like an internal model would, it makes no a priori assumptions about the current. It acts according to the curve in Fig. 2.1 no matter what the current is. It could be useful in the DC-link voltage stabilisations.

The abstract concept of VIC has potentially many approximate realisations as an electronic circuit. The realisation proposed in [163] is a canonical switching cell, as defined in [73], also known as a bidirectional (or reversible) buck converter, as shown in Fig. 2.2 (without the sensors, control circuitry and drivers). Very similar circuits have been used for power filtering (without introducing the VIC concept) in [152], [167], [20] and a less similar, but still related circuit appears in [114]. We will use a slight modification of the basic circuit from Fig. 2.2 which facilitates soft switching (to explain

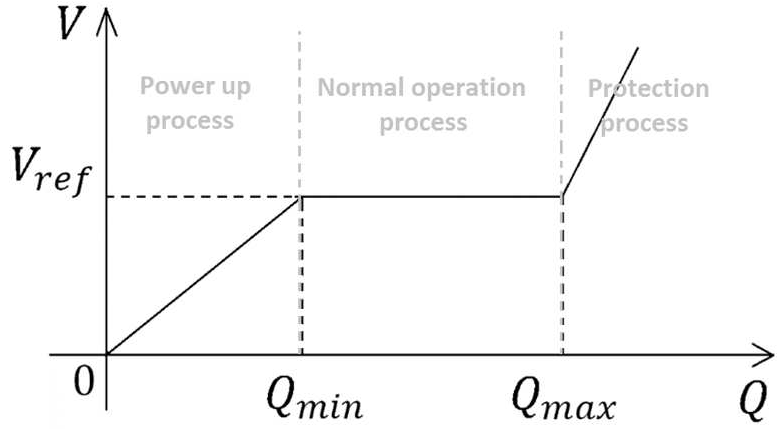

Figure 2.1: $Q - V$ characteristics of a VIC. The useful operating range is where $Q \in [Q_{min}, Q_{max}]$.

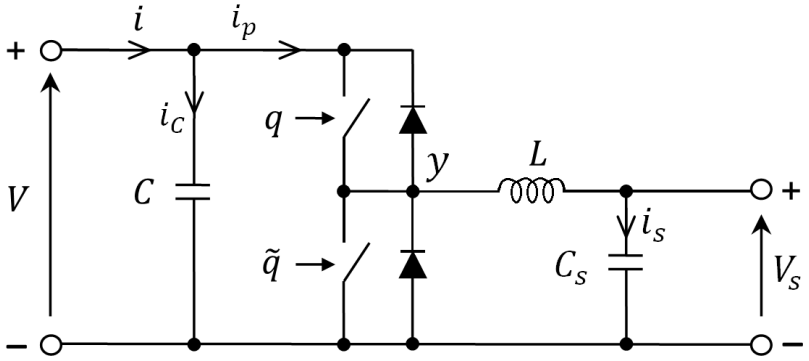

Figure 2.2: The approximate realisation of the VIC, showing only the main circuit elements without showing the sensing and control circuits. The terminals for V_S are only for sensing. q and $\tilde{q}$ are binary signals coming from the controller, that determine the ON or OFF status of the switches.

later).

We briefly describe how the VIC works using the simplified circuit in Fig. 2.2. This description is general, it holds regardless of the control algorithm used. It is clear from Fig. 2.1 that the operation of the VIC can be divided into three regions. The *first region*, where $Q \in [0, Q_{min}]$, is mostly used for the power up process. The easiest strategy is to use the buck converter in continuous conduction mode with constant duty cycle D, so that while C is charged to the voltage V_{ref}, the capacitor C_s is charged to the voltage $V_{s,min} = DV_{ref}$. $V_{s,min}$ is the lowest voltage at which the converter can work efficiently in boost mode to transfer energy from the capacitor C_s to the capacitor C,

when the latter is near the voltage V_{ref}. The value $V_{s,min}$ is chosen by the designer of the VIC, which is of the order of $V_{ref}/4$ (so that D is of the order of 0.25). We now recognize that Q_{min} is the charge Q that causes V_s to reach $V_{s,min}$. It is easy to check that the dynamic capacitance of the VIC in the first region is $\mathrm{d}Q/\mathrm{d}V = C + D^2C_s$.

The designer of the VIC has to choose a maximum allowed value of V_s, denoted by $V_{s,max}$, which must be less than V_{ref} for the converter to work. The charge Q that causes V_s to reach $V_{s,max}$ is denoted Q_{max}. The *second region*, where $Q \in [Q_{min}, Q_{max}]$ (and hence $V_s \in [V_{s,min}, V_{s,max}]$), is the *normal operating range* of the VIC. In this region, the charge Q will vary while the voltage on V will remain constant at V_{ref}. The *third region* (where $Q > Q_{max}$) means the capacitor C_s is overcharged and it should be avoided by opening both switches, so that only capacitor C is connected to the terminals.

There must be an additional control mechanism in place to prevent the VIC from leaving the normal operating range described above. The VIC controller cannot do this, since all it does is to ensure that the VIC behaves according to Fig. 2.1. This additional control mechanism consists of a *charge controller* and a power source (or power sink) that can be controlled, to some extent, by the charge controller. The charge controller gets the measurement of V_s from the VIC, which is an indication of the charge Q stored in the VIC. Indeed, it was shown in [163, Sect. 3] that

$$V_s = \sqrt{\frac{2V}{C_s}Q + \beta}, \qquad \beta = V_{s,min}^2 - 2\frac{Q_{min}V}{C_s}.$$

If the charge controller senses that Q is too low or too high, it will "order" the power source to inject more (or less) average power onto the DC bus, as the need may be, to ensure that Q stays within the normal range. Such a control mechanism exists on any DC bus, also if we have a conventional capacitor on the bus (instead of the VIC). In the latter case, the charge controller is the usual voltage controller, since voltage and charge are now proportional to each other. The design and stability analysis of the charge controller has been discussed in detail in [163, Sect. 3]. We shall rely on this design from [163] without repeating it here.

The delicate issue is the control of the VIC in the normal operating range (the other two regions are sort of trivial). In this chapter we propose a control algorithm for the VIC and modify the circuit realisation in Fig. 2.2 [163] to enable soft switching, hoping to reduce the power loss during operations.

With the proposed control strategy, we further demonstrate its performance with hardware experiment. The experiment is conducted without considering the charge control mechanism. Hence, the VIC will sometimes run out of the normal operating

range. However, it is enough to demonstrate the ripple suppression performance of VIC controller during the period when it is within the normal operating range. We connect an auto-transformer in series with a DC voltage supply, in order to directly inject the sinusoidal ripples to the VIC. The aim of the control is to eliminate the ripple and extract the DC voltage when VIC is within the normal operation range.

2.2 Control of the VIC

We propose a novel feedback control algorithm for the VIC operating in the normal operating range $Q \in [Q_{min}, Q_{max}]$, that is based on two controllers, one for buck operation and the other for boost operation of the bidirectional DC/DC converter. In each of these two modes of operation, the controller operates only one of the two switches.

We improve the circuit from Fig. 2.2 to Fig. 2.4. The role of the body diodes visible in Fig. 2.2 is taken over by the diodes D_1 and D_2 in Fig. 2.4. For ease of understanding, the control algorithm for the circuit (Fig. 2.2) will be explained.

2.2.1 Voltage control

When the current $i_p = i - i_C > 0$ (i.e., it is flowing from the DC bus to the internal capacitor C_s), the converter operates in buck mode, and V_s increases. At this stage, only the upper switch is controlled; the lower switch is always OFF, with its body diode acting as the freewheeling diode. Conversely, when $i_p < 0$, the converter operates in boost mode and the upper switch is always OFF. However, we do not really measure i_p. Instead, we compute a reference value for it, denoted i_p^* (as explained below), and the decision whether to operate the converter in buck or boost mode depends on the sign of i_p^*.

We shall regard the system to be controlled in the voltage loop as being just the capacitor C, described by

$$C\dot{V} = i - i_p, \tag{2.1}$$

where we regard i_p as a variable that we can control, at least in the sense of its average over a switching cycle, which we can force to be equal to the reference signal i_p^*. And i is the disturbance signal (since it depends entirely on the external power source and the loads on the DC bus).

We measure V and i and, in order to eliminate the influence of the high frequency noise, we low-pass filter them with transfer function $\mathbf{F}$. We do this because at any rate, our controller cannot do anything against high frequency noise, but this noise can corrupt

the data on which our controller is working. It is preferable to use a transfer function of the type $\mathbf{F}(s) = \frac{\phi_1\phi_2}{(s+\phi_1)(s+\phi_2)}$, where $\phi_1 > 0$ and $\phi_2 > 0$ are the corner frequencies, of the order of several thousand rad/sec, but strictly less than the switching frequency, because we want the filter to attenuate the noise due to the switching. We indicate by the subscript f the filtered signals, such as V_f and i_f.

We propose a PI controller to regulate the filtered voltage deviation $e = V_{ref} - V_f$. The PI controller determines the desired average current i_p^* and it is described by $i_p^*(t) = i_f(t) - k_P e(t) - k_I \int_0^t e(\sigma)\mathrm{d}\sigma$, where $k_P > 0$ and $k_I > 0$ are the controller's adjustable parameters. From (2.1) we have

$$-C\dot{e} = C\dot{V}_f = i_f - i_{pf} = i_f - i_p^* + [i_p^* - i_{pf}]$$

whence

$$C\ddot{e} + k_P\dot{e} + k_I e = \frac{\mathrm{d}}{\mathrm{d}t}[i_{pf} - i_p^*]. \tag{2.2}$$

We see that this is a stable (second order) linear system with disturbance input $d = i_{pf} - i_p^*$. If the current control (described further below) works correctly, the average of i_p over the current switching cycle is equal to the current sample of i_p^*, and if the switching frequency is higher than ϕ_1, ϕ_2, then $i_{pf} \approx i_p^*$, so that d is very small. Its main frequencies are the frequencies of i and the harmonics of the switching frequency. From (2.2), the transfer function from d to e is $\mathbf{H}(s) = \frac{s}{Cs^2 + k_P s + k_I}$. It is obviously vanishing at very small as well as at very high frequencies. We can place its corner frequencies wherever we want, by choosing suitable k_P and k_I. These should be tuned experimentally, to minimize the peak values of e in the specific application of the VIC.

2.2.2 Current control

As mentioned before, we operate the VIC converter in DCM. The inductor current waveforms are shown in Fig. 2.3. q and $\tilde{q}$ are binary signals that turn the switches ON. q_B and $\tilde{q_B}$ are binary signals (introduced only for our computations) that are equal to 1 if and only if $|i_s|$ is decreasing (and the current is flowing through one of the body diodes), as shown in Fig. 2.3. T denotes switching period. q_B^* and $\tilde{q_B}^*$ denote the averages of q_B and of $\tilde{q_B}$ over one switching period. Similarly, q^* and $\tilde{q}^*$ are the average of q and $\tilde{q}$ within one switching cycle, i.e. the duty cycle of the corresponding switches.

When $i_p^* > 0$, the converter is in buck mode, so that $\tilde{q} = 0$. Assuming V_s is nearly

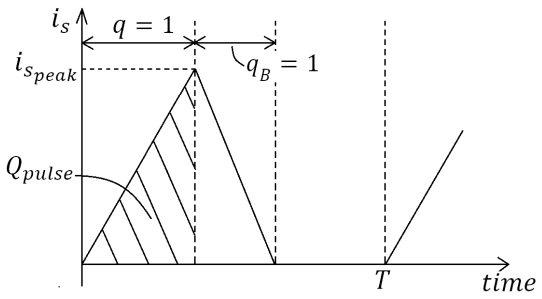

(**a**)in buck process

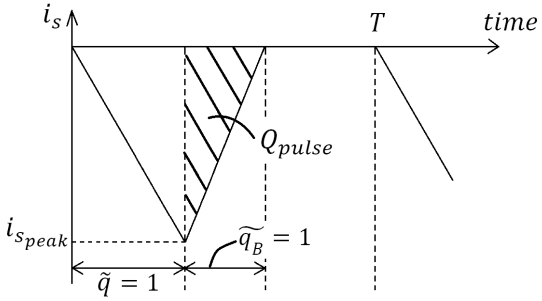

(**b**)in boost process

Figure 2.3: Waveform of inductor current i_s in DCM.

constant in a switching cycle, we have

$$i_{s_{peak}} = \frac{V - V_s}{L} q^* T, \quad \text{when} \quad q = 1;$$

$$q_B^* T = \frac{-i_{s_{peak}} L}{-V_s} = \frac{V - V_s}{V_s} q^* T, \quad \text{when} \quad q = 0.$$

Q_{pulse} denotes the charge flowing through i_p per cycle:

$$Q_{pulse} = \int_0^{q^* T} i_s dt = \frac{1}{2} q^* T i_{s_{peak}} = \frac{V - V_s}{2L} q^{*2} T^2.$$

Thus the average current i_p per cycle and duty cycle q^* are

$$i_p^* = \frac{Q_{pulse}}{T} = \frac{V - V_s}{2L} q^{*2} T,$$

$$q^* = \sqrt{\frac{2L i_p^*}{(V - V_s)T}}.$$

When $i_p^* < 0$, the converter is in boost mode, so that $q = 0$.

$$i_{s_{peak}} = \frac{-V_s \tilde{q}^* T}{L}, \quad \text{when} \quad \tilde{q} = 1;$$

$$\tilde{q_B}^* T = \frac{-L i_{s_{peak}}}{V - V_s} = \frac{V_s}{V - V_s} \tilde{q}^* T, \quad \text{when} \quad \tilde{q} = 0.$$

We have

$$Q_{pulse} = \int_{\tilde{q}^* T}^{\tilde{q}^* T + \tilde{q_B}^* T} i_s dt = \frac{-V_s^2 T^2}{2L(V - V_s)} \tilde{q^*}^2.$$

Thus the average current i_p^* and duty cycle $\tilde{q^*}$ are

$$i_p^* = \frac{Q_{pulse}}{T} = \frac{-V_s^2 T}{2L(V - V_s)} \tilde{q^*}^2,$$

$$\tilde{q^*} = \sqrt{\frac{2L(V - V_s) i_p^*}{V_s^2 T}}.$$

Looking at all three regions of operation from Fig. 2.1, the current control of the VIC can be summarized as follows: When $V_s \in [0, V_{s,min}]$,

$$\begin{cases} q^* & = \frac{V_{s,min}}{V_{ref}}, \\ \tilde{q}^* & = 1 - q^*. \end{cases}$$

When $V_s \in [V_{s,min}, V_{s,max}]$,

$$\begin{cases} q^* & = \sqrt{\frac{2Li_p^*}{(V - V_s)T}} \\ \tilde{q}^* & = 0 \end{cases} \quad \text{if} \;\; i_p^* > 0\,,$$

$$\begin{cases} q^* & = 0 \\ \tilde{q}^* & = \sqrt{\frac{2L(V - V_s)|i_p^*|}{V_s^2 T}} \end{cases} \quad \text{if} \;\; i_p^* < 0\,.$$

When $V_s > V_{s,max}$,

$$\begin{cases} q^* & = 0, \\ \tilde{q}^* & = 0. \end{cases}$$

2.2.3 Soft switching

If we use the circuit as shown in Fig. 2.2, when both switches are OFF, there is a resonant phenomenon, the voltage across the parasitic capacitors of the switches would keep oscillating. At the very beginning of next PWM cycle when one of the switches turns ON, the voltage drop across its parasitic capacitor would be some random value between the peak and valley of the oscillation. Thus the switching loss and the current varies randomly, introducing more harmonics frequencies to the system. Some researches propose the quasi-resonant switching method to tackle this problem, which is to trigger the switch when the minimum drain to source voltage of the MOSFET is detected. In this way, smallest power loss can be achieved in every switching cycle, i.e., valley switching. However, the frequency will vary and it has been claimed that this leads to higher losses for small loads, see [9], [143], [74].

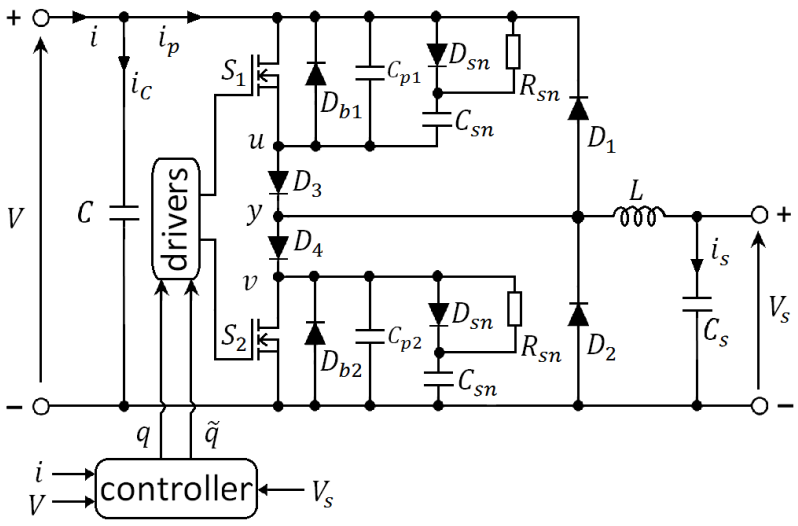

Figure 2.4: The realisation of the VIC working in DCM with soft switching, with two snubber circuits and additional diodes. The capacitors C_{p1} and C_{p2} in this figure represent the parasitic capacitances of the MOSFET transistors, while D_{b1} and D_{b2} are their body diodes.

The modification of Fig. 2.4 with respect to Fig. 2.2 are: two snubber circuits (composed of D_{sn}, R_{sn} and C_{sn}) have been added in order to insure low voltage on the switches at the moment when they switch OFF. Thus we have nearly zero voltage switching (ZVS) when switching OFF. The capacitor C_{sn} discharges slowly via R_{sn} while the switch is ON.

In Fig. 2.4, D_{b1} and D_{b2} are the body diodes of the MOSFET switches S_1 and S_2.

The capacitors C_{p1} and C_{p2} represent the parasitic capacitances of S_1 and S_2, which in reality are nonlinear. For simplicity, in the simulation, we use the energy related effective output capacitance, which is the fixed capacitance that gives the same stored energy as C_{oss} while the drain to source voltage is rising from 0 V to 390 V. D_3 and D_4 have been added to block the oscillations between L and C_{p1}, C_{p2} that would be rather strong when both switches are OFF, radiating energy and disturbing nearby devices. Instead we now have similar oscillations between L and the much smaller parasitic capacitances of D_3 and D_4. However, these oscillations carry much less energy than they would if we did not have D_3 and D_4. The voltages across the switches are more or less constant when both switches are OFF, as shown in Fig. 2.5, the general view of voltage at point y (i.e., the point between the diodes D_3 and D_4). At the instance when turning any switch ON, the current across the switch will not be zero, owing to C_{sn} discharging via R_{sn}, but it is negligible. Current i_s takes time to grow, so that we have almost zero current switching (ZCS) when switching ON. See Fig. 2.6 for the general view of the differences between hard and soft switching for VIC.

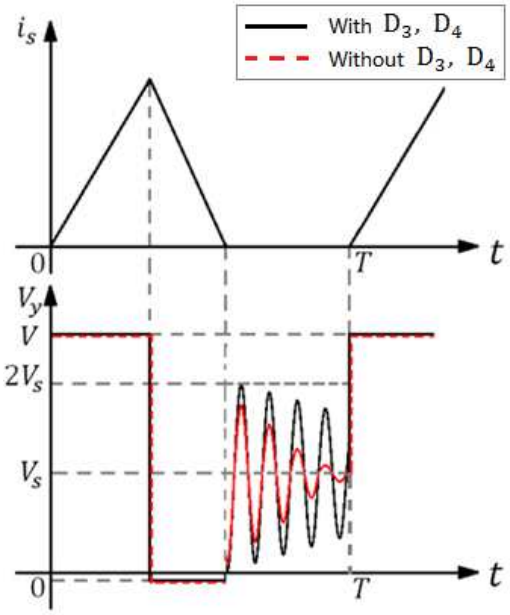

Figure 2.5: The general view of voltage at point y.

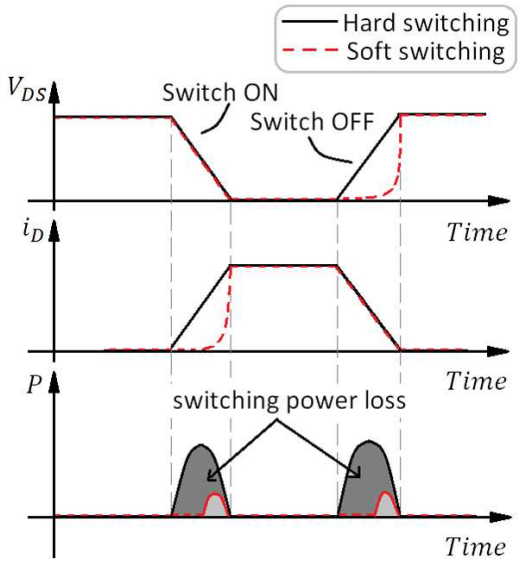

Figure 2.6: The general view of the differences between hard and soft switching for VIC. V_{DS} represents the drain to source voltage of the MOSFETs. i_D shows the current across the diodes D_3 and D_4.

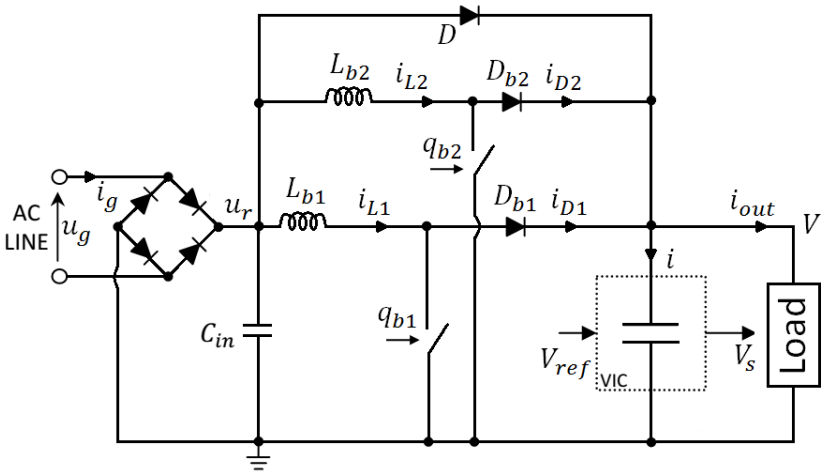

Figure 2.7: The application of the VIC as a filtering capacitor for a two-phase interleaved PFC supplying a load. The VIC controller, the charge controller and the sensors and drivers are not shown.

2.3 Simulation studies with PFC

Before applying the VIC to the wind turbine system, we firstly verify its performance by applying it in the simple two phase interleave power factor compensator (PFC) (see

Table 2.1: Simulation parameters for VIC.

Symbol	Value	Unit	Symbol	Value	Unit
u_g	$340\sin(2\pi f_g t)$	V	C	10	µF
f_g	50	Hz	C_s	47	µF
C_{in}	100	nF	V_{ref}	390	V
R	320	Ω	L_{b1}, L_{b2}	150	µH
$V_{s,min}$	100	V	L	120	µH
$V_{s,max}$	380	V	k_P	0.3142	-
$V_{s_{ref}}$	277.85	V	k_I	394.7842	-
C_{p1}, C_{p2}	158	pF	C_{sn}	1	nF
R_{sn}	500	Ω	$\phi_1/2\pi$	5	kHz
$\phi_2/2\pi$	1	kHz			

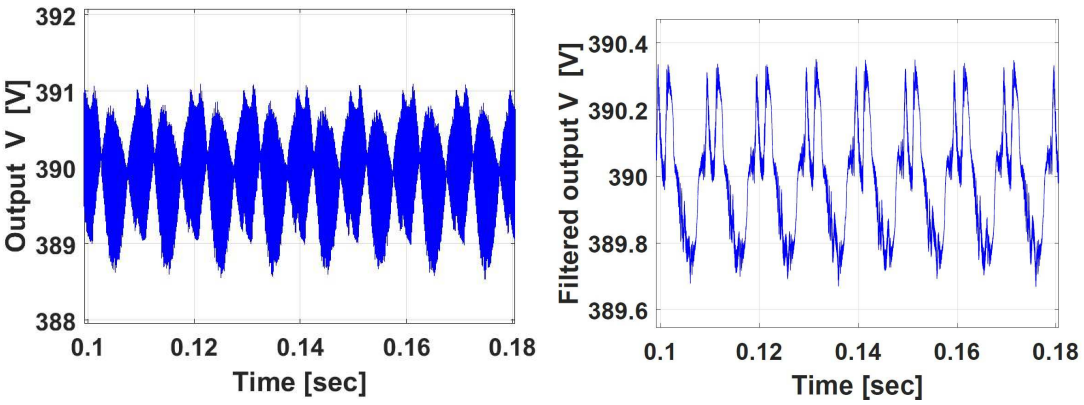

Figure 2.8: Output voltage (left) and filtered output voltage (right), filtered by a low-pass filter with corner frequency 2kHz. The low-frequency ripple amplitude is about 0.3V.

Fig. 2.7). The output filtering capacitor in PFC is replaced by VIC, with a load taking 475W at 390V. The two-phase-interleaved boost converter in the PFC operates under critical conduction mode (CRM), which means it starts the next switching cycle at the moment the current falls to zero. The ON time of the PFC switch is controlled by the charge controller, which is as in [163]. The ON time of the master phase is updated every half grid cycle and the ON time of the slave phase is adjusted instantly according to the phase lag between the master and slave phase. The phase lag is tuned by a PI controller to make them exactly out of phase. The parameter settings are are shown in table 2.1, which are based on the datasheets of the diode RFN2L6S, the MOSFET transistor $CoolMos^{TM}$ C7 IPZ60R040C7 and the 2-phase-interleaved power factor correction kit

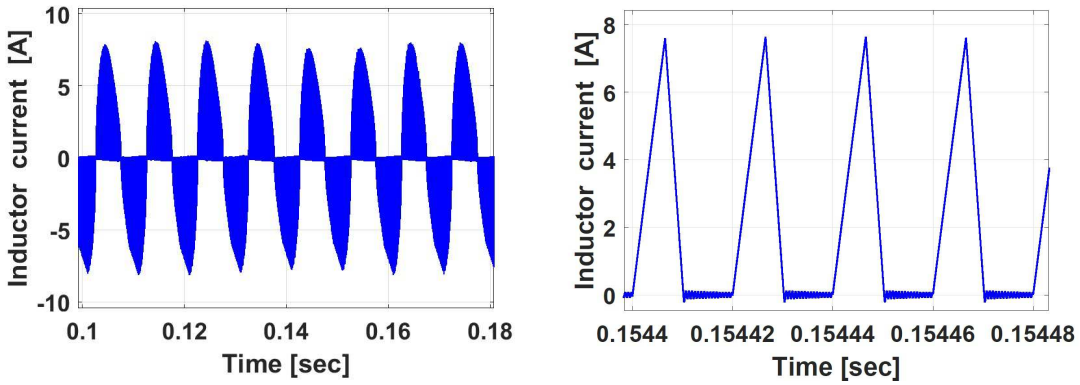

Figure 2.9: The inductor current i_s (left) and a strong zoom-in figure (right) at a moment when the converter works in buck mode.

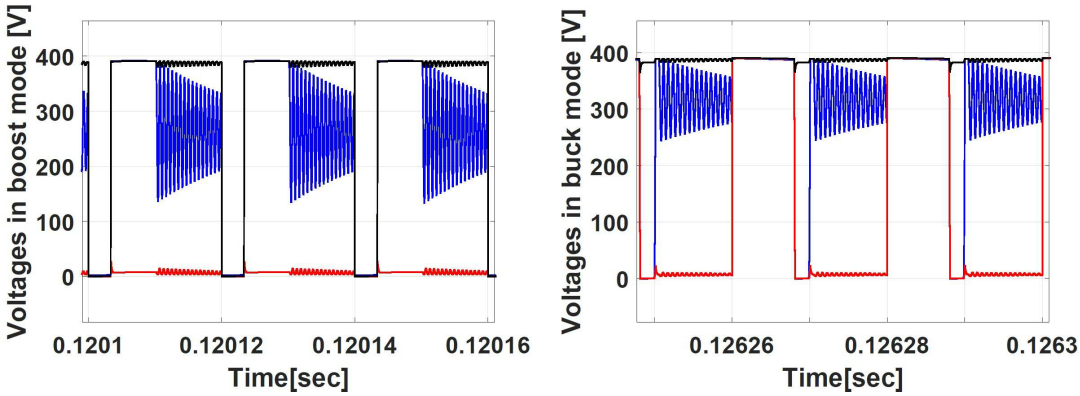

Figure 2.10: Strong zoom-in of the voltages at point u, y and v in boost operation (left) and in buck operation (right), where the red, blue and black lines represent the voltages at point u, y and v, respectively. See Fig. 2.4 for the positions of u, y and v.

TMDSILPFCKIT. The reference value for V_s is given by $V_{s_{ref}}^2 = \frac{1}{2}(V_{s,min}^2 + V_{s,max}^2)$, and the charge controller tries to bring the average of V_s^2 to $V_{s_{ref}}^2$. The sampling frequency and the switching frequency are both set to be 50 kHz. Fig. 2.8 shows the output voltage and the filtered output voltage V. It is filtered by a low pass filter with corner frequency of 2 kHz, aiming to check the ripple suppression performance of VIC without considering the influence of the fast switching. Fig. 2.9 shows the inductor current i_s and its magnifying figure, which indicating that the VIC is operating in the DCM mode. Fig. 2.10 shows the voltages at point u, y and v (see Fig. 2.4) in boost and buck operations, which is consistent with what we expected in Fig. 2.5. Fig. 2.11 shows current i which flows into VIC. It is filtered by a second order low pass filter with corner

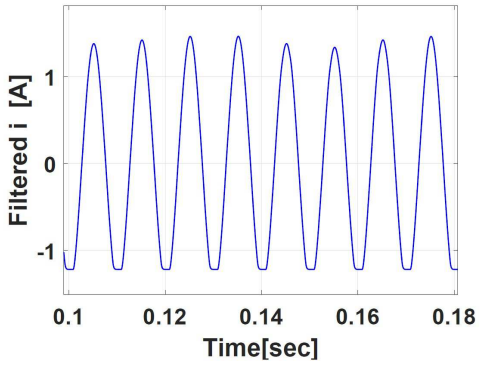

Figure 2.11: The filtered VIC current i, filtered by a second order low-pass filter with corner frequencies 5kHz and 1kHz.

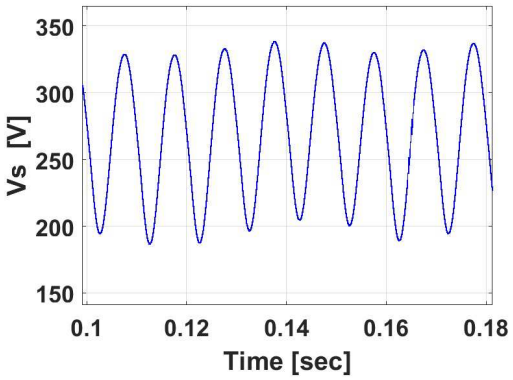

Figure 2.12: The voltage on the capacitor C_s.

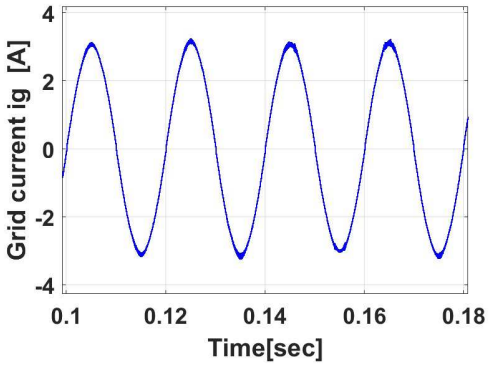

Figure 2.13: The input current to PFC (i_g).

freqiencies of 5 kHz and 1 kHz, which aims to attenuate the noise due to the switching. Fig. 2.12 shows the performance of voltage V_s. It is clear that the voltage of capacitor C_s varies while the output voltage V stays constant. Fig. 2.13 shows the input current to the PFC, which shows no visible distortions under the proper coordination between VIC controller, charge controller and the PFC controllers.

If we use a conventional capacitor to achieve a similar reduction of the low-frequency ripple as shown in Fig. 2.8 (right), for the dominant frequency $f = 100$ Hz in i, we will need to use an equivalent capacitor with capacitance approximately being

$$C_{eq} = \frac{i_{peak-peak}}{2 \times \pi \times f \times V_{peak-peak}} = 7.2mF,$$

which is about 156 times larger than $C + C_s$.

2.4 Experimental validation for VIC controller

We build up the experiment platform and conduct the experiment to verify the operation performance of VIC. The experiment is conducted in a simple and straightforward way without considering the 'charge controller'. It means that the VIC will sometimes operate exceed its desired operating range. However, during the small period of time when it is within the operating range, it is enough for us to validate the performance of the VIC controller. Then, the consistencies between the experiment and corresponding simulation performance will be presented and discussed.

2.4.1 Experiment set up

Fig. 2.14 and Fig. 2.15 show the experiment circuit and the photo of the whole experiment system respectively. The task of VIC is to remove the sinusoidal voltage provided by the auto-transformer. Note that it can suppress random fluctuations, whereas, the periodical fluctuations is applied here for easy realisation in hardware experiment. The diode D in Fig. 2.14 prevents the current flowing back to DC voltage source for protection purpose. The resistor R_p serves as short circuit protection in case of wrong switch operation. To avoid the frequent transitions between different process, the transitions between three processes are realised by state machine (see Fig. 2.16). At the moment of transition, both switches in VIC are turned OFF for one switching period as the short circuit protection.

By changing the DC voltage, the VIC may operate in different situations. When V_{DC} is small, the VIC will stay in power up process. Then as the voltage V_{DC} increase

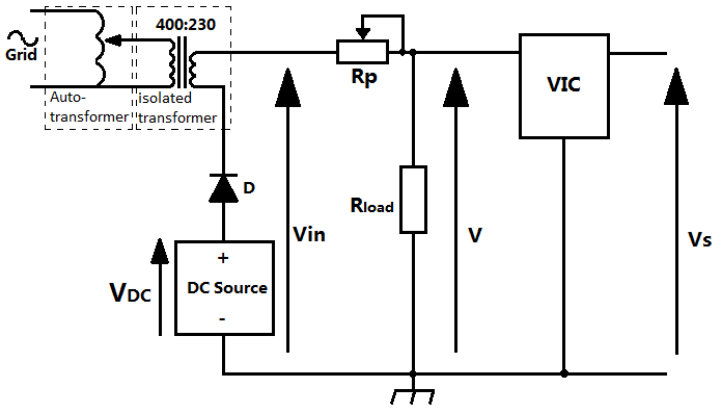

Figure 2.14: Circuit of VIC experiment to suppress the periodical voltage.

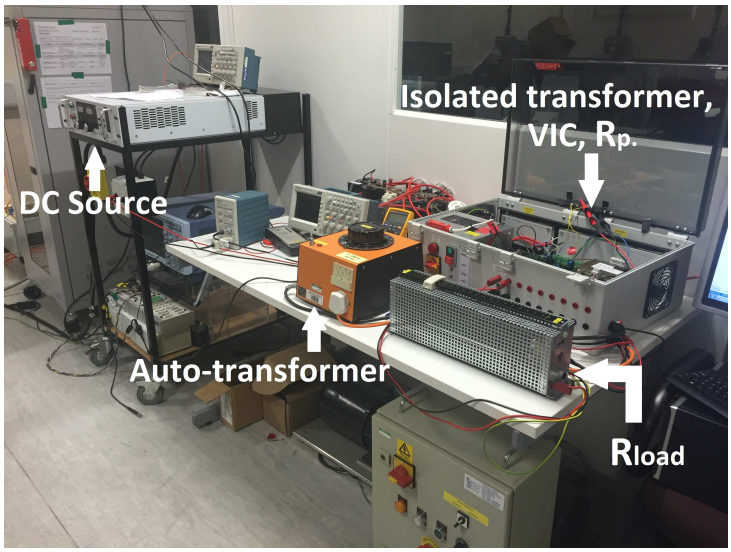

Figure 2.15: Photo of the whole experimental system. See Fig. 2.14 for R_{load} and R_p.

to certain level, the VIC will start to transit between the power up process and normal operation process periodically. If we keep increasing the V_{DC}, the VIC will start to operate between normal operation process and protection process.

In simulations, when V_{DC} is approximately 214.7 V, it will transit from power up process gradually to the protection process. During this transition, it will stay in the normal operation process for a few seconds and then it will operate in both normal operation stage and protection stage. This 'boundary' voltage is 214.3 V in experiment.

The experiment parameters and electronic components set up are shown in Table 2.2 and Table 2.3. The control algorithms are embedded into an off-the-shelf control card

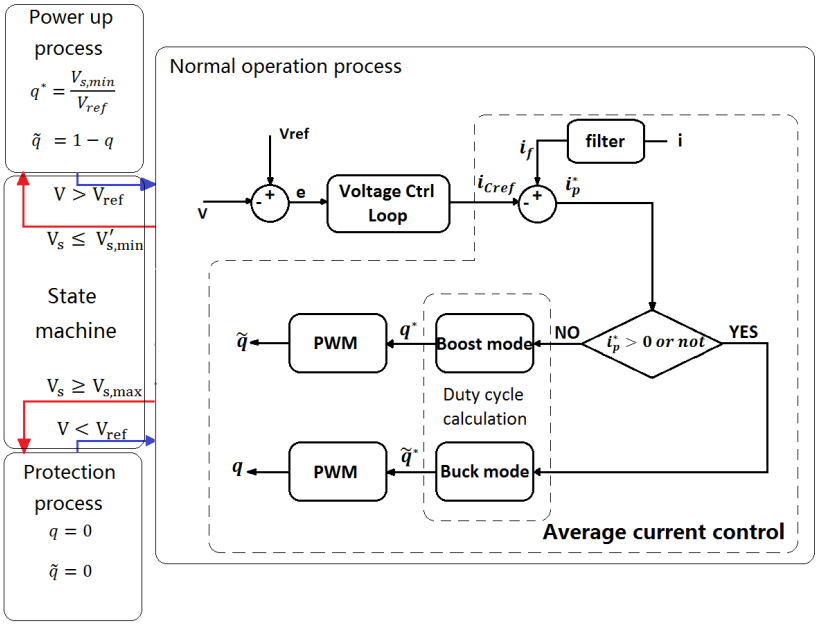

Figure 2.16: Overview of the control logic with the state machine.

Table 2.2: Experiment parameters set up.

Parameters	Setting	Unit
V_{in}	$V_{DC} + 42.5 \sin(\omega_g t)$	V
ω_g	100π	rad/s
V_{ref}	200	V
$V_{s,min}$	60	V
$V'_{s,min}$	40	V
$V_{s,max}$	180	V
$V_{s_{ref}}$	93.4	V

TMDSDOCKH52C1. A 12×16 cm four-layer printed circuit borad (PCB) is designed to implement VIC (see Fig. 2.17 and Appendix A). Electrolytic capacitors are chosen for the capacitor C and C_s, with the voltage rating of $500V$. The experiment is set up according to the circuit in Fig. 2.14.

The voltage V, V_s and current i, i_s are sensed with low pass filter in the experiment. See Fig. 2.18 for the schematic diagram of the sensing circuits. We choose different resistors and capacitors for the sensing circuit of current i, i_s and voltage V, V_s. The schematic diagram for the complete PCB design is attached in Appendix A in Page. 148.

In the current sensor, we adopt the 'floating ground' for current sensing and

Table 2.3: electronic device configurations.

Symbol	Value	Unit
C	10	µF
C_s	40	µF
R_{Load}	1000	Ω
L	120	µH
R_p	100	Ω
R_{sn}	500	Ω
C_{sn}	1	nF
C_{p1}	158	pF
C_{p2}	158	pF

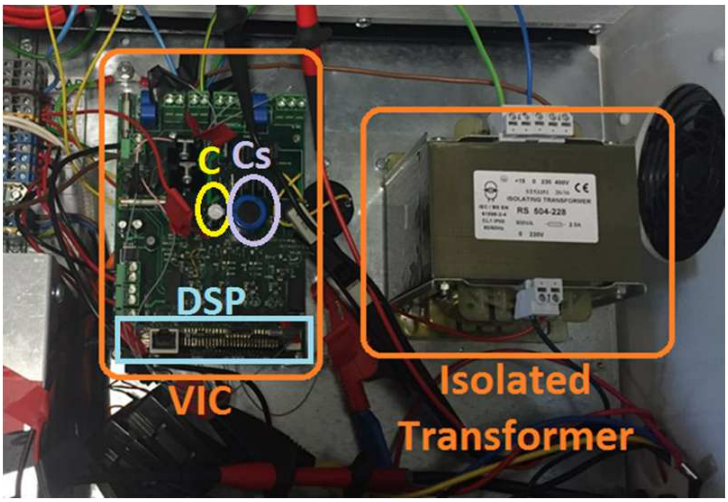

Figure 2.17: Photo of VIC and its connections.

computation, which is denoted as 'F_GND' in Fig. 2.18. The current sensor operates through sensing the voltage drop across the resistors R_1, and then computing the current via Ohm's Law. We filter the signal by two 1st-order RC filters, aiming to extract the clear average signals for computation. The corner frequency of these two filters are chosen to be 1 kHz and 5 kHz. Since the sign of the current can be altered in our experiment, we applied a floating 2.5 V voltage reference to the non-inverting input of the op-amp (denoted as $F\_2.5V$ in Fig. 2.18). In this way, the current flowing in two directions will leads to larger or smaller than 2.5 V at the sensor output V_i. C_3 is a small capacitor to filter the high frequency noise. The sensing output V_i can be expressed as

$$V_i = i_{i,i_s} \cdot 2R_1 \cdot \frac{-R_4}{R_2+R_3} \cdot \frac{\frac{R_2+R_3}{2R_2R_3C_1}}{s+\frac{R_2+R_3}{2R_2R_3C_1}} \cdot \frac{\frac{1}{R_4C_2}}{s+\frac{1}{R_4C_2}} + 2.5V, \tag{2.3}$$

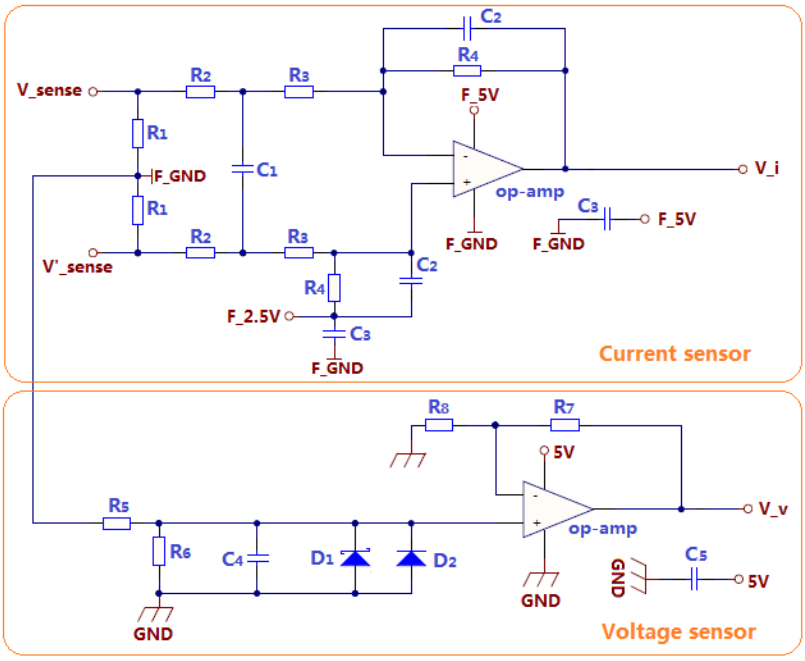

Figure 2.18: Schematic diagram of the current (i, i_s) and voltage (V, V_s) sensing circuit.

where i_{i,i_s} is the current flowing through the resistor R_1 and it is what we are going to sense. That is, the current i_{i,i_s} can be obtained by

$$i_{i,i_s} = -\frac{(R_2 + R_3)}{2R_1R_4} \cdot (V_i - 2.5), \tag{2.4}$$

The selection of resistors R_2, R_3, R_4 and capacitors C_1 and C_2 should satisfy

$$\frac{R_2 + R_3}{2R_2R_3C_1} \approx 2\pi \cdot 5000, \tag{2.5}$$

$$\frac{1}{R_4C_2} \approx 2\pi \cdot 1000. \tag{2.6}$$

The choices of resistors and capacitors to sense current i and i_s are listed in Table 2.4 and Table 2.5 respectively.

In the voltage sensor, one 1st-order RC filter is used to get rid of the high frequency noise in voltage signals. The corner frequency of this low pass filter is set to be around 5 kHz. Note that the voltage at the point 'V_{sense}' is the actual voltage we are interested. However, in this circuit, we sense the voltage at the point 'F_GND' instead. Due to the small R_1 (50 mΩ) and the small average current flowing through R_1 (within 3

Table 2.4: Resistor and capacitors in i sensing circuit.

Symbol	Value	Unit
R_1	0.05	Ω
R_2	2	kΩ
R_3	2	kΩ
R_4	40.2	kΩ
C_1	15	nF
C_2	3.9	nF
C_3	0.1	µF

Table 2.5: Resistor and capacitors in i_s sensing circuit.

Symbol	Value	Unit
R_1	0.05	Ω
R_2	3	kΩ
R_3	3	kΩ
R_4	40.2	kΩ
C_1	12	nF
C_2	3.9	nF
C_3	0.1	µF

A), the voltage differences between the point 'V_{sense}', 'V'_{sense}' and 'F_GND' are within 1 V, which is negligible in comparison with the operating voltage level (up to a few hundred volts). It means the accuracy of voltage sensing will not be influenced. The diode D_1 is the zener diode with nominal zener voltage of 5 V to protect the op-amp, and the capacitor C_5 is a small capacitor to filter the high frequency noise. The sensing output V_v can be expressed as

$$V_v = V_{V,V_s} \cdot \frac{R_6}{R_5} \cdot \frac{R_7 + R_8}{R_8} \cdot \frac{\frac{1}{R_6 C_4}}{s + \frac{1}{R_6 C_4}}, \tag{2.7}$$

where V_{V,V_s} is the voltage at the point 'F_GND'. That is, the voltage can be obtained by

$$V_{V,V_s} = \frac{R_5 R_8}{R_6(R_7 + R_8)} \cdot V_v. \tag{2.8}$$

The selection of resistors and capacitors should satisfy

$$\frac{1}{R_6 C_4} \approx 2\pi \cdot 5000. \tag{2.9}$$

See Table 2.6 for the selections of resistors and capacitors to sense the voltage V and V_s.

Table 2.6: Resistors and capacitors in V and V_s sensing circuits.

Symbol	Value	Unit
R_5	510	kΩ
R_6	3.3	kΩ
R_7	8.2	kΩ
R_8	10	kΩ
C_4	10	nF
C_5	0.1	µF

2.4.2 Experiment hazards and safety issues

We have capacitors in our circuit, which will start discharging after the power to the PCB is cut off. It may takes tens of milliseconds. That is, we cannot touch the PCB immediately at the moment of turning power off. Also, the operating voltage range of this experiment is supposed to be up to a few hundred volts, which is largely over the safety voltage level to humans and places the experiment operators under the risks of dangerous electrical shocks. Thence, we deem it compulsory to take some measures to secure the safe experiment operations.

Figure 2.19: The photo of the safety box panel.

A safety box is designed to house the VIC. The safety box panel and the circuit design for the safety box are show in Fig. 2.19 and Fig. 2.20 respectively. We can only energise the live line (230 V AC output) when we close the box lid, turn on the main switch (Switch A in Fig. 2.20) and press the RESET button (Switch E in Fig. 2.20). The magnetic open-lid switch (Switch C in Fig. 2.20) is installed to cut off the

power supply once we open the box, which prevents us from touching the PCB when the high voltage is on. Since it takes a short while to open the box, it automatically prevent us from touching the PCB during the discharging time of the capacitors. We can also manually stop the power by pressing the STOP button (Switch D in Fig. 2.20). Switch B is mechanically connected to the reed of the magnetic latching relay (Relay B in Fig. 2.20). Besides, if over voltage or over current is detected on PCB, a signal can be sent from the digital signal processor (DSP) to the safety box to trigger relay A for protection. Panel light (Light D in Fig. 2.20) will be on once the safety box is plugged into the socket and the manual switch is turned on. The lit light A, B and C indicate that the 5 V, 12 V DC output and 230 V AC output is energised respectively. The 5 V DC output is only used for the digital signals (i.e. for DSP) while the 12 V is only used for analogue signals (op amps, drivers, etc.). The digital signals are isolated from the analogue signals by the signal isolators (Part No. ISO7320, SI8431AB), which largely reduces the influences from each other. We will not lose the information in the DSP when we cut off the live line, since the 5 V and 12 V DC output is still on, which facilitates the data storing, transferring and debugging.

2.4.3 Simulation and experiment results

In this section, by changing V_{DC}, we show the performance of VIC operating in four different situations, i.e., power up process, power up – normal operation process, normal operation process, and normal operation – protection process. See Fig. 2.21 – Fig. 2.24 for the simulation and experiment results in these four situations. The simulations are conducted under the same settings as that in experiments.

During the VIC's normal operation region (see Fig. 2.23), V_{bound} are 214.7 V and 214.3 V in simulation and experiment respectively. In simulations, the 85 V voltage ripple is confined into DC voltage by VIC. The high frequency ripple in the DC voltage is about 1.5 V in simulations while it is about 7 V in the experiment. The difference may be due to some real scenarios which cannot be fully considered in the simulation, such as the EMI, the device tolerance, etc. During the protection stage (see Fig. 2.24), the voltage V_s becomes flat, which means that the capacitor C_s is disconnected. It effectively protects the C_s from being overcharged.

It is clear that the VIC performance meets our expectations. No visible low frequency ripples appear in either simulation or experiment. The experiment results are highly consistent with simulations.

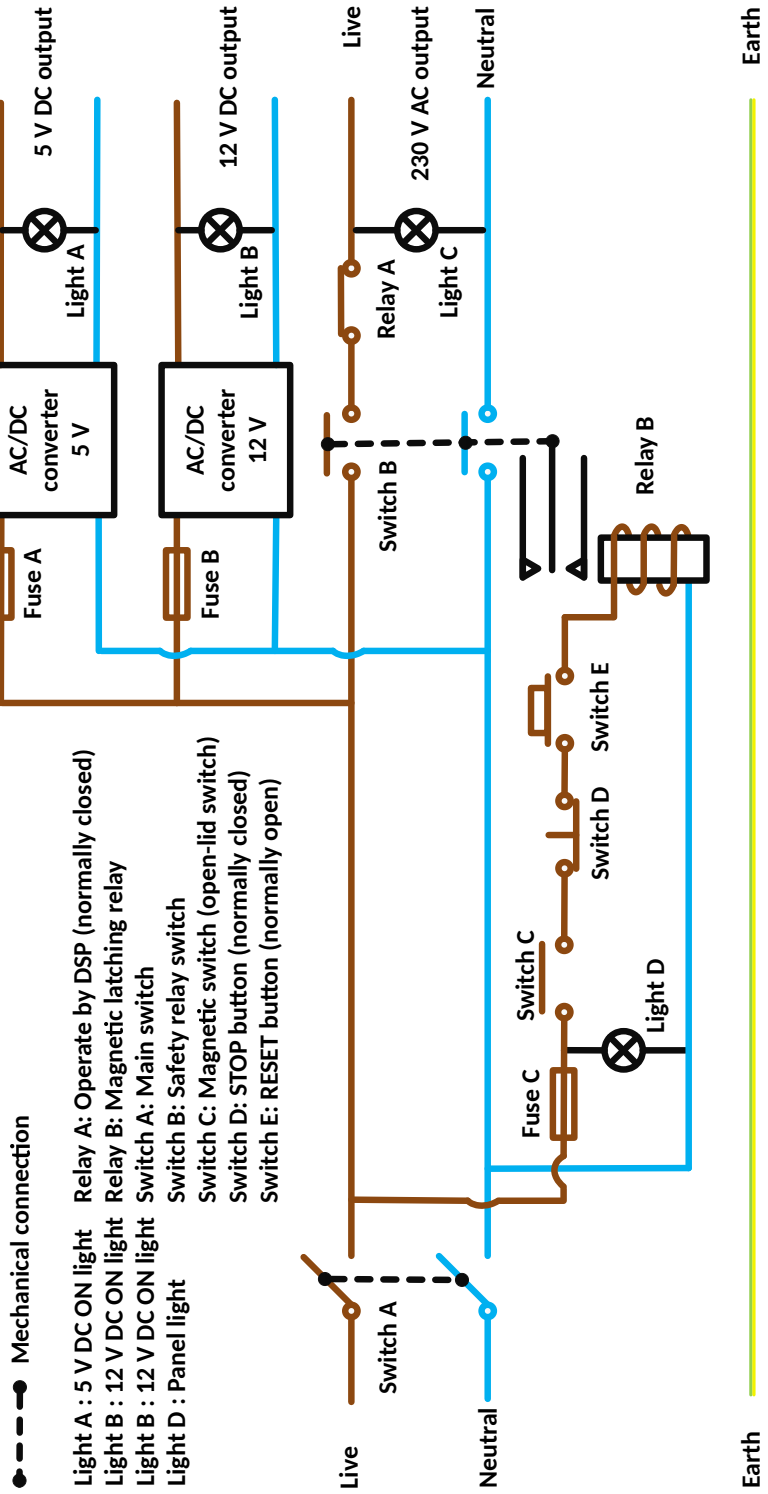

Figure 2.20: The circuit of the protection scheme of the safety box.

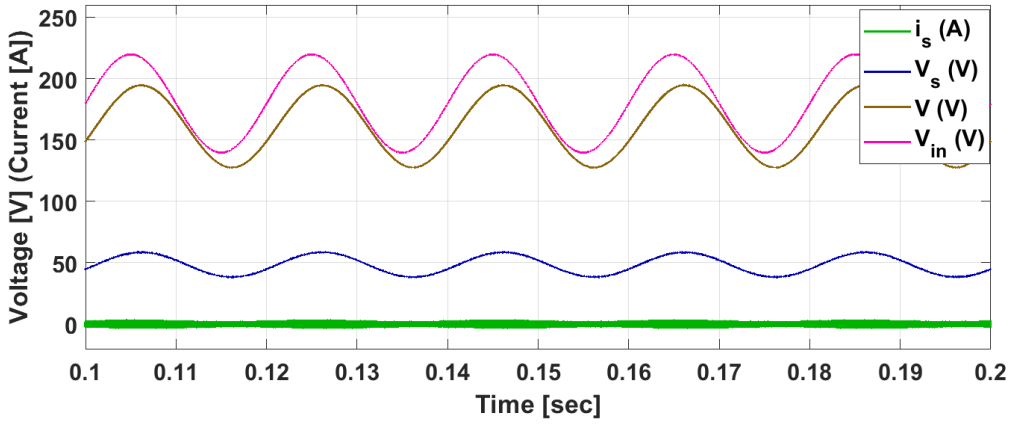

(a)

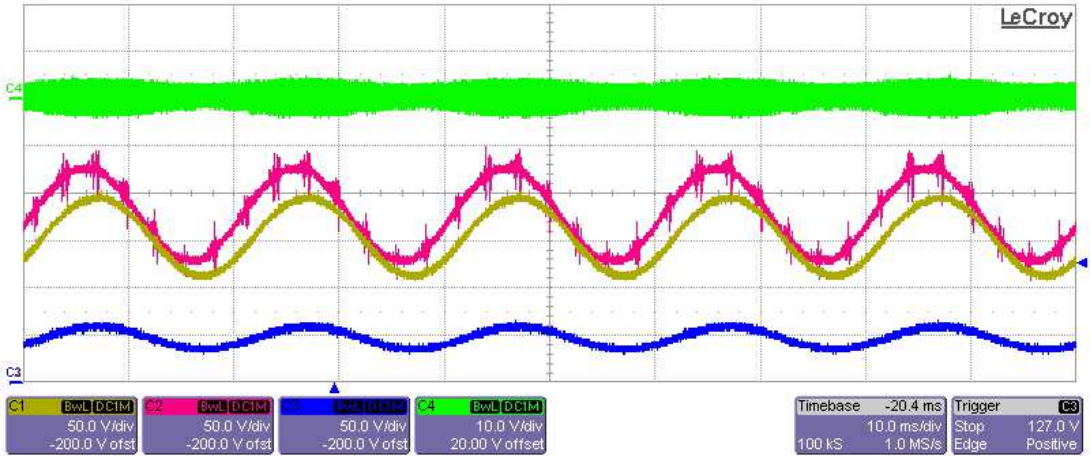

(b)

Figure 2.21: Control performance in power up process in simulation (a) and experiment (b). V_{in} is set to be $180 + 42.5sin(100\pi t)$. In the experiment, the green, pink, brown, blue signals are $i_s(A)$, $V_{in}(V)$, $V(V)$, $V_s(V)$, respectively.

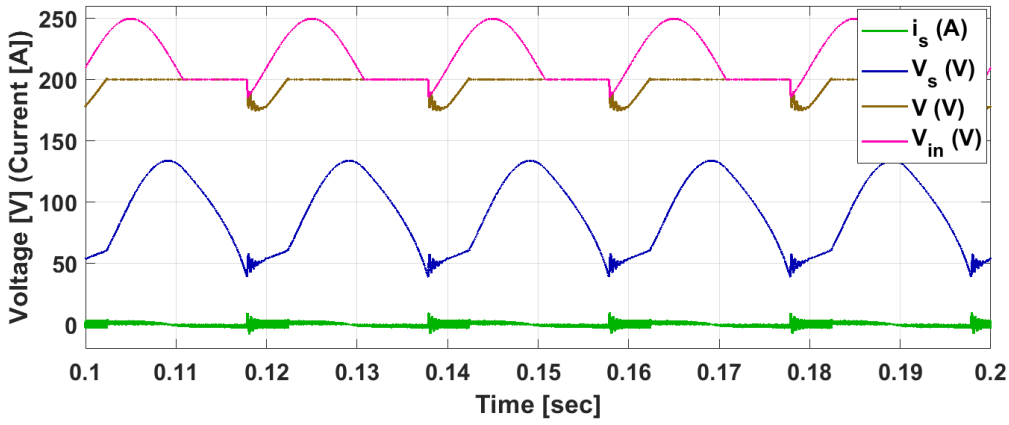

(a)

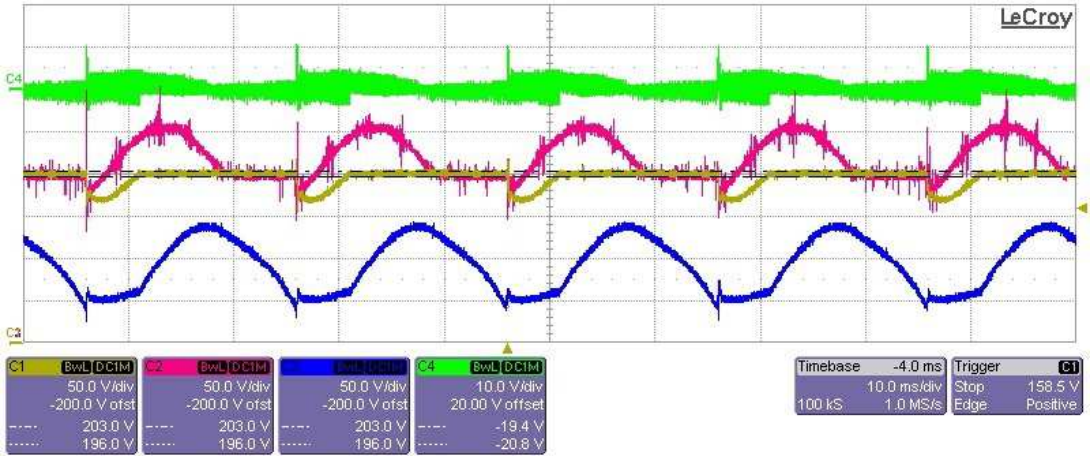

(b)

Figure 2.22: Control performance in power up – normal operation in simulation (a) and experiment (b). V_{in} is set to be $210 + 42.5sin(100\pi t)$. In the experiment, the green, pink, brown, blue signals are $i_s(A)$, $V_{in}(V)$, $V(V)$, $V_s(V)$, respectively.

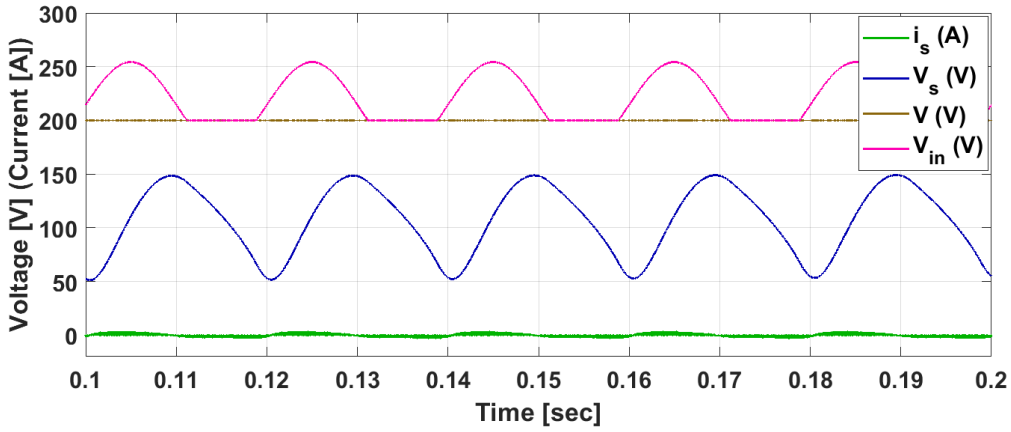

(a)

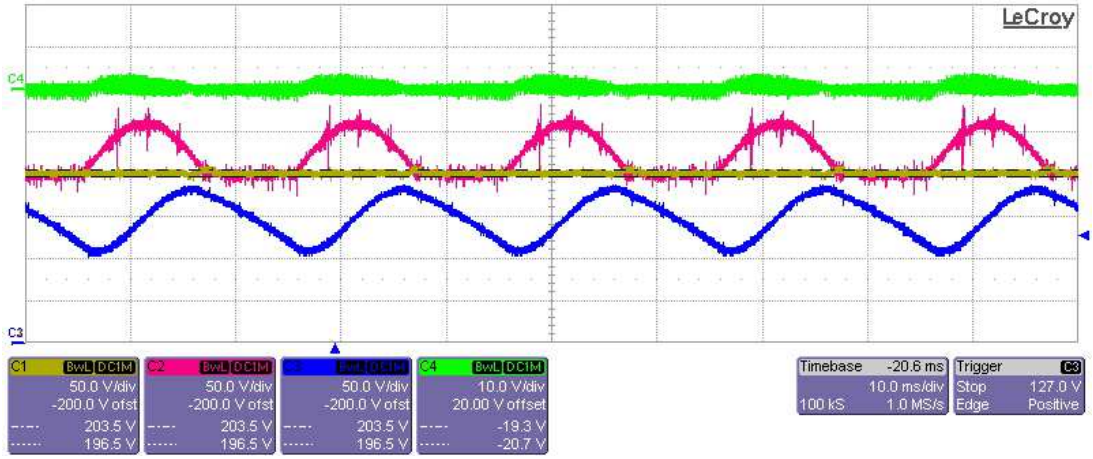

(b)

Figure 2.23: Control performance in normal operation process in simulation (a) and experiment (b). V_{in} is set to be $V_{bound} + 42.5sin(100\pi t)$. In the experiment, the green, pink, brown, blue signals are $i_s(A)$, $V_{in}(V)$, $V(V)$, $V_s(V)$, respectively.

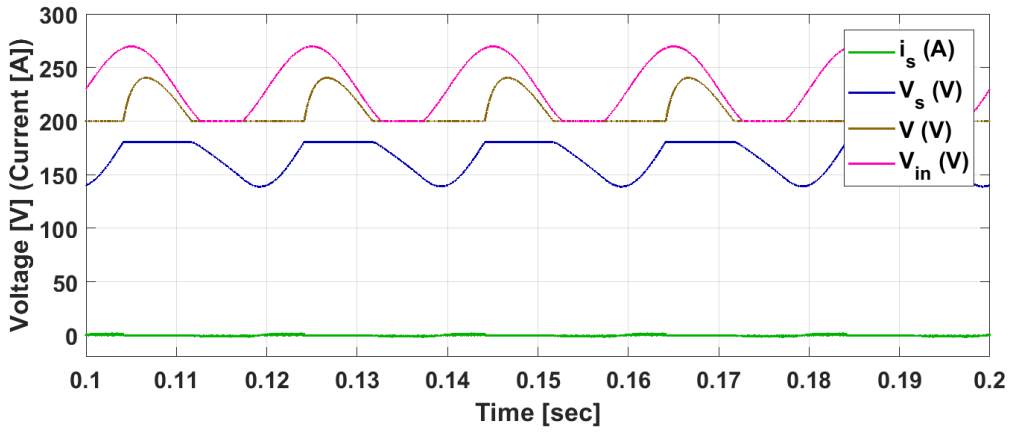

(a)

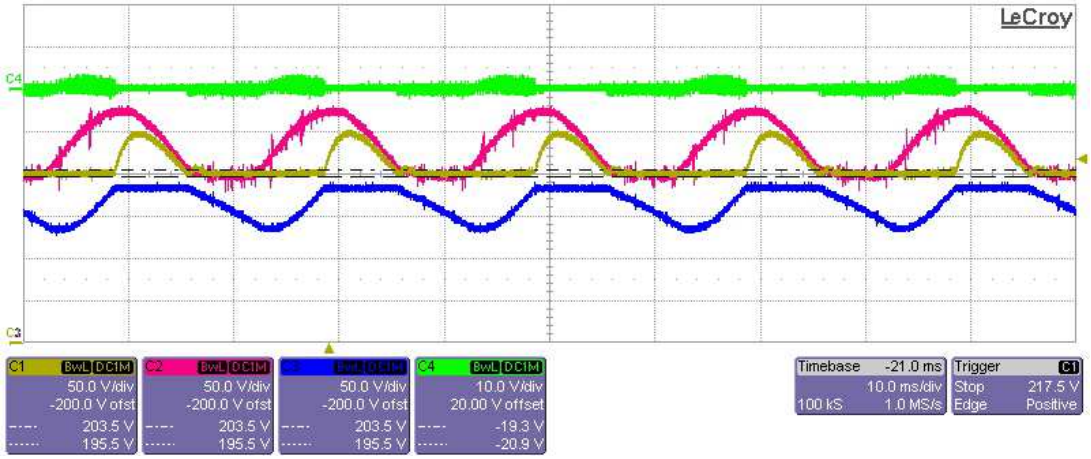

(b)

Figure 2.24: Control performance in normal operation – protection process in simulation (a) and experiment (b). V_{in} is set to be $230 + 42.5sin(100\pi t)$. In the experiment, the green, pink, brown, blue signals are $i_s(A)$, $V_{in}(V)$, $V(V)$, $V_s(V)$, respectively.

2.5 Conclusions

We proposed a control algorithm to control the VIC, which included a close-loop voltage control and an open-loop current control based on the average model of the VIC. We also proposed an improved realisation of the VIC to achieve soft switching. We firstly verified the designed control system by applying it in a PFC circuit as the output filter capacitor. The simulation results implied that VIC provided outstanding performance in voltage ripple suppression. Then to further validate the designed control system, we experimentally tested the VIC in a simple and straightforward way. We created a 50 Hz, 85 $V_{peak-peak}$ sinusoidal ripple through the auto-transformer and fed it to the VIC together with a DC voltage. The VIC was expected to remove this sinusoidal voltage and extract the DC voltage at its output terminal. Our experiment results showed outstanding ripple suppression performances of VIC, which were highly consistent with the corresponding simulation results. The experiment tests demonstrated the possibility to substitute the DC-link capacitor with VIC in wind power integration system and use VIC in other industrial systems.

Chapter 3

The Parallel Virtual Infinite Capacitor Applied to DC-Link Voltage Filtering for Wind Turbine

The VIC proposed in Chapter 2 provides the possibility to replace the fragile and expensive DC-link capacitor for voltage filtering. However, the DC-link voltage usually includes ripples in two distinct frequency ranges while the VIC mainly aims to filter the ripple in one frequency range. Hence, in this chapter, we further develop the VIC into a parallel virtual infinite capacitor (PVIC) for the wind turbine, aiming to suppress voltage variations in a wider frequency range than a usual VIC. We also design a new snubber circuit to further reduce the energy loss. The PVIC is composed of two VICs which is connected to the same DC link and share one capacitor, with one tuned to low frequency (LF) and the other tuned to high frequency (HF). The LF-VIC is controlled by a sliding mode controller (SMC) to regulate the LF component of the voltage to its reference value, and maintain its state of charge (SoC) within the desired range by a PI controller. The HF-VIC is controlled by another SMC to limit the HF ripples and also to keep its SoC within a reasonable operating interval. Then we use the PVIC to replace a DC-link capacitor in wind power integration system and run the simulations under different grid conditions with turbulent wind input. The simulation results show that the PVIC provides better voltage stabilisation performance than a DC-link capacitor with the same capacitance. See these results also in our paper [85, 86].

3.1 Introduction

The energy generated from wind has occupied an increasing proportion of the total energy generated worldwide, and the wind power will continue to be an important source for electric power. At the end of 2017, the cumulative installed wind turbine capacity was over 539 GW, which can cover over 5% of the electric power demand of the world. Wind power capacity is expected to rise to 840 GW in 2020 [158, 46]. Doubly fed induction generators (DFIG) have been widely used for wind turbines with power ratings of 1.5-MW and above since 1996 [112].

A DFIG wind turbine is quite vulnerable to grid faults because the DFIG stator is directly connected to the grid. Grid faults may cause voltage variations at the DFIG terminals, which may lead to low or high currents in rotor windings causing the DC-link voltage to drop, preventing the converters from working, or to rise too high, which may damage the capacitors and IGBTs [98, 161]. During grid faults, the DC-link voltage should be maintained at the normal level to enable the converters to apply the voltage ride through algorithm, especially to guarantee the control performance of the rotor side converter. Even without grid faults, DC-link voltage fluctuations need to be limited to guarantee accurate power regulation [161]. Some electronic circuits used for active ripple suppression on the DC link of wind turbine have been proposed (see [62, 104] and the references therein). Fig. 3.1 shows the configuration of a DFIG driven by a 1.5-MW wind turbine connected to the power grid via back-to-back converters and transformers. Typically, the rotor side converter is controlled to maximize wind power extraction, and the grid side converter is controlled to stabilise the DC-link voltage. In Chapter 2, we have propose the VIC as the alternative to the DC-link capacitor in the grid integration system of the wind turbines.

However, when we compute the output impedance of a VIC (as is done, for instance, in [81]), we find that it is high for frequencies near zero (as it should), it has a region where it is very low (as desired), but it grows for higher frequencies. The region of low impedance depends on the control algorithm. The DC-link voltage filtering in wind power integration system is this kind of application where there are two main sources of ripple, in two distinct frequency range. The DC-link voltage ripple can originate from variations of wind speed (low frequency), grid imbalance (twice the grid frequency) and switching ripple from the main converters (relatively high frequency). To deal with such situations, we introduce here the PVIC concept.

The PVIC is composed of two VICs, one for low-frequency (LF) and one for high frequency (HF), which share a common capacitor. We also propose a new soft switching

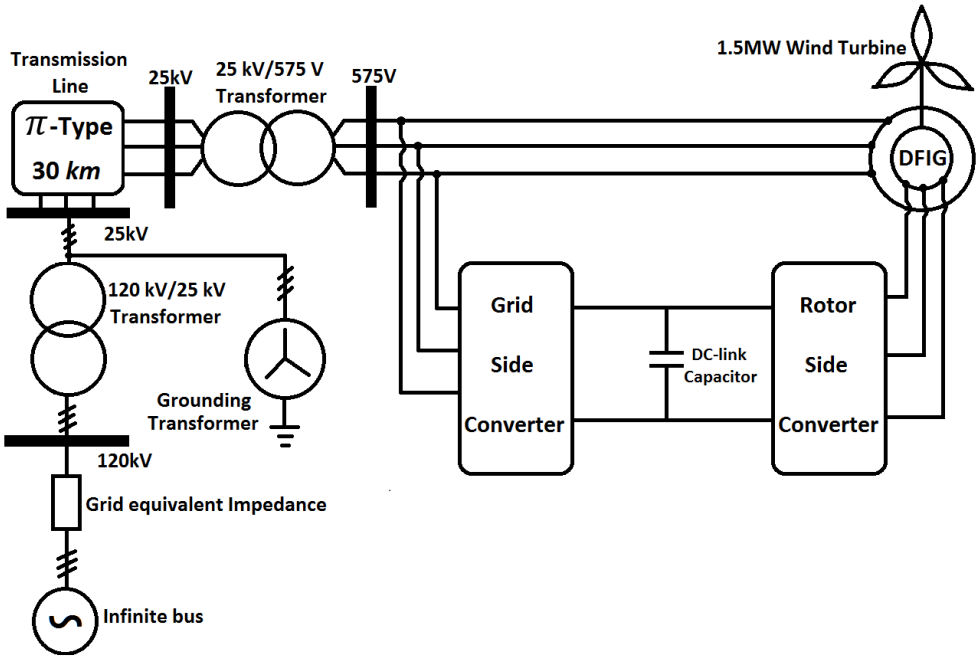

Figure 3.1: Configuration of the grid-connected doubly fed induction generator (DFIG) wind turbine system.

topology (see Fig. 3.2) to be used for both the LF-VIC and the HF-VIC, which of course improves the efficiency compared with earlier designs (Fig. 2.4). The operation of this new circuit will be explained in Section 3.2. For the LF-VIC, we design a sliding mode controller (SMC) to regulate the DC-link voltage in the frequency range of this VIC. A proportional-integral (PI) controller is used to maintain the charge in this VIC in its normal operating range and realise the 'plug-and-play' feature of the PVIC. Another SMC is designed for the HF-VIC to suppress the high-frequency component of the ripple voltage and at the same time to keep the state of charge (SoC) of this VIC within the normal operating range. Note that sliding mode controllers are robust and appropriate for nonlinear variable structure systems [39, 106, 147, 148] such as power converters [139, 138, 150, 8, 45].

In this chapter, the PVIC is applied to replace the DC-link capacitor for DC-link voltage filtering of a 1.5-MW DFIG wind turbine system. We use a grid-connected DFIG model [96, 97], driven by the popular WindPACT (WP) 1.5-MW wind turbine [72, 129, 91] under turbulent wind generated by NREL Turbsim [70]. We have replaced the DC-link capacitor seen in Fig. 3.1 with a PVIC with the same total capacitance and we compare the performance of the DC-link capacitor with that of the PVIC in

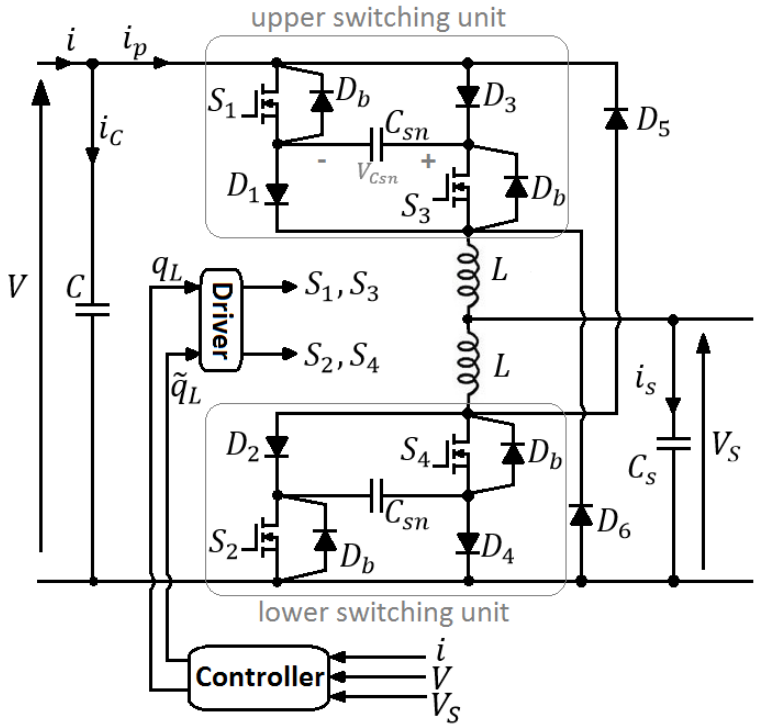

Figure 3.2: The proposed new VIC circuit, D_b, denotes a body diode of a MOSFET switch.

stabilizing the DC-link voltage. The comparisons under different grid faults demonstrate the capability of the PVIC in handling unpredictable voltage fluctuations. In order to introduce disturbances to the DC link, we have simulated faults at the infinite bus. The simulations indicate that the PVIC is more effective in suppressing the voltage fluctuations than the equivalent DC-link capacitor (i.e., a DC-link capacitor with the same capacitance), regardless if there are grid disturbances or not.

The structure of this chapter is as follows. In Section 3.2, we briefly explain the operation principle and control of the VIC and especially the soft switching version from Figure 3.2. In Section 3.3, we present our simulation results for the DC-link voltage filtering performance of the PVIC. We compare the performance of the PVIC with that of the equivalent (in capacitance) DC-link capacitor.

3.2 The PVIC and its control

To improve efficiency, we use a new soft switching circuit shown in Fig. 3.2, where the two snubber capacitors C_{sn} are small. This is an improvement of the circuit appearing

in Fig. 2.4. The upper switching unit is composed of the S_1, S_3, C_{sn}, D_1 and D_3, in which S_1 is synchronized with S_3. The lower switching unit is similar. The inductors are not coupled.

We take the upper switching unit (see Fig. 3.2) as an example to explain the soft switching mechanism. Actually, this is soft switching only in discontinuous conduction mode (DCM), while in continuous conduction mode (CCM) it is only zero voltage switching-off. Immediately after S_1 and S_3 are turned off, the voltage on the left side of C_{sn} will remain close to V without dropping abruptly because C_{sn} takes time to get charged via D_1 and D_3 until $V_{C_{sn}}$ reaches V, which implies zero voltage switching-off of S_1 and S_3. The main current will flow via D_6, decreasing at a slope of $-V_s/L$, until one of the following two events occurs: either the current reaches zero and then remains zero for some time (DCM) or the switches are controlled to turn on again. Immediately after S_1 and S_3 are turned on, the voltage on the right side of C_{sn} will suddenly jump to $V + V_{C_{sn}} \approx 2V$. Then C_{sn} starts to release energy through the switches and the upper inductor L to charge C_s, until $V_{C_{sn}}$ reaches nearly zero or the switches are controlled to turn off. This discharging period of C_{sn} is relatively short because the time constant $\sqrt{LC_{sn}}$ is small. Hence practically all the energy that was stored in C_{sn} is saved into C_s. However, if the inductor current at the moment of switching-on is not zero, we do not have zero current switch-on. After switch-on and after C_{sn} is emptied, the inductor current (flowing through the switches and the diodes D1 and D3) grows, at a slope of $(V - V_s)/L$. Of course, the rising current will stop once the switches are turned off, which closes the whole cycle. The story for the lower switching unit is similar.

Fig. 3.3 shows the circuit realisation of a PVIC, which replaces the DC-link capacitor. $q_L,\ \tilde{q}_L \in \{0,\ 1\}$ are binary signals and $\tilde{q}_L = 1 - q_L$. The switches S_{1_L} and S_{3_L} are on if $q_L = 1$. The switches S_{2_L} and S_{4_L} are on if $\tilde{q}_L = 1$. The binary signals q_H and $\tilde{q}_H$ are defined in a similar way. The capacitor C_{s_H} is smaller than the capacitor C_{s_L}. The remaining components in the HF-VIC are same as in the LF-VIC. The control of PVIC is attained by the LF-VIC controller and HF-VIC controller. The former regulates low-frequency components of the voltage V to the neighbourhood of its reference while the latter suppresses the high-frequency ripples of the voltage V. During the power up process (see the left segment in Figure 2.1), a constant duty cycle D_{pow_up} and a constant PWM switching frequency f_{pow_up} are applied to both VICs. During the protection region of operation (the right segment in Figure 2.1), all the switches are turned off to avoid the overcharge of C_{s_L} and C_{s_H}. The transitions between the three processes are controlled using a state machine, which was detailed in our paper [83]. Next we discuss the control algorithm in the normal operation range.

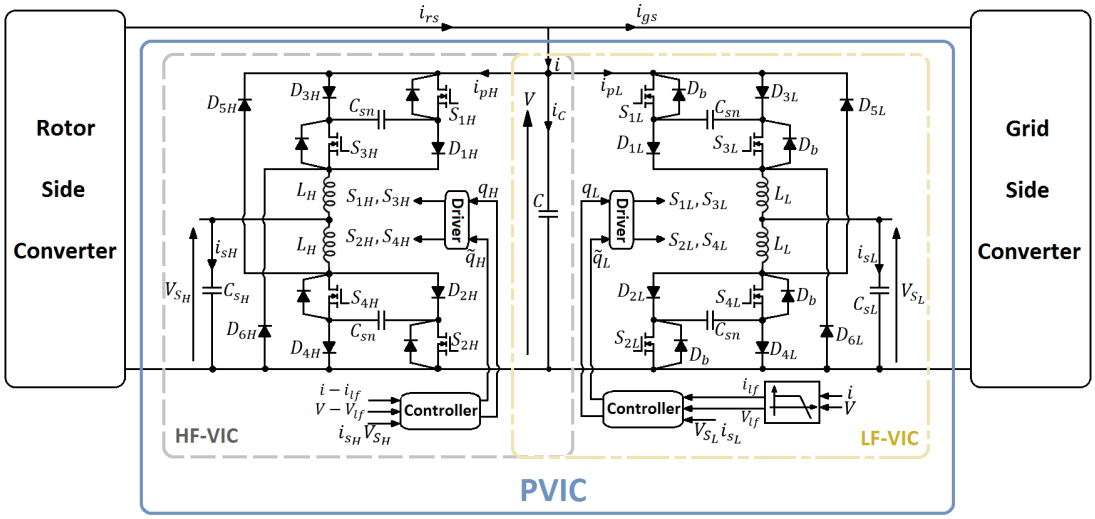

Figure 3.3: The PVIC in place of a DC-link capacitor.

The low-frequency signals (V_{lf}, i_{lf}) and high-frequency signals (V_{hf}, i_{hf}) are acquired by passing V and i through a low pass filter with the corner frequency f_l:

$$\begin{cases} V_{lf} = \frac{2\pi f_l}{s + 2\pi f_l} V, \\ V_{hf} = V - V_{lf}, \\ i_{lf} = \frac{2\pi f_l}{s + 2\pi f_l} i, \\ i_{hf} = i - i_{lf}. \end{cases} \tag{3.1}$$

According to Fig. 3.3, we have

$$i_C = C\dot{V} = i - q_L i_{s_L} - q_H i_{s_H}. \tag{3.2}$$

Considering (3.1), we can rewrite (3.2) as

$$C\left(\dot{V}_{lf} + \dot{V}_{hf}\right) = i_{lf} + i_{hf} - q_L\left(i_{s_{L_L}} + i_{s_{L_H}}\right) - q_H\left(i_{s_{H_L}} + i_{s_{H_H}}\right), \tag{3.3}$$

where $i_{s_{L_L}}$, $i_{s_{L_H}}$, $i_{s_{H_L}}$, and $i_{s_{H_H}}$ are defined by

$$\begin{aligned} i_{s_{L_L}} &= \frac{2\pi f_l}{s \ + \ 2\pi f_l} i_{s_L}, \\ i_{s_{L_H}} &= i_{s_L} - i_{s_{L_L}}, \\ i_{s_{H_L}} &= \frac{2\pi f_l}{s \ + \ 2\pi f_l} i_{s_H}, \\ i_{s_{H_H}} &= i_{s_H} - i_{s_{H_L}}. \end{aligned} \tag{3.4}$$

Multiplying both sides of (2) with $\frac{2\pi f_l}{s \ + \ 2\pi f_l}$, we get

$$C\dot{V}_{lf} = i_{lf} - q_L i_{s_{L_L}} - q_H i_{s_{H_L}}. \tag{3.5}$$

Subtracting (3.5) from (3.2), we get

$$C\dot{V}_{hf} = i_{hf} - q_H i_{s_{H_H}} - q_L i_{s_{L_H}}.$$

Then the state equations of the PVIC can be written as:

$$\begin{cases} C\dot{V}_{lf} = i_{lf} - q_L i_{s_{L_L}} - q_H i_{s_{H_L}}, \\ C\dot{V}_{hf} = i_{hf} - q_H i_{s_{H_H}} - q_L i_{s_{L_H}}, \\ L_L \dot{i}_{s_L} = q_L(V_{lf} + V_{hf}) - V_{s_L}, \\ L_H \dot{i}_{s_H} = q_H(V_{hf} + V_{lf}) - V_{s_H}, \\ C_{s_L} \dot{V}_{s_L} = i_{s_L}, \\ C_{s_H} \dot{V}_{s_H} = i_{s_H}. \end{cases} \tag{3.6}$$

These state equations are considered only in the operating range, which is Ω defined by:

$$\Omega = \begin{cases} i_{s_L} \in [-i_{smax_L}, i_{smax_L}], \\ i_{s_H} \in [-i_{smax_H}, i_{smax_H}], \\ V_{s_L} \in [V_{smin_L}, V_{smax_L}], \\ V_{s_H} \in [V_{smin_H}, V_{smax_H}], \\ V_{lf} > V_{min_L}, \\ \left|V_{hf}\right| < V_{max_H}. \end{cases} \tag{3.7}$$

Note that $0 < V_{s_{min_L}} < V_{s_{max_L}} < V_{min_L} < V_{ref} < V_{max_L}$ and $0 < V_{max_H} < V_{s_{min_H}} < V_{s_{max_H}}$. For subsequent analysis, we set the following lower and upper bounds:

$$\begin{cases} V \in [0, V_{max_L} + V_{max_H}], \\ i_{lf} \in [-i_{max_L}, i_{max_L}], \\ i_{hf} \in [-i_{max_H}, i_{max_H}], \\ i_{s_{H_L}} \in [-i_{smax_{HL}}, i_{smax_{HL}}], \\ i_{s_{H_H}} \in [-i_{smax_{HH}}, i_{smax_{HH}}], \\ i_{s_{L_L}} \in [-i_{smax_{LL}}, i_{smax_{LL}}], \\ i_{s_{L_H}} \in [-i_{smax_{LH}}, i_{smax_{LH}}]. \end{cases} \tag{3.8}$$

3.2.1 Control of the LF-VIC

The LF-VIC controller is composed of a sliding mode voltage controller and a PI charge controller. Their control objectives are to control the low-frequency component of the voltage to its expected reference in normal operation process and, restrain the LF-VIC's SoC within its normal operating range, respectively.

Voltage Control of the LF-VIC

We use a SMC to regulate the low-frequency component of V. We employ a sliding function with the states $x = \begin{bmatrix} V_{lf} & i_{s_L} & V_{s_L} \end{bmatrix}^T$ and disturbance i_{lf}, based on ([163], Section 6):

$$\begin{aligned} S_L(x) =& (V_{ref} - V_{lf}) + k_1 \int_0^t (V_{ref} - V_{lf}) d\tau \\ & - k_2 (V_{ref} i_{lf} - V_{s_L} i_{s_L}), \end{aligned} \tag{3.9}$$

where we set $k_1 > 0$. The sliding surface Γ_L is the set of all the possible $x \in \Omega$ for which

$$S_L(x) = 0. \tag{3.10}$$

Note that the energy stored in the two inductors of the PVIC can be roughly written as $V_{ref} i_{lf} + V_{ref} i_{hf} - V_{s_L} i_{s_L} - V_{s_H} i_{s_H}$. The nonlinear term $V_{ref} i_{lf} - V_{s_L} i_{s_L}$ in (3.9) represents the energy in L_L. The remaining part $V_{ref} i_{hf} - V_{s_H} i_{s_H}$, which represents the energy in L_H, is included in the HF-VIC controller. This will be discussed in Section

3.2.2. The absolute values of k_1 and k_2 should be small enough to diminish deviation between V_{lf} and V_{ref} when x is controlled to be within Γ_L.

To reduce chattering effects and limit operating frequencies within a controllable range, we use the hysteresis-modulation (HM) sliding mode control [139] to determine the binary switching signals q_L and $\tilde{q}_L$:

$$\begin{cases} q_L = \begin{cases} 1, \text{if } S_L < -\epsilon, \\ 0, \text{if } S_L > \epsilon, \\ \text{previous state, if } S_L \in [-\epsilon, \epsilon]. \end{cases} \\ \tilde{q}_L = 1 - q_L, \end{cases} \tag{3.11}$$

where ϵ is a small positive number. In the stability analysis later, we assume $\epsilon = 0$ for simplicity but without loss of generality.

The SMC is designed according to the following steps. Firstly, the hitting condition should be satisfied to ensure that the state trajectory is guided to the sliding surface. After that, when the states are within a small vicinity of the sliding surface, the existence condition needs to be satisfied to maintain the states within the neighbourhood of the sliding surface and always direct the states towards the desired surface [138, 39].

In this chapter, we describe the hitting condition by

$$S_L(x) \cdot \dot{S}_L(x) < 0 \quad \text{for all } x \in \Omega \backslash \Gamma_L, \tag{3.12}$$

where

$$\begin{aligned} \dot{S}_L(x) = &- \dot{V}_{lf} + k_1(V_{ref} - V_{lf}) \\ &- k_2(V_{ref}\dot{i}_{lf} - V_{s_L}\dot{i}_{s_L} - \dot{V}_{s_L} i_{s_L}). \end{aligned} \tag{3.13}$$

Combining (3.6) and (3.13), we get

$$\begin{aligned} \dot{S}_L(x) = &- \frac{i_{lf} - q_L i_{s_{L_L}} - q_H i_{s_{H_L}}}{C} + k_1(V_{ref} - V_{lf}) \\ &+ k_2(\frac{q_L(V_{lf} + V_{hf})V_{s_L} - V_{s_L}^2}{L_L} + \frac{i_{s_L}^2}{C_{s_L}} - V_{ref}\dot{i}_{lf}). \end{aligned} \tag{3.14}$$

When $S_L(x) > 0$ for all $x \in \Omega \backslash \Gamma_L$, $q_L = 0$. To satisfy (3.12), we require that

$$\begin{aligned} \dot{S}_L = &- \frac{i_{lf} - q_H i_{s_{H_L}}}{C} + k_1(V_{ref} - V_{lf}) \\ &+ k_2(-\frac{V_{s_L}^2}{L_L} + \frac{i_{s_L}^2}{C_{s_L}} - V_{ref}\dot{i}_{lf}) < 0. \end{aligned} \tag{3.15}$$

Here, $\dot{i}_{lf}$ is set to be $\dot{i}_{lf} \in [-\dot{i}_{max_L}, \dot{i}_{max_L}]$. Note that it is hard to limit a current derivative term in reality. This limit is allowed to be violated under some circumstances such as the abrupt current change due to some faults. However it will be brought back by the control schemes. A sufficient condition for (3.15) is

$$\begin{aligned} &\dot{S}_{Lmax} \leq k_1(V_{ref} - V_{min_L}) + k_2(-\frac{V_{smin_L}^2}{L_L} + \frac{i_{smax_L}^2}{C_{s_L}} \\ &+V_{ref}\dot{i}_{max_L}) + \frac{i_{max_L} + i_{smax_{HL}}}{C} < 0. \end{aligned} \tag{3.16}$$

When $S_L(x) < 0$ for all $x \in \Omega \backslash \Gamma_L$, $q_L = 1$. To satisfy (3.12), we have

$$\begin{aligned} \dot{S}_L = &- \frac{i_{lf} - q_H i_{s_{H_L}} - i_{s_{L_L}}}{C} + k_1(V_{ref} - V_{lf}) \\ &+ k_2(\frac{(V_{lf} + V_{hf})V_{s_L} - V_{s_L}^2}{L_L} + \frac{i_{s_L}^2}{C_{s_L}} - V_{ref}\dot{i}_{lf}) > 0. \end{aligned} \tag{3.17}$$

A sufficient condition for (3.17) is

$$\begin{aligned} \dot{S}_{Lmin} \geq \; & k_1(V_{ref} \; - \; V_{max_L}) \\ & + \; k_2(\frac{V_{smax_L}(V_{min_L} \; - \; V_{max_H}) \; - \; V_{smax_L}^2}{L_L} \\ & - \; V_{ref}\dot{i}_{max_L}) \; - \; \frac{i_{max_L} \; + \; i_{smax_{LL}} \; + \; i_{smax_{HL}}}{C} > 0. \end{aligned} \tag{3.18}$$

From (3.16) and (3.18) we set

$$\begin{cases} k_1 > 0, \qquad\qquad k_2 > 0, \\ 0 < \dot{i}_{max_L} < minF_{Lb}, \\ F_{Lb} = \left\{ \frac{V_{s_{min_L}}^2}{L_L V_{ref}} \; - \; \frac{i_{smax_L}^2}{C_{s_L} V_{ref}}, \frac{V_{s_{max_L}}(V_{min_L} \; - \; V_{s_{max_L}} \; - \; V_{max_H})}{L_L V_{ref}} \right\}, \end{cases} \tag{3.19}$$

where F_{Lb} is derived from

$$-\frac{V_{smin_L}^2}{L_L} + \frac{i_{smax_L}^2}{C_{s_L}} + V_{ref}\dot{i}_{max_L} < 0 \tag{3.20}$$

and

$$\frac{V_{smax_L}(V_{min_L} - V_{max_H}) - V_{smax_L}^2}{L_L} - V_{ref}\dot{i}_{max_L} > 0. \tag{3.21}$$

Note that it is reasonable to have inequalities (3.20) and (3.21) since $L_L \ll C_{s_L} \ll i_{smax_L} < V_{smin_L} < V_{ref} \ll \dot{i}_{max_L}$ and $L_L \ll V_{max_H} \ll V_{smax_L} < V_{min_L} < V_{ref} \ll \dot{i}_{max_L}$.

Then the existing condition for this SMC is

$$\begin{cases} \lim_{S_L(x)\to S_L(x_0)^+} \dot{S}_L(x) < 0, \\ \lim_{S_L(x)\to S_L(x_0)^-} \dot{S}_L(x) > 0, \end{cases} \quad \text{for all } x_0 \in \Gamma_L. \tag{3.22}$$

From (3.10), we have

$$i_{lf} = \frac{V_{ref} - V_{lf} + k_1 \int_0^t (V_{ref} - V_{lf})d\tau + k_2 V_{s_L} i_{s_L}}{k_2 V_{ref}}, \tag{3.23}$$

based on which the inequalities (3.15) and (3.17) can be written as

$$\begin{aligned} \dot{S}_L = &- \frac{V_{ref} - V_{lf} + k_1 \int_0^t (V_{ref} - V_{lf})d\tau + k_2 V_{s_L} i_{s_L}}{C k_2 V_{ref}} \\ &+ \frac{q_H i_{s_{H_L}}}{C} + k_1(V_{ref} - V_{lf}) \\ &+ k_2(-\frac{V_{s_L}^2}{L_L} + \frac{i_{s_L}^2}{C_{s_L}} - V_{ref}\dot{i}_{lf}) < 0, \end{aligned} \tag{3.24}$$

and

$$\begin{aligned} \dot{S}_L = &- \frac{V_{ref} - V_{lf} + k_1 \int_0^t (V_{ref} - V_{lf})d\tau + k_2 V_{s_L} i_{s_L}}{C k_2 V_{ref}} \\ &+ \frac{q_H i_{s_{H_L}}}{C} + \frac{i_{s_{L_L}}}{C} + k_1(V_{ref} - V_{lf}) \\ &+ k_2(\frac{(V_{lf} + V_{hf})V_{s_L} - V_{s_L}^2}{L_L} + \frac{i_{s_L}^2}{C_{s_L}} - V_{ref}\dot{i}_{lf}) > 0. \end{aligned} \tag{3.25}$$

Since $Ck_2V_{ref} > 0$, (3.24) and (3.25) can be written as

$$\begin{aligned} &- k_1 \int_0^t (V_{ref} - V_{lf})d\tau - k_2(V_{s_L} i_{s_L} - q_H i_{s_{H_L}} V_{ref}) \\ &+ k_1 k_2 (CV_{ref}^2 - CV_{ref}V_{lf}) \\ &+ k_2^2(\frac{-CV_{ref}V_{s_L}^2}{L_L} + \frac{CV_{ref}i_{s_L}^2}{C_{s_L}} - CV_{ref}^2\dot{i}_{lf}) < V_{ref} - V_{lf}, \end{aligned} \tag{3.26}$$

and

$$
\begin{aligned}
&- k_1 \int_0^t (V_{ref} - V_{lf}) d\tau + k_2 (i_{s_{L_L}} V_{ref} - i_{s_L} V_{s_L} + q_H i_{s_{H_L}} V_{ref}) \\
&+ k_2^2 (\frac{C V_{ref} V_{s_L} (V_{lf} + V_{hf} - V_{s_L})}{L_L} + \frac{C V_{ref} i_{s_L}^2}{C_{s_L}} - C V_{ref}^2 \dot{i}_{lf}) \\
&+ k_1 k_2 (C V_{ref}^2 - C V_{ref} V_{lf}) > V_{ref} - V_{lf}.
\end{aligned} \tag{3.27}
$$

The parameters k_1 and k_2 should be chosen to fulfill the inequalities (3.15), (3.17), (3.26), and (3.27) to satisfy both the hitting condition and existing condition, which are the sufficient conditions to attain the successful control. The details about the selection of k_1 and k_2 will be discussed in Section 3.2.3.

Charge Control of the LF-VIC

In the application of grid connected DFIG system, a charge control scheme is developed to regulate the LF-VIC's state of charge (V_{s_L}) by coupling a PI controller with the controller of grid side converter. Since the charge controller is required to operate more slowly than the voltage controller, the average of V_{s_L} (i.e., $V_{s_{Lavg}}$) is controlled, which is acquired by passing V_{s_L} through a low pass filter with the corner frequency f_c (see Fig. 3.4). In the voltage control of DC-link capacitor, the voltage V is fed back to the controller of grid side converter. Herein, the voltage V^* rather than V is injected. V^* is the estimated value of V obtained from the LF-VIC's state of charge through a PI controller:

$$
V^* = V_{ref} - k_P (V_{sref_L} - V_{s_{Lavg}}) - k_I \int_0^t (V_{sref_L} - V_{s_{Lavg}}) d\tau.
$$

In this way, the control scheme of the grid side converter is not violated, realising a 'plug-and-play' pattern for the PVIC.

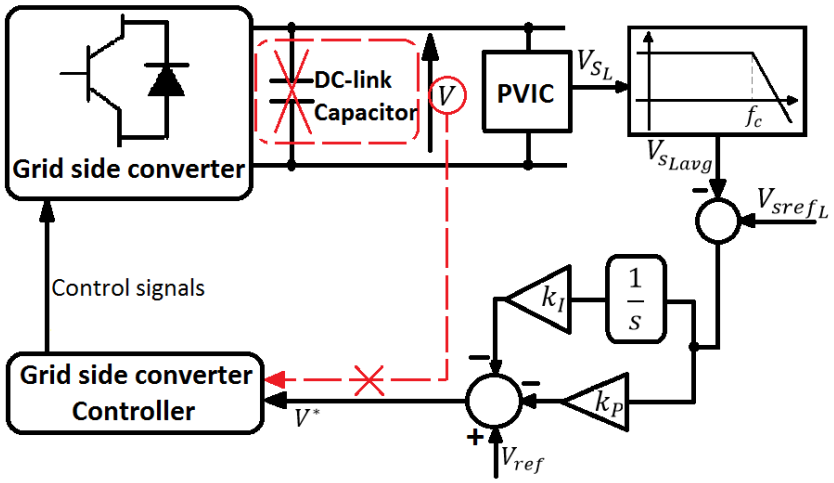

Figure 3.4: Charge control scheme of the LF-VIC. The estimated voltage V^* replaces the measurement of the DC-link voltage for the grid side converter.

3.2.2 Control of the HF-VIC

For the control of HF-VIC, both voltage control and charge control are implemented by a SMC whose sliding function is

$$\begin{aligned} S_H(x) = (0 - V_{hf}) - k_3(V_{ref} i_{hf} - V_{s_H} i_{s_H}) \\ + k_4(V_{sref_H} - V_{s_{Havg}}). \end{aligned} \tag{3.28}$$

The sliding surface Γ_H is the set of all the possible $x = \begin{bmatrix} V_{hf} & i_{s_H} & V_{s_H} \end{bmatrix}^T \in \Omega$ for which

$$S_H(x) = 0. \tag{3.29}$$

The expression $V_{ref} i_{hf} - V_{s_H} i_{s_H}$ appearing in (3.28) represents the power stored in L_H, which is included in the HF-VIC controller. $V_{sref_H} - V_{s_{Havg}}$ is the charge control term in this sliding function. As with the charge control of the LF-VIC, the average of V_{s_H} (i.e., $V_{s_{Havg}}$) is regulated to realise a much slower response of the charge control than the voltage control. $V_{s_{Havg}}$ is obtained by passing V_{s_H} through a low pass filter with the corner frequency f_c. The absolute values of the parameters k_3 and k_4 should be very small to guarantee the accuracy of the control.

The hysteresis-modulation (HM) sliding mode control is also applied to the HF-

VIC, using the same ϵ as in (3.11):

$$\begin{cases} q_H = \begin{cases} 1, \text{if } S_H < -\epsilon, \\ 0, \text{if } S_H > \epsilon, \\ \text{previous state, if } S_H \in [-\epsilon, \epsilon]; \end{cases} \\ \tilde{q}_H = 1 - q_H. \end{cases}$$

The hitting condition is described as

$$S_H(x) \cdot \dot{S}_H(x) < 0$$

for all $x \in \Omega \backslash \Gamma_H$. Here $\dot{V}_{s_{Havg}}$ is limited as $\dot{V}_{s_{Havg}} \in [-\dot{V}_{s_{Havg_{max}}}, \dot{V}_{s_{Havg_{max}}}]$, where $\dot{V}_{s_{Havg_{max}}}$ should be small due to the slow change of $V_{s_{Havg}}$. Similarly as in Section 3.2.1, when $S_H(x) > 0$ and $S_H(x) < 0$, we have

$$\dot{S}_H(x) = \frac{-i_{hf} - q_L i_{s_{L_H}}}{C} - k_3 \left(V_{ref} \dot{i}_{hf} - \frac{i_{s_H}^2}{C_{s_H}} + \frac{V_{s_H}^2}{L_H} \right) - k_4 \dot{V}_{s_{Havg}} < 0 \tag{3.30}$$

and

$$\begin{aligned} \dot{S}_H(x) = & \frac{-i_{hf} - i_{s_{H_H}} - q_L i_{s_{L_H}}}{C} \\ & -k_3 \left(-\frac{V_{s_H}(V_{hf} + V_{lf})}{L_H} + \frac{V_{s_H}^2}{L_H} + V_{ref} \dot{i}_{hf} - \frac{i_{s_H}^2}{C_{s_H}} \right) - k_4 \dot{V}_{s_{Havg}} > 0, \end{aligned} \tag{3.31}$$

respectively. Here, $\dot{i}_{hf}$ is limited as $\dot{i}_{hf} \in [-\dot{i}_{max_H}, \dot{i}_{max_H}]$, that is, the sufficient conditions for (3.30) and (3.31) are

$$\begin{aligned} \dot{S}_{Lmax} \leq & k_3 \left(\frac{i_{smax_H}^2}{C_{s_H}} + V_{ref} \dot{i}_{max_H} - \frac{V_{smin_H}^2}{L_H} \right) \\ & + k_4 \dot{V}_{s_{Havg_{max}}} + \frac{i_{max_H} + i_{smax_{LH}}}{C} < 0, \end{aligned} \tag{3.32}$$

and

$$\begin{aligned} \dot{S}_{Lmin} \geq & -k_3 \left(\frac{V_{smax_H}(V_{max_H} - V_{min_L}) + V_{smax_H}^2}{L_H} + V_{ref} \dot{i}_{max_H} \right) \\ & - k_4 \dot{V}_{s_{Havg_{max}}} - \frac{i_{max_H} + i_{smax_{HH}} + i_{smax_{LH}}}{C} > 0. \end{aligned} \tag{3.33}$$

To fulfil (3.32) and (3.33), we set

$$\begin{cases} k_3 > 0, & k_4 < 0, \\ 0 < \dot{i}_{max_H} < \min F_{Hb}, \\ F_{Hb} = \{\frac{V_{smin_H}^2}{L_H V_{ref}} - \frac{i_{smax_H}^2}{C_{s_H} V_{ref}}, -\frac{V_{smax_H}(V_{max_H} - V_{min_L}) + V_{smax_H}^2}{L_H V_{ref}}\}, \end{cases} \tag{3.34}$$

where F_{Hb} is derived from

$$\frac{i_{smax_H}^2}{C_{s_H}} + V_{ref}\dot{i}_{max_H} - \frac{V_{smin_H}^2}{L_H} < 0 \tag{3.35}$$

and

$$\frac{V_{smax_H}(V_{max_H} - V_{min_L}) + V_{smax_H}^2}{L_H} + V_{ref}\dot{i}_{max_H} < 0. \tag{3.36}$$

To fulfil the inequalities (3.35) and (3.36), we set $L_H \ll C_{s_H} \ll i_{smax_H} < V_{smin_H} < V_{ref} \ll \dot{i}_{max_H}$ and $L_H \ll V_{max_H} \ll V_{smax_H} < V_{min_L} < V_{ref} \ll \dot{i}_{max_H}$. The existing condition for this SMC is

$$\begin{cases} \lim_{S_H(x) \to S_H(x_0)^+} \dot{S}_H(x) < 0, \\ \lim_{S_H(x) \to S_H(x_0)^-} \dot{S}_H(x) > 0, \end{cases} \quad \text{for all } x_0 \in \Gamma_H. \tag{3.37}$$

Similarly as in Section 3.2.1, we get

$$\begin{aligned} &- k_3(V_{s_H} i_{s_H} + q_L V_{ref} i_{s_{L_H}}) - k_4(V_{s_{ref_H}} - V_{s_{Havg}}) \\ &- k_3 k_4 C V_{ref} \dot{V}_{s_{Havg}} + k_3^2 C V_{ref}(V_{ref}\dot{i}_{hf} + \frac{i_{s_H}^2}{C_{s_H}} - \frac{V_{s_H}^2}{L_H}) < -V_{hf}, \end{aligned} \tag{3.38}$$

and

$$\begin{aligned} &k_3(i_{s_{H_H}} V_{ref} - q_L i_{s_{L_H}} V_{ref} - V_{s_H} i_{s_H}) \\ &+ k_3^2 C V_{ref}(V_{ref}\dot{i}_{hf} + \frac{i_{s_H}^2}{C_{s_H}} + \frac{(V_{hf} + V_{lf} - V_{s_H}) V_{s_H}}{L_H}) \\ &- k_4(V_{sref_H} - V_{s_{Havg}}) - k_3 k_4 C V_{ref} \dot{V}_{s_{Havg}} > -V_{hf}. \end{aligned} \tag{3.39}$$

The parameters k_3 and k_4 should be chosen to satisfy the inequalities (3.30), (3.31), (3.38) and (3.39), so that the state trajectory will converge and stabilise at the sliding surface Γ_H. The details about the selection of k_3 and k_4 will be discussed in Section 3.2.3.

3.2.3 Parameter selection

In order to limit the deviation between V and its reference V_{ref}, the absolute values of the parameters k_1, k_2, k_3 and k_4 should be small. We apply the interior-point optimization algorithm to find the boundaries of these four parameters, which are embedded in the nonlinear programming solver '*fmincon*' in Matlab (MathWorks).

The optimization for LF-VIC controller parameters is conducted to minimize $|k_1| + |k_2|$ under the inequality constraints (3.7), (3.8), (3.15), (3.17), (3.19), (3.26), (3.27), and equality constraint (3.10). Similarly, the objective function for parameter optimization of the HF-VIC controller is $|k_3|+|k_4|$, with the inequalities constraints (3.7), (3.8), (3.30), (3.31), (3.34), (3.38), (3.39), and equality constraint (3.29). The results of these optimizations provide the boundaries for k_1, k_2, k_3 and k_4 to ensure the successful control of both LF-VIC controller and HF-VIC controller.

The parameters' initial values are all set to be zero. The related operating boundaries are listed in Table 3.1. The optimal boundaries for the parameters $k_1 \sim k_4$ are

$$\begin{cases} k_{1min} = 2.66 \times 10^{-7}, \\ k_{2min} = 5.77 \times 10^{-6}, \\ k_{3min} = 2.55 \times 10^{-7}, \\ k_{4max} = -1.01 \times 10^{-4}. \end{cases}$$

Table 3.1: Operating boundaries

Parameters	**Values**	**Parameters**	**Values**
V_{smax_L}	920 V	V_{smax_H}	920 V
i_{smax_L}	50 A	i_{smax_H}	200 A
$i_{smax_{HL}}$	50 A	$i_{smax_{LH}}$	200 A
$i_{smax_{LL}}$	50 A	$i_{smax_{HH}}$	200 A
i_{max_L}	100 A	i_{max_H}	500 A
V_{min_L}	1140 V	$\dot{V}_{s_{Havg_{max}}}$	100 V/s
V_{max_H}	10 V	$V_{s_{Havg_{max}}}$	770 V
V_{max_L}	1160 V	$\dot{i}_{max_L}$	2.76×10^6 A/s
$V_{s_{Havg_{min}}}$	570 V	$\dot{i}_{max_H}$	2.75×10^6 A/s

.

3.3 Simulation studies

The simulations are conducted using a grid-connected DFIG model [96, 97] driven by the WP 1.5-MW wind turbine model [129, 72, 91]. The parameters of the DFIG are listed in Table 3.2. The hub height of wind turbine is 84 m. The rated wind speed is about 12 m/s. The blade length is 33.25 m and the maximum blade chord is 8% of blade radius [120]. Note that the grid frequency in the simulations is set to be 60 Hz due to the default setting of the WP wind turbine model.

Table 3.2: Parameters of the 1.5-MW doubly fed induction generator (DFIG) model (in p.u. units) [96, 97].

DFIG Parameters	**Values**
Frequency	60 Hz
Pole pairs	3
Magnetizing inductance	2.9 p.u.
Stator resistance	0.023 p.u.
Stator inductance	0.18 p.u.
Rotor type	Wound
Rotor resistance	0.016 p.u.
Rotor inductance	0.16 p.u.
Inertia	0.685 p.u.

The NREL FAST (Fatigue, Aerodynamics, Structures, and Turbulence) code [72] is used to simulate dynamic responses of the turbine. FAST takes aerodynamics, control and electrical (servo) dynamics, and structural (elastic) dynamics of the turbine into account. FAST is interfaced with Matlab/Simulink through a Simulink S-Function block. During simulations, this block calls the FAST Dynamic Library, which has integrated all the FAST modules [72] and is compiled as a dynamic-link-library (DLL).

NREL TurbSim [70] is utilised to generate stochastic, full-field, and turbulent wind flows for simulation studies. The International Electro-technical Commission (IEC) Kaimal spectral model [24, 25] in Turbsim is applied to generate the wind condition as shown in Fig. 3.5(a), with the category A (most turbulent) IEC NTM (normal turbulence model). The mean hub-height longitudinal wind speed is 12 m/s. Note that the average sampling frequency of the LF-VIC controller is smaller than that of HF-VIC controller in the simulations, which are approximately 45 kHz and 100 kHz, respectively.

The voltage filtering performances of two configurations are compared: a 15 mF DC-link capacitor and a PVIC as in Fig. 3.3, where the total capacitance of C, C_{s_L} and C_{s_H} is 15 mF. Tables 3.3 and 3.4 list the parameters of the electronic components in

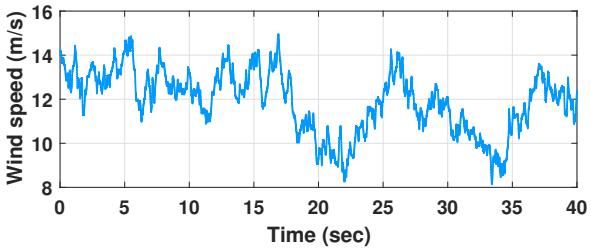

(**a**) The turbulent wind input.

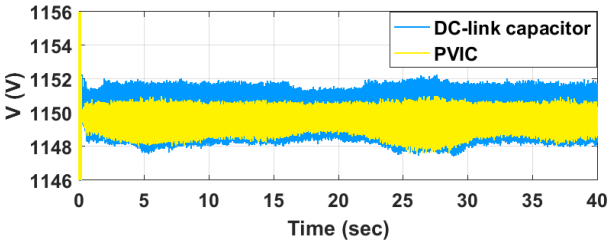

(**b**) DC-link voltage V stabilised by DC-link capacitor and PVIC.

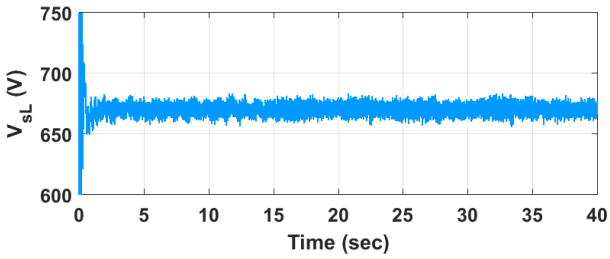

(**c**) State of charge of the LF-VIC (i.e., V_{s_L}).

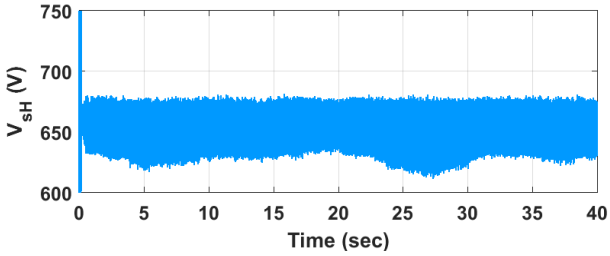

(**d**) State of charge of the HF-VIC (i.e., V_{s_H}).

Figure 3.5: Wind input and performances of PVIC under normal grid operation.

PVIC and control parameters of PVIC, respectively.

Firstly the simulation is conducted without grid disturbance under the turbulent wind input (see Fig. 3.5). Fig. 3.5(a) and Fig. 3.5(b) demonstrate the turbulent wind

Table 3.3: Parameters of the electronic components in PVIC (see Fig. 3.3).

Components in PVIC	**Configuration**
C	7 mF
C_{s_L}	6 mF
C_{s_H}	2 mF
C_{sn}	1 nF
L_L	10 µH
L_H	10 µH

Table 3.4: Control parameters of the PVIC.

Parameters	**Values**	**Parameters**	**Values**
V_{ref}	1150 V	ϵ	0.5
V_{sref_L}	670.5 V	V_{sref_H}	670.5 V
k_1	5×10^{-5}	k_2	6×10^{-6}
k_3	2.5×10^{-5}	k_4	-2.5×10^{-2}
D_{pow_up}	0.3	f_{pow_up}	30 kHz
k_P	0.0169	k_I	0.0225
f_l	120 Hz	f_c	60 Hz

input and the DC-link voltage stabilised by DC-link capacitor and PVIC. Fig. 3.5(c) and Fig. 3.5(d) illustrate the SoC of PVIC (i.e., V_{s_L} and V_{s_H}). It is clear that when there is no grid disturbance, both configurations can stabilise the DC-link voltage V to its reference, and PVIC reduces about 30% of the voltage fluctuations compared with the equivalent DC-link capacitor (see Fig. 3.5(b)), which is mainly achieved by HF-VIC controller to suppress the high-frequency ripple due to the fast switching of two converters. The SoC of the LF-VIC and HF-VIC are successfully controlled to the vicinity of their references by the charge control schemes explained in Section 3.2.

Then the simulations are conducted under four types of grid disturbances with the same turbulent wind input (Fig. 3.5(a)). The first case is the frequency variation. In reality, the frequency, as a key factor to judge the power quality, is allowed to vary within a very narrow range during normal operation. Here, we test the performance of the PVIC and a DC-link capacitor under a one-second large sinusoidal grid frequency variation with an amplitude of 1 Hz and a period of 0.5 s. Fig. 3.6(a) and Fig. 3.6(c) show this grid condition and the performances of PVIC and DC-link capacitor. Note that the V_{lf} and V_{hf} of the DC-link voltage are obtained according to (3.1).

The second type of the tested grid disturbances is the balanced three-phase voltage sag and swell. This is one of the most common power disturbances, which is usually

caused by abrupt reduction or increase in loads. The grid voltage is altered four times by ±0.15 p.u. and each change is kept for 15 grid cycles (250 ms) (see Fig. 3.6(b) and Fig. 3.6(d)). Note that the amplitude of grid voltage (phase-to-phase) is 120 kV (see Fig. 3.1).

The third case of the disturbance test is the grid frequency harmonics. In reality, a small range of frequency harmonics due to the nonlinear loads, transformer magnetisation nonlinearities, rectification, etc. is allowed in the power system, which may introduce the high-frequency ripple to DC-link voltage. We inject a combination of a negative-sequence 1st order frequency harmonic (with the magnitude of 0.1 p.u.) and negative-sequence 3rd order frequency harmonic (with the magnitude of 0.1 p.u. and phase shift of 35°), lasting for 1 s. Fig. 3.7(a) and Fig. 3.7(c) show this grid condition and the voltage filtering performance.

Finally we combine the above frequency variation and frequency harmonic disturbances as the fourth case. That is, both high-frequency and low-frequency ripples are introduced to the DC-link voltage. The grid condition and the voltage filtering performance are shown in Fig. 3.7(b) and Fig. 3.7(d).

In Table 3.5, we summarise the ripple suppression performance of the PVIC and DC-link capacitor with the same total capacitance under different grid conditions in Fig. 3.6 and Fig. 3.7. Note that when no grid disturbance occurs, there is no low frequency variations, thence no information about V_{lf} (peak-peak) is provided in Table 3.5. It is clear that the PVIC reduces the total voltage variation by approximately 85% in comparison with the equivalent DC-link capacitor during these grid disturbances. This is because the oscillations in the DC-link voltage are transferred into the capacitors C_{s_L} and C_{s_H} of the PVIC. The same conclusion can be obtained under other grid conditions, such as unbalanced voltage sag and swell, the phase shift in voltage, different frequency harmonic injections, frequency steps variations, or the combinations of some of these faults.

Table 3.5: Performance comparisons between the DC-link capacitor and PVIC.

Grid disturbance	V (peak-peak) [V]			V_{lf} (peak-peak) [V]			V_{hf} (peak-peak) [V]		
	DC-link Capacitor	PVIC	Comparison (%)	DC-link Capacitor	PVIC	Comparison (%)	DC-link Capacitor	PVIC	Comparison (%)
No grid disturbance	4.5	3	−33	–	–	–	–	–	–
Frequency variation	25	3.5	−86	8.5	0.4	−95	10	3.3	−67
Voltage sag and swell	38.5	6	−84	33	2	−94	12.5	4.5	−64
Frequency harmonics in negative sequence	51.5	6	−88	40	3	−92.5	23	6	−74
Frequency variation and frequency harmonics in negative sequence	48	6	−87.5	43	3	−93	21	5.5	−74

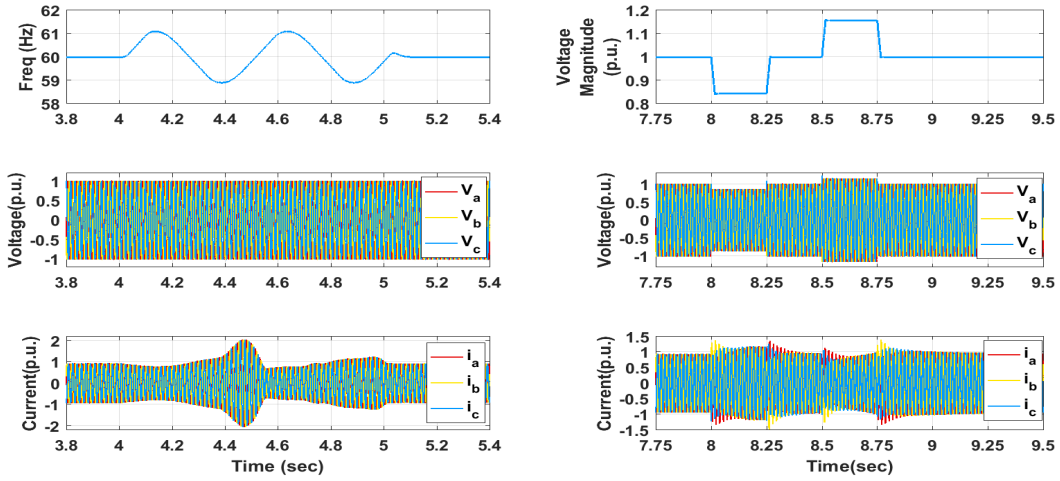

(**a**) (**b**)

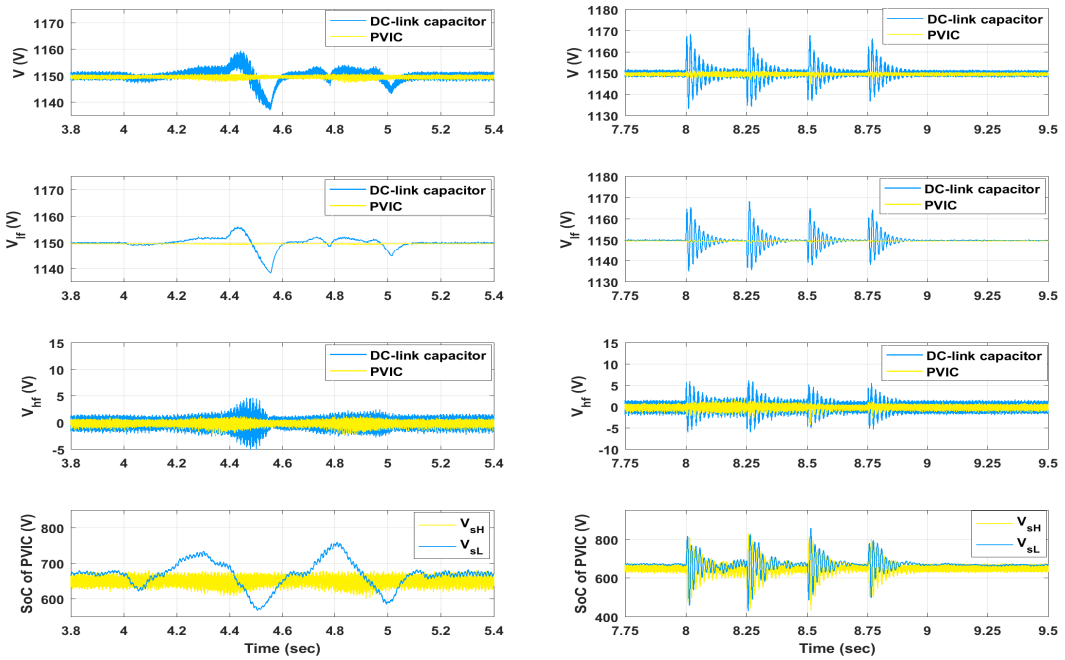

(**c**) (**d**)

Figure 3.6: (**a**) shows frequency variation and three-phase grid voltage and current; (**b**) describes the grid voltage magnitude variation and three-phase grid voltage and current; (**c**) illustrates voltage filtering performance (V, V_{lf}, V_{hf}) of DC-link capacitor and PVIC, and PVIC's state of charge (V_{s_L}, V_{s_H}) under the grid conditions of (**a**); (**d**) exhibits the voltage filtering performance (V, V_{lf}, V_{hf}) of DC-link capacitor and PVIC, and PVIC's state of charge (V_{s_L}, V_{s_H}) under the grid conditions of (**b**).

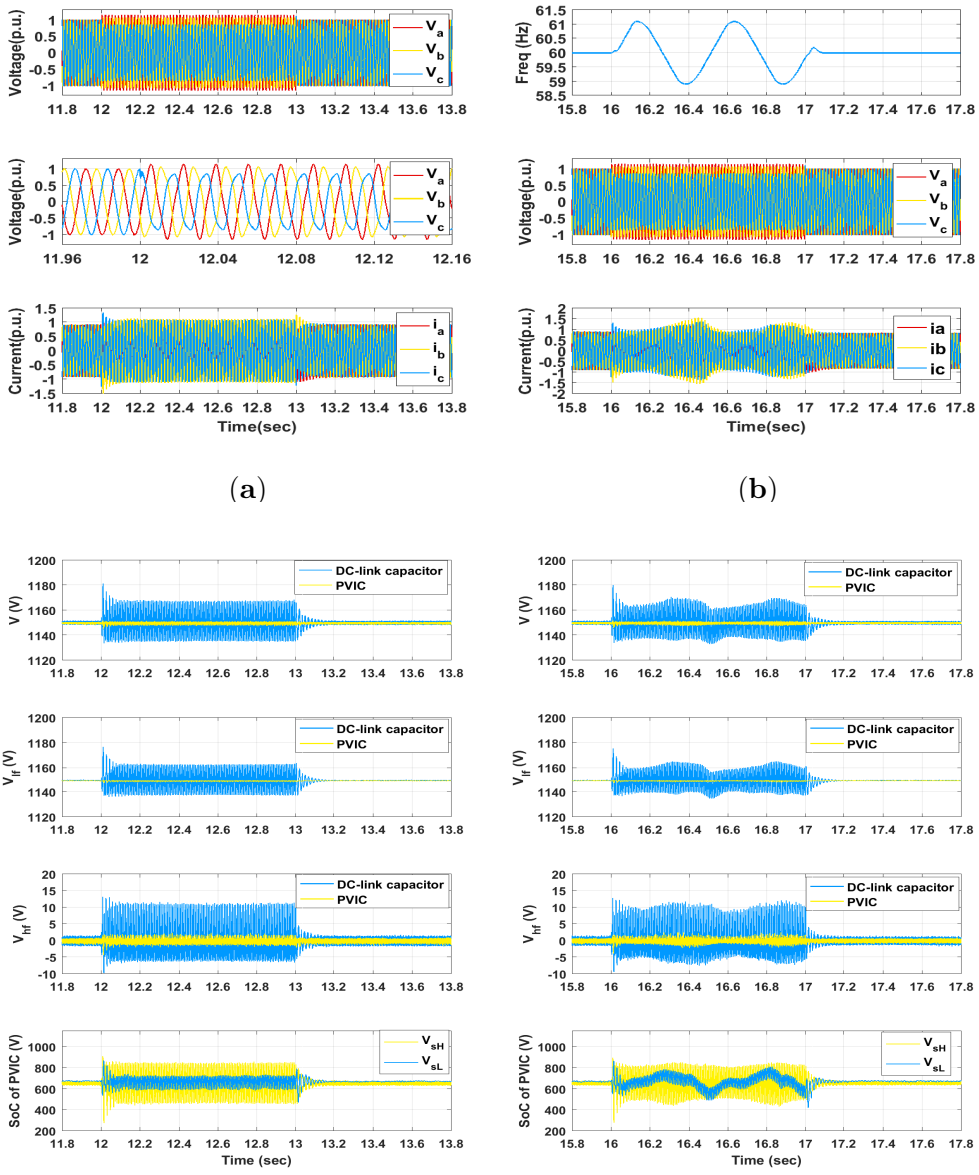

Figure 3.7: (**a**) shows the three-phase grid voltage and current when there is negative sequence 1st order frequency harmonic (with magnitude of 0.1 p.u.) and negative sequence 3rd order frequency harmonic (with magnitude of 0.1 p.u. and phase shift of 35°) injected; (**b**) demonstrates the frequency variation, three-phase grid voltage and current when the situations in Fig. 3.6(a) and (**a**) both occur; (**c**) describes voltage filtering performance (V, V_{lf}, V_{hf}) of DC-link capacitor and PVIC, and PVIC's state of charge (V_{s_L}, V_{s_H}) under the grid conditions of (**a**); (**d**) displays voltage filtering performance (V, V_{lf}, V_{hf}) of the DC-link capacitor and PVIC, and PVIC's state of charge (V_{s_L}, V_{s_H}) of under the grid conditions of (**b**).

3.4 Conclusions

We have introduced the concept of parallel virtual infinite capacitor (PVIC), which referred to a low-frequency (LF) virtual infinite capacitor (VIC) and a high-frequency (HF) VIC working on a common DC link and sharing one capacitor. It could suppress voltage ripple in a wider frequency band than what one VIC could achieve. The low frequency ripple was regulated by a sliding mode controller (SMC), and a PI controller was applied to maintain the LF-VIC within its operating range. Another SMC was applied to suppress high-frequency fluctuations while at the same time keeping the HF-VIC's state of charge within the normal range. The PVIC has been applied to replace the DC-link capacitor between two back-to-back converters in a grid-connected DFIG-based wind turbine system. The simulations were conducted under different grid conditions with turbulent wind input. The results indicated that the PVIC provided outstanding ripple suppression performance regardless of the low-frequency and high-frequency fluctuations, individually or together. In comparison with an equivalent DC-link capacitor, the PVIC reduced the DC-link voltage ripple by about 30% during normal grid operation, and by approximately 85% during the tested grid disturbances, which implies that PVIC is a better replacement for the conventional DC-link capacitor.

Chapter 4

Feasibility Studies of a Converter-free Grid-connected Hydrostatic Wind Turbine

In Chapter 3, the PVIC removes the bulky, vulnerable and expensive DC-link capacitor between two power converters in wind turbine grid integration system. However, the power converters are also fragile and expensive. Besides, the power converters decouple the doubly fed induction generator (DFIG) and the grid, so that the DFIG in wind power plant can neither provide the direct inertia support nor participate in the grid frequency regulations. Due to the increasing penetration of wind power generation, it imposes great challenges to the frequency regulation in the modern power system.

Hence, in this chapter, we look into the hydrostatic wind turbine (HWT) which completely remove the power converters and DC-link capacitor in the grid integration. We investigate the feasibility of frequency regulation by a HWT. By controlling the energy extraction and energy storage of the HWT, the 'continuously variable gearbox ratio' can be realised to maintain the constant generator speed, which mimics the frequency regulation process of a conventional thermal plant. It is connected to a synchronous generator (SG) and then directly to the grid, without power converters in-between. To test the performances of the control scheme, the HWT is connected to a 5-bus grid model and operates with different frequency events under turbulent wind. The simulation results indicate that the HWT provides a promising solution for modern power system frequency regulation. These results are drafted into a paper [87].

4.1 Introduction

With the growing demands for the low-carbon emission around the world, the engineers are strongly encouraged to utilise the alternatives to fossil fuels in industrial applications, and the researchers pay more and more attentions to the development of the renewable energies, such as wind energy. The wind energy is deemed as one of the most important green energies over the world and has been widely applied in power generations. By the end of 2017, the cumulative installed wind turbine capacity was over 539 GW, and it is anticipated to be 840 GW in 2020 [46, 158]. In some EU countries such as Denmark, Portugal, Ireland and Germany, the wind power penetration rate reached over 20% in 2017 [46]. Compared with the conventional thermal power plants, it is more difficult for wind farm to provide the frequency regulation, because of the uncontrollable nature of wind. Once the power supply cannot balance the load demand, the frequency will vary at a rate related to the system inertia. However, due to the existence of power converters, the generator speed is decoupled from the system frequency in wind farms, which cannot provide direct inertia response to the grid. Hence, the growth in wind power penetration leads to the reduction in system inertia, thus bringing great challenges and concerns for system stability. In some countries such as UK and Denmark, the frequency support by the wind power has already been required in the grid codes [32, 92]. Many research works have been oriented to investigate the frequency control by wind turbines, aiming to take over part of the responsibilities in frequency regulation in the future. The general frequency regulation for wind farms includes the inertia support [154, 99], primary frequency control [15] and the secondary automatic generation control (AGC) [22], just as what thermal power plants do. The doubly fed induction generators (DFIGs) are commonly applied in wind industries. Some researches propose the concept of emulated inertia response, which is to release the kinematic energy stored in DFIG rotor for the grid when system frequency drops [44, 35]. However, compared to the inertia response by the conventional synchronous generator, the indirect inertia support requires more complicated control schemes. Moreover, using wind turbines for frequency regulation usually forces wind turbine to operate at a de-rating situation, in order to reserves abundant power to manage the frequency variations [5, 15, 153]. It is usually achieved by redesigning the power control loop in rotor-side converter and deviating the blade pitch angles from the optimal position to 'de-rate' the power extraction [22, 155]. However, the de-rating operation violates the maximum power point tracking (MPPT) rules, which leads to the concern of energy waste and the economically trade-offs between the revenues from energy and regulation markets. Moreover, the accuracy

of the regulation is influenced by the pitch response time, the turbulent wind and the amount of reserved wind power, thus resulting in low efficiency and poor reliability [80]. In a word, though the frequency regulation by wind power system is of highly necessity for modern power market, the existing methods still suffers from complicated algorithms, energy waste, and accuracy concerns.

The energy storage system (ESS) acts as an alternative to support frequency regulations for wind turbines. There are various types of energy storage technologies, such as battery energy storage (BESS), pump hydro energy storage (PHES), pneumatic energy storage (PES), etc. BESS is a popular technology due to its fast response and accurate regulation [135, 95]. However, high cost, high flammability, and vulnerable power electronics devices become the main obstacles for its widespread use [50]. PHES is to pump or release water between lower and higher reservoirs, which is a readily available mature technique in industries. However, the slow response and geographical requirements limit its extensive application [65, 166]. As for PES, the compressed air energy storage (CAES) technology can be applied on very large scales, which regulates the energy by pressurising or de-pressurising the air in a sealed underground cavern. But it requires extra aboveground devices and it is highly geological structure reliance [50]. Another commonly applied PES technology is the compressed gas hydraulic accumulator. It removes the geological dependency. However, for DFIG wind trubine, extra devices and energy transition during operation may result in low energy efficiency [50]. That is, there is some disadvantages for the energy storage system assembling to the wind power system, which impedes its widespread applications.

Hydrostatic wind turbine (HWT) may offer a better solution. In HWT, the original gearbox drivetrain between the wind turbine rotor shaft and generator rotor shaft is replaced by the hydrostatic transmission (HST) which is equipped with a hydraulic accumulator (see Fig. 4.1). It enables the continuously variable transmission ratio, so that the HWT is connected to a synchronous generator (SG) rather than the commonly applied DFIG, thus achieving the converter-free connection, like a conventional thermal plant. The SG is able to directly provide inertia support to the grid. With proper control, the HWT can also provide the primary and secondary frequency regulation to the grid, with easily-assembled energy storage devices to reserve the power. Furthermore, HST introduces a new design dimension which offers a more reliable transmission system in HWT by removing fragile gearbox with the reduced nacelle weight [42, 105]. As a matter of fact, the uncontrollable characteristic of the wind brings huge burdens to the wind turbine gearbox drivetrain under wind gusts, which is considered as one of the major causes to the premature failure of the wind turbine [42, 128, 105]. Particularly in

the offshore case, the faster offshore wind speed and severe weather conditions increase the risk of gearbox failure. Thus the introduction of the HST includes the removal of the power converters and the gearbox, which can cut down the maintenance cost for wind power integration, especially in offshore case. In addition, the damping effect is inherently provided by the fluid in the HST which reduces the stress to the generator [42].

In the present chapter, we focus on the offshore HWT. It is composed of a closed-loop oil circuit (connecting a pump and a motor), and an open-loop sea water circuit (connecting a pump-motor, a hydraulic accumulator, and a relief valve) (see Fig. 4.1). The current researches on HWTs mainly focus on the modelling and power extraction [144, 77, 38]. In the present chapter, we investigate the feasibility to provide frequency support by the HWT through the coordinated control strategy on energy extraction and energy storage, aiming to deliver the required amount of power to the grid system in all wind conditions. We integrate the HWT model with a 5-bus grid model and the simulation results indicate that the proposed control scheme provides excellent frequency regulation performance.

This chapter is structured as follows: in Section 4.2, we introduce the system structures with its mathematical models. In Section 4.3, we expatiate the coordinated control scheme. In Section 4.4, we conduct the simulations. Finally, Section 4.5 concludes this chapter.

4.2 System modelling

Previous research [144] has transformed the gearbox in NREL 5-MW monopile wind turbine model within FAST code [72, 129, 71] into the rigid connection between wind turbine rotor and pump. The mathematical models of the hydrostatic transmission system (Fig. 4.1) is introduced in this section following [144, 77, 38].

4.2.1 Variable displacement pump

The wind turbine rotor transforms the wind energy into the rotary motion then the variable displacement pump converts the mechanical power of rotor shaft to the hydraulic power in the high pressure oil line [77]. The model of the pump is defined by the net generated volumetric flow rate Q_{pump} and the transmitted torque τ_{pump}:

$$Q_{pump} = D_p \omega_r - C_{sp} p_{pump}, \tag{4.1}$$

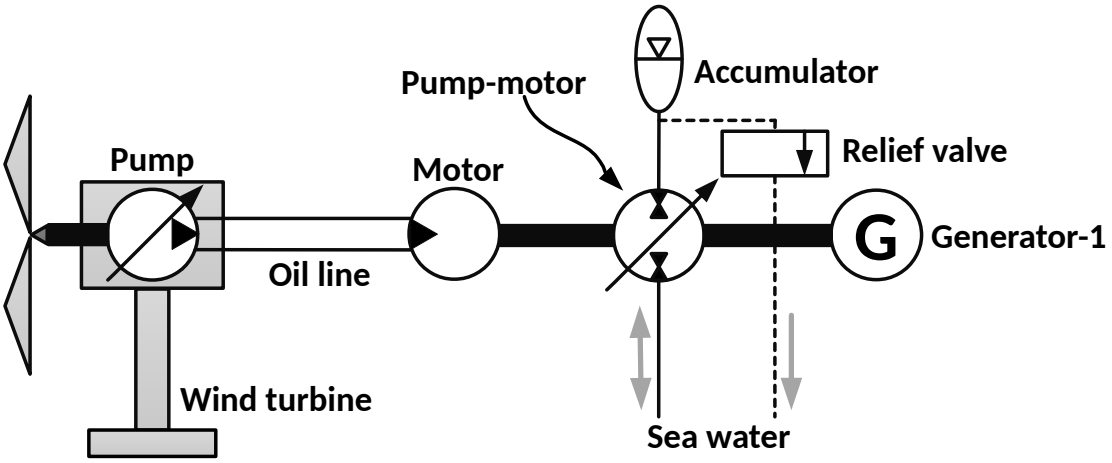

Figure 4.1: Structure diagram of a 5-MW hydrostatic wind turbine.

$$\tau_{pump} = (1 + C_{fp})D_p p_{pump} + B_p \omega_r, \tag{4.2}$$

where D_p, ω_r, C_{sp}, p_{pump}, C_{fp} and B_p represent the pump volumetric displacement, wind turbine rotor speed, laminar leakage coefficient, the pressure difference across the pump, the Coulomb friction coefficient and the viscous damping coefficient of pump respectively.

The dynamics of the pump actuator is modelled as

$$\dot{D}_p = \frac{1}{T_p} \cdot (D_p^* - D_p), \tag{4.3}$$

where D_p^* represents the command of the pump volumetric displacement and T_p represents the time constant.

4.2.2 Fixed displacement motor

The fixed displacement motor transforms the hydraulic power from the high pressure oil line to the kinematic energy of the generator rotor shaft, whose model is similar to the pump with only difference being the energy conversion direction. The net volumetric flow rate Q_{motor} and transmitted torque of the motor τ_{motor} are described as

$$Q_{motor} = D_m \omega_g + C_{sm} p_{motor}, \tag{4.4}$$

$$\tau_{motor} = (1 + C_{fm})D_m p_{motor} - B_m \omega_g, \tag{4.5}$$

where D_m, ω_g, C_{sm}, p_{motor}, C_{fm} and B_m represent the motor volumetric displacement, generator rotor speed, the laminar leakage coefficient, the pressure difference across the motor, the Coulomb friction coefficient and the viscous damping coefficient of motor respectively.

4.2.3 Oil line

The power transmission of the hydraulic pipeline is modelled by a linear state-space with assumption of constant pressure in low pressure line [77, 144]. The inputs to the pipeline are the flow rates of pump and motor. Its outputs are the pressure across the pump and motor:

$$\dot{\boldsymbol{x_l}} = \boldsymbol{A_l x_l} + \begin{bmatrix} \boldsymbol{B_{l1}} & \boldsymbol{B_{l2}} \end{bmatrix} \begin{bmatrix} Q_{pump} \\ Q_{motor} \end{bmatrix}, \tag{4.6}$$

$$\begin{bmatrix} p_{pump} \\ p_{motor} \end{bmatrix} = \begin{bmatrix} \boldsymbol{C_{l1}} \\ \boldsymbol{C_{l2}} \end{bmatrix} \boldsymbol{x_l} \tag{4.7}$$

Note that the state vector $\boldsymbol{x_l}$ in (4.6) and (4.7) does not have a physical interpretation. The frequency domain transfer functions describing the input-output behavior of a circular hydraulics line filled with viscous compressible fluid were derived in [134]. To simulate the line dynamics in time domain, the transcendental frequency domain transfer functions must be approximated by rational and proper transfer functions. To derive the approximate transfer functions describing the dynamics of the pressure and volumetric flow at the upstream and downstream side of the pipeline, the modal method is one of the best methods which is the very accurate, convenient and numerically stable. It approximates each transfer function by the sum of a finite number of first and second order modes and a constant term, with the second order modes given by couples of complex conjugated poles [64]. The impedance model of the hydraulic line is used considering the causality of the HST drivetrain system [77]. The equation (4.6) is derived based on [90] which employed the modal method to obtain the state-space representation of the impedance line model with the number of modes selected to be 10. The pressure transients along the line (using trigonometric basis functions) are approximated as [90]

$$P(x) = \sum_{j=0}^{n} p_j(t) \cos\left(\frac{j\pi x}{L}\right)$$

where x is the coordinate along the hydraulic line, n is the number of modes considered for the hydraulic line, p_j is the Ritz coefficient and L is the line length. Then they used

the Ritz method to derive p_j [90]. The state vector of the impedance line model is

$$\mathbf{x}_l = \begin{bmatrix} p_0 & r_1 & p_1 & \cdots & r_n & p_n \end{bmatrix}^T$$

where $\dot{r}_i$ $(i = 1, 2, \ldots, n)$ is the linear combination of p_i, Q_{pump} and Q_{motor}.

4.2.4 Wind turbine rotor shaft dynamics

The rotational dynamics of the wind turbine rotor shaft is modelled as:

$$\dot{\omega}_r = \frac{1}{J_r + J_p} \cdot [\tau_{aero}(\omega_r, \beta, v_{wind}) - \tau_{pump}], \tag{4.8}$$

where J_r and J_p are the rotational inertias of the wind turbine rotor and pump, and τ_{aero} is the aerodynamic torque, which depends on the rotor speed ω_r, blade pitch angle β and the rotor effective wind speed v_{wind}.

4.2.5 Variable displacement pump-motor

The fixed displacement motor and variable displacement pump-motor are both connected to the generator rotor shaft. The pump-motor keeps converting energy between kinematic and hydraulic energy, aiming to provides the desired power to the grid. The simplified model of pump-motor are expressed in the flow rate Q_{pm} and transmitted torque τ_{pm} [38]:

$$Q_{pm} = \eta_{Qpm} D_{pm} \omega_g, \tag{4.9}$$

$$\tau_{pm} = \eta_{\tau pm} D_{pm} p_{pm}, \tag{4.10}$$

where D_{pm} and p_{pm} represent the volumetric displacement of pump-motor and the pressure difference across the pump-motor, respectively. $\eta_{Qpm}, \eta_{\tau pm}$ represent the volumetric and mechanical efficiencies. Note that the sign of D_{pm} indicates the directions of the transmitted torque τ_{pm} and flow rate Q_{pm}, where positive sign implies the pump-motor is in pump motion.

The dynamics of pump-motor actuator is modelled as

$$\dot{D}_{pm} = \frac{1}{T_{pm}} \cdot (D^*_{pm} - D_{pm}), \tag{4.11}$$

where D^*_{pm} is the command of the pump-motor displacement and T_{pm} is the time constant.

4.2.6 Generator rotor shaft dynamics

The rotary motion of the generator rotor shaft is modelled as:

$$\dot{\omega}_g = \frac{1}{J_m + J_{pm} + J_g} \cdot [\tau_{motor} - (\tau_{pm} + \tau_g)]. \tag{4.12}$$

J_m, J_{pm}, J_g represents the rotational inertias of motor, pump-motor and generator. τ_g is the electrical torque of the generator.

4.2.7 Relief valve

The relief valve is installed to protect the accumulator from being overcharged. It is actually a controllable variable-area hydraulic orifice, created by a cylindrical sharp-edged spool and a variable-area slot in a sleeve. The flow rate Q_{rv} is defined as:

$$Q_{rv} = C_D A \sqrt{\frac{2}{\rho_{sw}}} \frac{p_{rv}}{\sqrt[4]{p_{rv}^2 + p_{cr}^2}}, \tag{4.13}$$

in which $p_{rv} = p_{pm}$. C_D and ρ_{sw} represent the flow discharge coefficient and the density of the seawater. p_{cr} is the minimum pressure for turbulent flow, when the block transitions from laminar to turbulent regime with $p_{cr} = \frac{\rho_{sw}}{2} \cdot (\frac{Re_{cr}\nu}{C_D \cdot 2R_{ori}})^2$. A is the cross-section area of the orifice. Re_{cr}, ν and R_{ori} are critical Reynolds number, seawater kinematic viscosity and the radius of the orifice, respectively.

4.2.8 Hydraulic accumulator

The accumulator here is a fixed volume cylindrical container, in which a piston segregates the sea water from the inside pressurised gas. To simplify the performance of the accumulator, the adiabatic index is chosen to be 1, indicating an isothermal process. Thence, we have

$$V_0 = V_{hyd} + V_{gas}, \tag{4.14}$$

$$p_a = \frac{p_0 V_0}{V_{gas}} = \frac{p_0 V_0}{V_0 - \int \Delta Q_a d\tau}, \tag{4.15}$$

where V_0, V_{hyd} and V_{gas} are the total volume of the accumulator, the seawater volume and gas volume in the accumulator. p_0 is the pressure in the accumulator when $V_{hyd} = 0$ and p_a is the pressure across the accumulator. Note that

$$p_a = p_{pm} \tag{4.16}$$

due to the physical connection between pump-motor and accumulator. The dynamics of the sea water volume in the accumulator is modelled as

$$\dot{V}_{hyd} = \Delta Q_a, \tag{4.17}$$

where

$$Q_a = Q_{pm} - Q_{rv}. \tag{4.18}$$

The accumulator's state-of-charge (SoC) is defined as

$$SoC = \frac{V_{hyd}}{V_0}, \tag{4.19}$$

and the energy stored in accumulator E_a is expressed as

$$E_a = \int_0^t P_{acc} d\tau = p_0 V_0 \ln \frac{V_0}{V_{gas}} = p_0 V_0 \ln \frac{1}{1 - SoC}, \tag{4.20}$$

where P_{acc} is the power flow of the accumulator.

4.3 Control design

The wind turbine operation is divided into 4 regions according to the wind speed. When the wind is below cut-in speed (region 1) or above the cut-out speed (region 4), the wind turbine doesn't work. When the wind is above the cut-in speed and below rated speed (region 2), the blade pitch keeps at fine position and torque controller works to maximize the power extraction. When the wind speed is above the rated speed and below cut-out speed (region 3), the pitch controller is activated to maintain rated wind turbine rotor speed, and operates together with torque controller to achieve rated power extraction. For conventional wind turbine, the torque control is usually achieved by the rotor-side-converter controller to regulates the electrical torque of the generator (usually DFIG), while the torque control in HWT is achieved by regulating the motor displacement rather than the electrical torque of generator, which indirectly adjusts the pump torque through the oil line to extract desired wind power. Like [144], the boundary speeds for these four region divisions in the present chapter are 3 m/s (cut-in speed), 11.4 m/s (rated speed) and 25 m/s (cut-out speed) respectively.

Fig. 4.2 shows the interaction between the HWT system and controllers. There are 7 controllers in this HWT system, namely, pump torque controller, accumulator state-of-charge controller, wind turbine pitch controller, pump-motor torque controller, relief valve controller, frequency (active power) controller, and excitation controller. The details of these controllers and the their interactions are expatiated in this section.

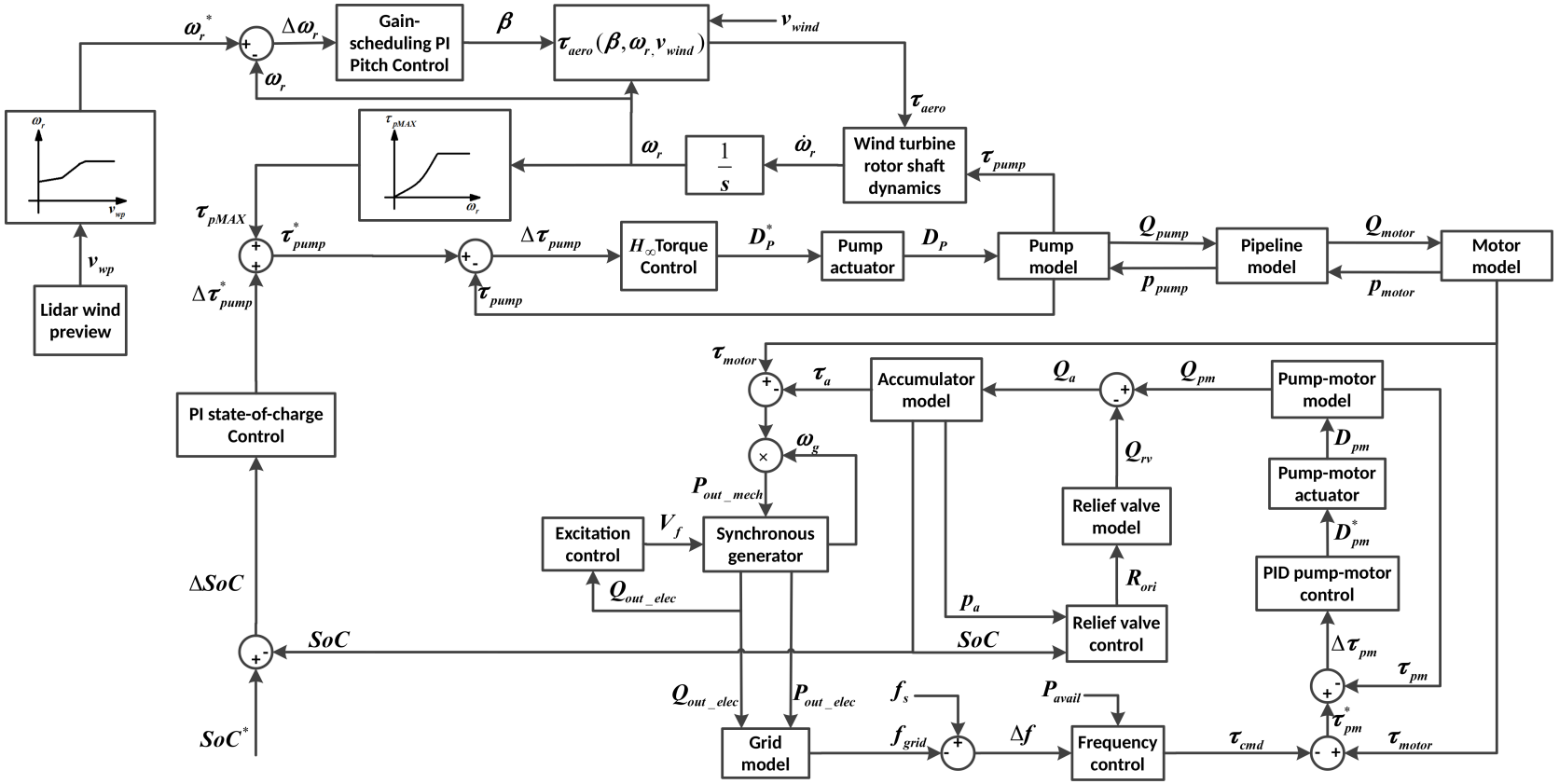

Figure 4.2: Block diagram of interactions between controllers and the hydrostatic wind turbine system connecting to the grid.

4.3.1 Wind turbine pitch control

The extractable wind power is defined as

$$P_{extract} = \frac{1}{2} C_p(\beta, \lambda) \rho \pi R^2 v_{wind}^3, \tag{4.21}$$

where ρ is the air density, R is the wind turbine blade length, v_{wind} is the rotor effective wind speed. The power coefficient C_p only depends on the pitch angle β and the tip speed ratio λ [69]. The definition of the tip speed ratio λ is

$$\lambda = \frac{\omega_r R}{v_{wind}}. \tag{4.22}$$

Usually in region 2 the pitch angle is forced to zero. When we have the optimal wind turbine rotor speed ω_r^*, the tip speed ratio reaches its optimal point λ^*, thus achieving maximum power coefficient C_p and realising the maximum power point tracking (MPPT) operation. Due to (4.22), the optimal wind turbine rotor speed ω_r^* linearly depends on the rotor effective wind speed v_{wind}. By utilizing the LIDAR simulator, v_{wind} can be estimated, based on which the optimal wind turbine rotor speed ω_r^* can be obtained. The details about the LIDAR wind preview are expatiated in Section 4.3.1.

In our scheme, we would still like to maintain MPPT operation in region 2 and store the excessive power in the accumulator. However, once the accumulator is full, the wind turbine is forced to operate at the sub-optimal point, ensuring the balance between generation and the load demand. It can be achieved by deviating the blade pitch angle from its original position to reduce the power extraction while the wind turbine rotor speed is maintained as what it is under MPPT operations. According to (4.21), the power coefficient will deviate from its optimal point, thus extracting less wind power. That is, the pitch control should be activated in both region 2 and region 3, in order to regulate the power extraction based on the SoC of the accumulator in all operation regions.

See (4.23) for the computed optimal wind turbine rotor speed, which is a tabulated function incorporating 5 control regions and serves as the reference for pitch controller.

$$\omega_r^* = \begin{cases} 12.1, & v_{wp} >= 11.4; \\ 11.68 + \dfrac{12.1 - 11.68}{11.4 - 10.2}(v_{wp} - 10.2), & v_{wp} \in [10.2, 11.4); \\ 8.96 + \dfrac{11.68 - 8.96}{10.2 - 7.8}(v_{wp} - 7.8), & v_{wp} \in [7.8, 10.2); \\ 6.87 + \dfrac{8.96 - 6.87}{7.8 - 4}(v_{wp} - 4), & v_{wp} \in [4, 7.8); \\ 0, & v_{wp} < 4, \end{cases} \tag{4.23}$$

where v_{wp} represents the previewed rotor effective wind by LIDAR. ω_r^* is expressed in revolutions per minute (rpm) and v_{wp} is in meters per second (m/s). The control region division is based on torque control region division in [71]. From the top to bottom in (4.23) are region 3, region 2.5, region 2, region 1.5 and region 1 respectively, where region 1.5 and region 2.5 are created for smooth transition between region 1, 2, 3.

A gain-scheduled PI controller with antiwindup (AW) compensator from [77, 144] is applied for wind turbine rotor speed regulation. The parameter $K_{p_{pit}}$ and $K_{I_{pit}}$ are set as

$$K_{p_{pit}} = -\frac{1.6167}{1 + \frac{\beta}{6.302336}} \text{ and } K_{I_{pit}} = -\frac{0.6929}{1 + \frac{\beta}{6.302336}},$$

with antiwindup back-calculation coefficient 0.5 [144]. β represents the blade pitch angles in degree.

LIDAR wind preview

In our scheme, Light and Detection Ranging (LIDAR) simulator is installed to the wind turbine nacelle, which mainly contribute to the wind turbine pitch control (See Fig. 4.2). The wind turbine-mounted LIDAR is able to provides a method for remote wind measurement and it has been proved to potentially improve the pitch control performance in may research applications and field works [51, 100, 125, 29, 36, 144]. LIDAR simulator emits the laser wave to the atmosphere and the laser wave is then scattered by aerosol particles, which is partially returned to the LIDAR. By making use of the Doppler shift of the returned radiations, we are able to estimate and compute the remote wind speed [51]. The frequency shift $\delta\nu$ can be written as

$$|\delta\nu| = \frac{2V_{LOS}}{c}\nu = \frac{2V_{LOS}}{\lambda},$$

where c is the light speed (3×10^8 m/s), ν and λ are the laser frequency and wavelength. V_{LOS} represents the component of target speed along the line-of-sight [51].

Similar to [144, 125, 124], the scanning trajectory of LIDAR in our simulations is to scan 8 points in each measurement circle for 5 circles in total (see Fig. 4.3). The half opening angle is 16.7° with distance between 63 m (0.5 times of blade diameter) and 189 m (1.5 times of blade diameter).

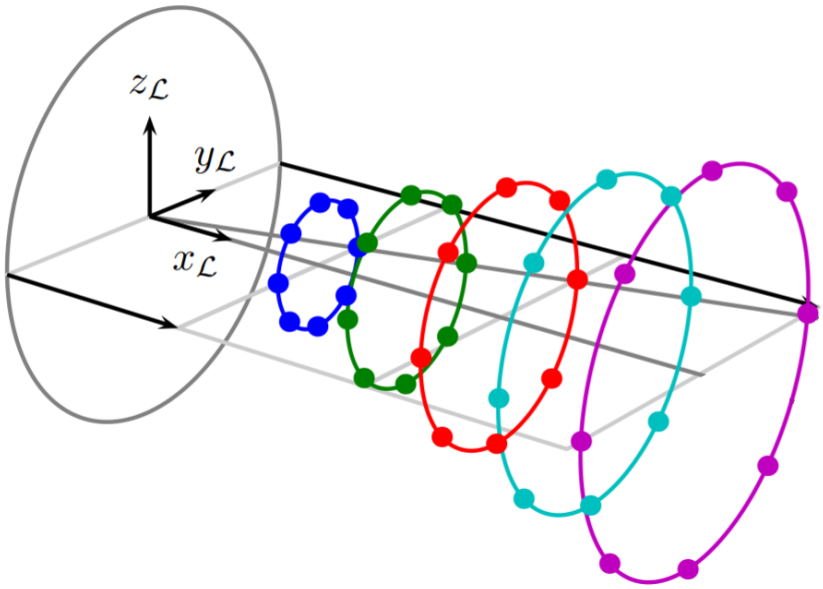

Figure 4.3: LIDAR scan trajectory. This figure is taken from [125].

4.3.2 Pump torque control

An $\mathcal{H}_\infty$ loopshaping torque controller is designed to govern the pump torque through adjusting the pump volumetric displacement D_p. The system equations are (4.3), (4.8), (4.6), (4.7) and (4.12), which can be linearised at the operating point ($\bar{\omega}_r$, $\bar{v}_{wind}$, $\bar{\beta}$):

$$\dot{\hat{\boldsymbol{x}}}_{\boldsymbol{\tau c}} = \boldsymbol{A}_{\boldsymbol{\tau c}}\hat{\boldsymbol{x}}_{\boldsymbol{\tau c}} + \boldsymbol{B}_{\boldsymbol{\tau c}}\hat{D}_p^* + \boldsymbol{B}_{\boldsymbol{\tau cd}}\hat{\boldsymbol{d}}, \tag{4.24}$$

$$\hat{\tau}_{pump} = \boldsymbol{C}_{\boldsymbol{\tau c}}\hat{\boldsymbol{x}}_{\boldsymbol{\tau c}} + D_{\tau c}\hat{D}_p^*, \tag{4.25}$$

in which $\hat{\boldsymbol{x}}_{\boldsymbol{\tau c}} = \boldsymbol{x}_{\boldsymbol{\tau c}} - \bar{\boldsymbol{x}}_{\boldsymbol{\tau c}} = \begin{bmatrix}\hat{\omega}_r & \hat{D}_p & \hat{\boldsymbol{x}}_{\boldsymbol{l}} & \hat{\omega}_g\end{bmatrix}^T$, $\hat{D}_p^* = Dp^* - \bar{D}_p$, $\hat{\boldsymbol{d}} = \boldsymbol{d} - \bar{\boldsymbol{d}} = \begin{bmatrix}\hat{v}_{wind} & \hat{\tau}_g & \hat{\tau}_{pm}\end{bmatrix}^T$, and $\hat{\tau}_{pump} = \tau_{pump} - \bar{\tau}_{pump}$. The operating points are selected to be $\bar{\omega}_r = 10.3$ rpm, $\bar{v}_{wind} = 9$ m/s and $\bar{\beta} = 0°$.

In (4.24) and (4.25), the matrices $\boldsymbol{A_{\tau c}}$, $\boldsymbol{B_{\tau c}}$, $\boldsymbol{B_{\tau cd}}$, $\boldsymbol{C_{\tau c}}$ and $D_{\tau c}$ are derived as

$$\boldsymbol{A_{\tau c}} = \begin{bmatrix} \frac{\partial \tau_{aero}}{\partial \omega_r} - B_p & \frac{-(1+C_{fp})\boldsymbol{C_{l1}}\bar{\boldsymbol{x}}_{\boldsymbol{l}}}{J_r+J_p} & \boldsymbol{A_{13}} & 0 \\ \frac{J_r+J_p}{0} & -\frac{1}{T_p} & \boldsymbol{0} & 0 \\ \boldsymbol{B_{l1}}\bar{D}_p & \boldsymbol{B_{l1}}\bar{\omega}_r & \boldsymbol{A_{33}} & \boldsymbol{B_{l2}}D_m \\ 0 & 0 & \boldsymbol{A_{43}} & \frac{-B_m}{J_m+J_{pm}+J_g} \end{bmatrix}$$

where $\boldsymbol{A_{33}} = \boldsymbol{A_l} - C_{sp}\boldsymbol{B_{l1}}\boldsymbol{C_{l1}} + C_{sm}\boldsymbol{B_{l2}}\boldsymbol{C_{l2}}$,

$$\boldsymbol{A_{13}} = \frac{-(1+C_{fp})\boldsymbol{C_{l1}}\bar{D}_p}{J_r + Jp}, \quad \boldsymbol{A_{43}} = \frac{(1+C_{fm})D_m\boldsymbol{C_{l1}}}{J_m + J_{pm} + J_g};$$

$$\boldsymbol{B_{\tau c}} = \begin{bmatrix} 0 & \frac{1}{T_p} & \boldsymbol{0} & 0 \end{bmatrix}^T;$$

$$\boldsymbol{B_{\tau cd}} = \begin{bmatrix} \frac{\partial \tau_{aero}}{\partial v_{wind}} & 0 & 0 \\ \frac{J_r+J_p}{0} & 0 & 0 \\ \boldsymbol{0} & \boldsymbol{0} & \boldsymbol{0} \\ 0 & -\frac{1}{J_m+J_{pm}+J_g} & -\frac{1}{J_m+J_{pm}+J_g} \end{bmatrix};$$

$$\boldsymbol{C_{\tau c}} = \begin{bmatrix} B_p & (1+C_{fp})\boldsymbol{C_{l1}}\bar{\boldsymbol{x}}_{\boldsymbol{l}} & (1+C_{fp})\boldsymbol{C_{l1}}\bar{D}_p & 0 \end{bmatrix};$$

and

$$D_{\tau c} = \begin{bmatrix} 0 \end{bmatrix}.$$

The system from pump displacement command D_p^* to pump torque τ_{pump} are denoted as a 24-order plant G_m with its state-space realisation ($\boldsymbol{A_{\tau c}}$, $\boldsymbol{B_{\tau c}}$, $\boldsymbol{C_{\tau c}}$, $D_{\tau c}$). The Hankel singular value of the plant G_m is shown in Fig. 4.4. From this figure, we can safely discard the last 8 states whose Hankel singular values are small and reduce the plant order to 16. It can be achieved by matching DC-gain method using Matlab command *balred*. See Fig. 4.5 for the bode diagrams of the plant G_m and the reduced-order plant G_{mr}. It is clear that the reduced-order system G_{mr} matches G_m very well at low frequency (< 73 Hz).

For this linear time-invariant system G_{mr}, the $\mathcal{H}_\infty$ loopshaping controller K_τ is computed by the Matlab controller synthesis tool *loopsyn*. The desired shape of the open-loop system frequency response is firstly specified and then the *loopsyn* computes the stabilising controller which best approximates the specified loop shape. It demonstrates the basic idea of the 'loop shaping' frequency domain controller design mechanism. That is, by applying *loopsyn*, the singular value plot of the open-loop transfer function $G_{mr}K_\tau$

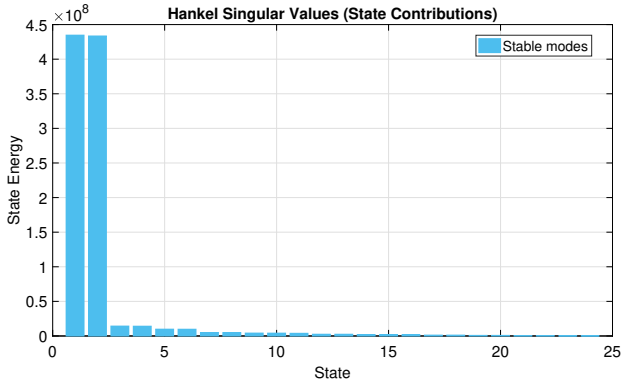

Figure 4.4: The Hankel singular values of the plant G_m.

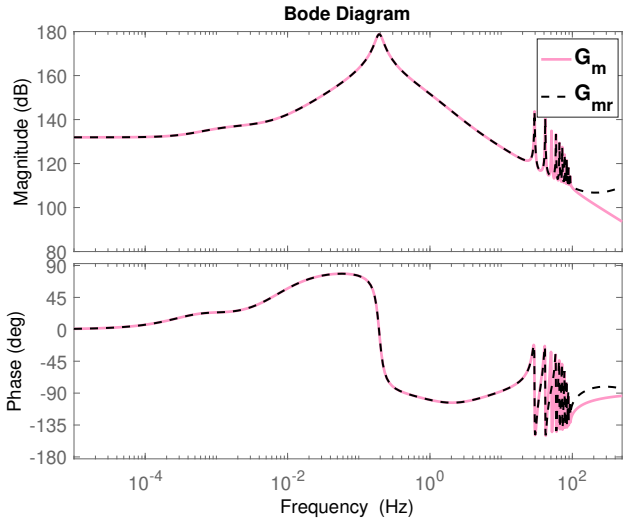

Figure 4.5: Bode diagram for the plant G_m and the reduced-order plant G_{mr}.

will match the singular value plot of the specified desired open-loop shape G_d with the accuracy γ in the sense that:

$$\underline{\sigma}(G_{mr}(j\omega)K_\tau(j\omega)) \leq \frac{1}{\gamma}\underline{\sigma}(G_d(j\omega)) \text{ for all } \omega > \omega_0, \text{ and,}$$

$$\underline{\sigma}(G_{mr}(j\omega)K_\tau(j\omega)) \leq \gamma\underline{\sigma}(G_d(j\omega)) \text{ for all } \omega > \omega_0,$$

where ω_0 is the crossover frequency of the singular value plot.

The design procedure of this $\mathcal{H}_\infty$ loopshaping controller K_τ under the Matlab command *loopsyn* is mainly divided into three steps: Firstly, to get the pre-compensator

W_{pre} by loop shaping, then to design the optimal controller K_∞ for the plant G_s with robust stability guaranteed, and finally the $\mathcal{H}_\infty$ loopshaping controller can be acquired from W_{pre} and K_∞ (see Fig. 4.6) [94].

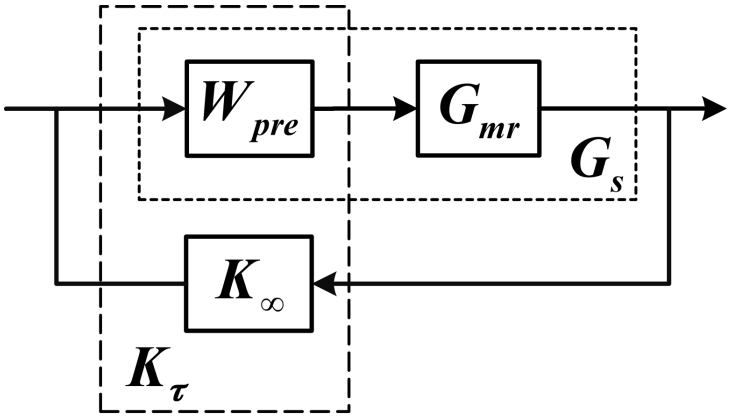

Figure 4.6: The design procedure of the $\mathcal{H}_\infty$ loopshaping controller.

Loop shaping is to apply a state-space construction method (see Theorem 3.1 in [78]) for rational matrix greatest common divisors (GCD's) to compute a stable minimum-phase squaring-down pre-compensator W_{pre} for the reduced-order plant G_{mr}, such that the shape plant $G_s = W_{pre}G_{mr}$ is square and is a greatest common right divisor (GCRD) of the reduced-order plant G_{mr} [78, 34]. We demonstrate the reduced-order plant G_{mr} is a continuous LTI system. It is a full rank matrix and have a state-space realisation (not necessarily minimum)

$$G_{mr} \stackrel{\text{S}}{=} \left[\begin{array}{c:c} A_{mr} & B_{mr} \\ \hdashline C_{mr} & D_{mr} \end{array}\right], \tag{4.26}$$

and it has no finite zeros on $j\omega$-axis. In this way, the singular values of the desired shape G_d should be highly in consistent with the singular values of G_s in the frequency range of $(0, \infty)$. That is

$$\sigma(G_d) \approx \sigma(G_s) \text{ for all } \omega \in (0, \infty).$$

Then it is required to find out an optimal controller K_∞ to maximize the stability margin and stabilise the shape plant G_s [49, 48] at the same time. We defined $\tilde{M}_s$ and $\tilde{N}_s$ as the normalized coprime factors of shape plant G_s, such that

$$G_s = \tilde{M}_s^{-1}\tilde{N}_s,$$

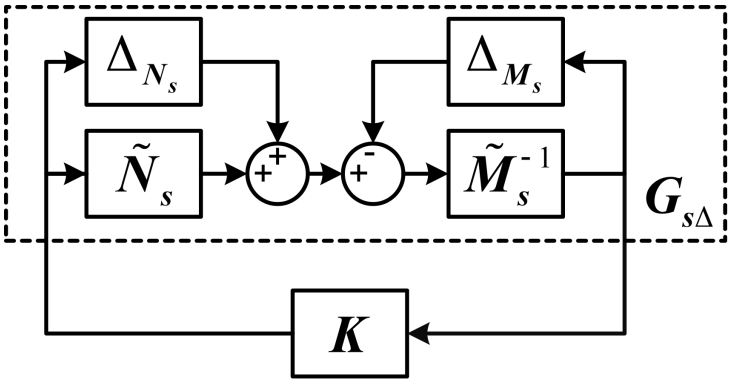

Figure 4.7: Perturbed plant $G_{s\Delta}$.

$$\tilde{M}_s\tilde{M}_s^* + \tilde{N}_s\tilde{N}_s^* = I.$$

The perturbed plant $G_{s\Delta}$ is written as

$$G_{s\Delta} = (\tilde{M}_s + \Delta_{M_s})^{-1}(\tilde{N}_s + \Delta_{N_s}),$$

where Δ_{M_s} and Δ_{N_s} are stable unknown transfer functions representing the uncertainties (see Fig. 4.7). They should satisfy

$$\left\| \begin{bmatrix} \Delta_{M_s} & \Delta_{N_s} \end{bmatrix} \right\|_\infty < \epsilon,$$

where ϵ is the stability margin and $\epsilon > 0$. Note that $\epsilon = \frac{1}{\gamma}$. Then, the synthesis stabilising controller K is designed to stabilise all such $G_{s\Delta}$ for a given ϵ [149]. That is

$$\left\| \begin{bmatrix} I \\ K \end{bmatrix} (I - G_{s\Delta}K)^{-1}\tilde{M}_s^{-1} \right\|_\infty \leq \epsilon^{-1}.$$

The optimal controller K_∞ is achieved when $\epsilon = \epsilon_{max}$, where

$$\epsilon_{max}^2 = 1 - \left\| \begin{bmatrix} \tilde{M}_s & \tilde{N}_s \end{bmatrix} \right\|_H^2.$$

$\|\cdot\|_H$ represents the Hankel norm and ϵ_{max} is the maximum stability margin.

Finally the $\mathcal{H}_\infty$ loopshaping torque controller K_τ is defined as

$$K_\tau = W_{pre} \cdot K_\infty.$$

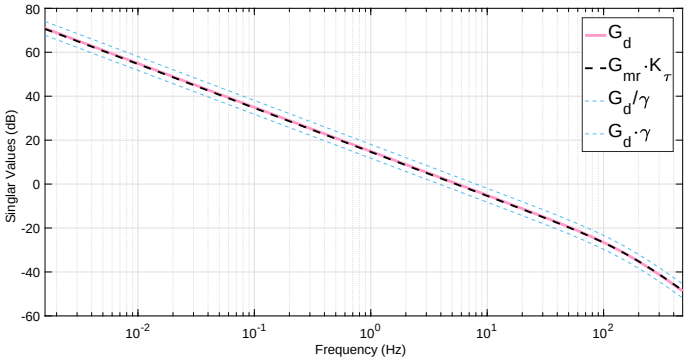

Figure 4.8: Singular value plots of open loop transfer function $G_{mr}K_\tau$ and desired loop shape G_d.

Here, the desired open-loop system frequency response is specified as

$$G_d = \frac{35000}{(s+10^{-12})(s+1000)}, \tag{4.27}$$

where the gain is high at low frequency indicating low tracking error in the steady state with gain crossover frequency of 35 rad/s. The roll-off at high frequency is -40 dB/decade which imply the good robustness and fast tracking performance.

Fig. 4.8 represents the singular value plot of the open loop transfer function $G_{mr}K_\tau$ and its desired loop shape G_d. It shows that with the control of K_τ, the open loop transfer function $G_{mr}K_\tau$ tracks the desired loop shape G_d very well. Fig. 4.9 shows the closed-loop step response which has no overshoot with a settling time of 0.1127 second. The settling time here is defined as the time it takes for $y(t) - y_{final}$ to fall below 2% of its peak value, where $y(t)$ and y_{final} represent the system response at time t and the steady-state response. The stability margin ϵ is 0.6954, the phase margin is 61.03°, and the crossover frequency ω_0 is 30 rad/s.

4.3.3 Accumulator state-of-charge control

As mentioned in Section 4.3.1, blade pitch angles will deviate from its original position once the accumulator is full. The pitch controller will maintain the wind turbine rotor speed ω_r according to (4.23) and the change in pump torque will lead to the change in blade pitch angles. Hence we regulate the pitch angle by redefining the pump torque reference according to accumulator's SoC. Then the pitch angle will be automatically tuned to its desired position via proper pitch control.

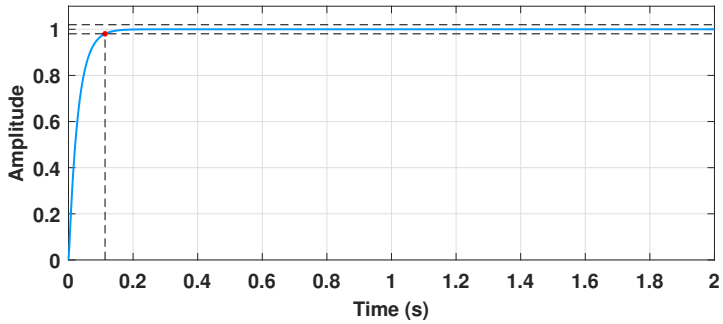

Figure 4.9: Closed-loop step response of the $\mathcal{H}_\infty$ loopshaping controller K_τ.

Here, the SoC of the accumulator is preserved at a relatively high level to retain enough power in case of the high load demand under low wind speed. The HWT extracts more power than what required by the grid to charge the accumulator when wind is abundant, and reduce the power extraction if the accumulator is under the risk of being overcharged. It means that the SoC of the accumulator serves as a feedback to adjust the power extraction, namely, adjusting the reference of pump torque τ^*_{pump}.

The NREL 5-MW conventional gearbox-equipped wind turbine provides the relationship between generator torque and turbine rotor speed under MPPT operation [71]. It can be modified and mapped from the generator-rotor-shaft side to the wind-turbine-rotor-shaft side, which reflects the relationship between pump torque under MPPT operation τ_{pMAX} and the wind turbine rotor speed ω_r (see (4.28)).

$$\tau_{pMAX}(\omega_r) = \begin{cases} \dfrac{Pwr_0}{\omega_r} & \omega_r >= 1.267; \\ K_0\omega_r^2 + \dfrac{\frac{Pwr_0}{\omega_r} - K_0\omega_r^2}{1.267 - 1.255}(\omega_r - 1.255) & \omega_r \in [1.255, 1.267); \\ K_0\omega_r^2 & \omega_r \in [0.940, 1.255); \\ \dfrac{K_0\omega_r^2}{0.940 - 0.724} \cdot (\omega_r - 0.724) & \omega_r \in [0.724, 0.940); \\ 0 & \omega_r < 0.724, \end{cases} \tag{4.28}$$

Note that the region division is provided by [71], which is in accordance with (4.23). Pwr_0 represents the rated rotor power in Watt. Wind turbine rotor speed ω_r is radian per second (rad/s), τ_{pMAX} is in Newton meter (Nm) and K_0 is a constant. Then

the available power Pwr_{avail} can be calculated as

$$Pwr_{avail} = \tau_{pMAX} \cdot \omega_r. \tag{4.29}$$

The accumulator's SoC indicates how much the pump torque should be deviated from τ_{pMAX}, which is marked as $\Delta\tau^*_{pump}$ in Fig. 4.2. We apply a PI controller to compute how much the power extraction ΔPwr and parameter ΔK should be deviated from the available power Pwr_{avail} and the constant K_0. The difference $SoC^* - SoC$ is denoted as ΔSoC where SoC^* is a constant:

$$\Delta Pwr = K_{p_{SoC}} \Delta SoC + K_{I_{SoC}} \int \Delta SoC d\tau. \tag{4.30}$$

$K_{p_{SoC}}$ and $K_{I_{SoC}}$ are the proportional and integral gain of the PI controller, and

$$\Delta K = K_0 \frac{\Delta Pwr}{Pwr_{avail}}. \tag{4.31}$$

Note that the SoC is in the range of [0, 90%] due to the compressible limit of the gas. Once the SoC is over 85%, the accumulator starts to store in less energy than requested. When SoC reaches its upper limit 90%, the accumulator completely stop working until it is requested to release energy. Similarly, when SoC is dropped down below 5%, the accumulator will start to release less energy than requested. When SoC reaches zero, the accumulator completely stop working until it is requested to store energy. We need guarantee the relatively smooth transition when we have to exclude the operation of accumulator. It will inevitably lead to a small period of variation in grid frequency due to the unbalance between power generation and load demand, but the frequency will be brought back to normal once the accumulator's SoC returns to [5%, 85%]. We have designed a proper controller to maintain the SoC within the range [5%, 85%].

By substituting the Pwr_0 and K_0 in (4.28) with ΔPwr and ΔK, we get the

expression of $\Delta\tau^*_{pump}$:

$$\Delta\tau^*_{pump}(\omega_r) = \begin{cases} \dfrac{\Delta Pwr}{\omega_r} & \omega_r >= 1.267; \\ \Delta K\omega_r^2 + \dfrac{\frac{\Delta Pwr}{\omega_r} - \Delta K\omega_r^2}{1.267 - 1.255}(\omega_r - 1.255) & \omega_r \in [1.255, 1.267); \\ \Delta K\omega_r^2 & \omega_r \in [0.940, 1.255); \\ \dfrac{\Delta K\omega_r^2}{0.940 - 0.724} \cdot (\omega_r - 0.724) & \omega_r \in [0.724, 0.940); \\ 0 & \omega_r < 0.724. \end{cases} \tag{4.32}$$

Then the commanded torque τ^*_{pump} becomes

$$\tau^*_{pump}(\omega_r) = \tau_{pMAX}(\omega_r) + \Delta\tau^*_{pump}(\omega_r). \tag{4.33}$$

Note that the range for $\Delta\tau^*_{pump}(\omega_r)$ is set to be $[-\tau_{pMAX}(\omega_r),\ 0.1\tau_{pMAX}(\omega_r)]$.

4.3.4 Pump-motor torque control

A PID pump-motor torque controller is designed to regulate the pump-motor torque τ_{pm} by adjusting the volumetric displacement of pump-motor D_{pm}. The system transfer function can be computed from (4.9), (4.10), (4.11), (4.14), (4.15) and (4.18) as

$$\tau_{pm}(s) = \frac{\eta_{\tau pm} p_0 V_0 D^*_{pm}}{(T_{pm}s + 1)(V_0 - \omega_g \eta_{Qpm} D^*_{pm} \cdot \frac{1}{T_{pm}s^2 + s} + \frac{1}{s} Q_{rv})}, \tag{4.34}$$

where the system input, output and disturbance are D^*_{pm}, τ_{pm} and Q_{rv} respectively. The control structure is shown in Fig. 4.2. A PID controller with a first order filter on derivative term is utilised:

$$D^*_{pm}(s) = (K_{p_{D_{pm}}} + \frac{K_{I_{D_{pm}}}}{s} + \frac{K_{D_{D_{pm}}} s}{T_f s + 1})\Delta\tau_{pm}, \tag{4.35}$$

where $\Delta\tau_{pm} = \tau^*_{pm} - \tau_{pm}$. The parameters $K_{p_{D_{pm}}}$, $K_{I_{D_{pm}}}$, $K_{D_{D_{pm}}}$ are the proportional, integral and derivative gain of the PID controller and T_f is the filter coefficient. They are listed in Table 4.1. See Fig.4.10 for the close-loop step response of the PID pump-motor controller. It is clear that there is small overshoot (3.6%) with fast settling time of 0.0979 seconds. Again, the settling time here is set to be the time when the variation of system response starts to stay within 2% of the maximum difference.

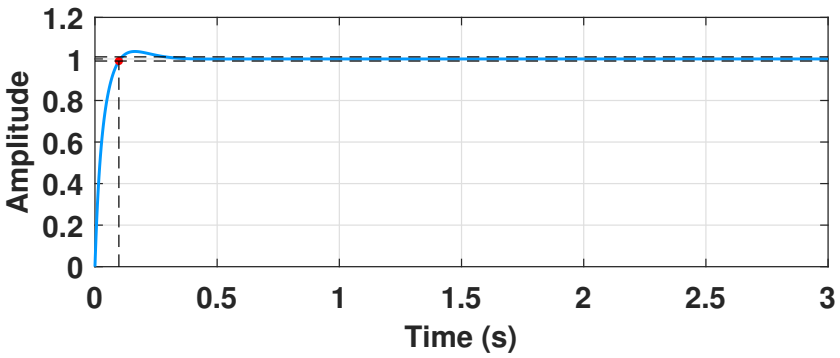

Figure 4.10: Close-loop step response of the PID pump-motor controller.

4.3.5 Relief valve protection control

In an emergency such as abrupt lost of loads, the grid requests a sudden reduction in power generation in order to limit the frequency rise. Thence, a large amount of power has to be stored in the accumulator in a short time, since the response of pitch regulation is not fast enough to reduce the power extraction due to its mechanical response speed. In this case, the accumulator is placed at the risk of being overcharged, which can be protected by a relief valve. It starts operation when the hydraulic volume V_{hyd} in the accumulator reaches 80% of the accumulator total volume V_0. When V_{hyd} reaches 85% of V_0, the relief valve is opened to its maximum.

The relief valve orifice area $A = \pi R_{ori}^2$ is controlled according to a tabulated function:

$$R_{ori} = \begin{cases} R_{min}, & SoC <= 0.8; \\ R_{max}, & SoC >= 0.85; \\ R_{min} + \dfrac{SoC - 0.8}{0.85 - 0.8}(R_{max} - R_{min}), & otherwise; \end{cases}$$

The unit for R_{ori}, R_{min} and R_{max} is meter (m).

4.3.6 Excitation control

The excitation control is to regulate the terminal voltage of the synchronous generator, and provide the excitation for the synchronous generator at the same time [131]. Since the output reactive power is highly related to the terminal voltage of a synchronous

generator, the reactive power will be regulated at the same time by the excitation control. Different from the conventional wind turbine (WT), the HWT system is connected to the synchronous generator (SG) rather than DFIG, that is, we regulate the reactive power via excitation control rather than the converter control in the conventional WT grid connection system.

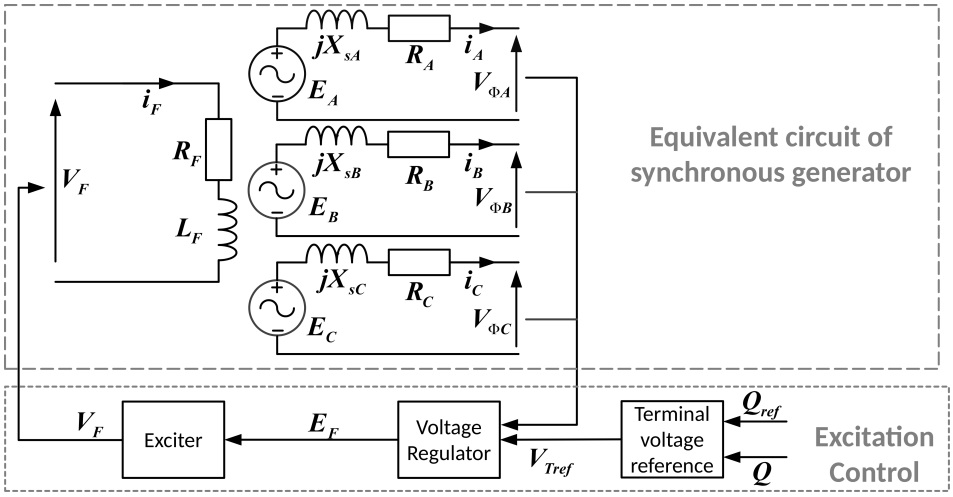

Figure 4.11: Three-phase equivalent circuit of a synchronous generator with the excitation control scheme. R_F and L_F are the resistance and leakage inductance in field winding.

See Fig. 4.11 for the three-phase equivalent circuit of a synchronous generator with its excitation control scheme. The RMS internal induced voltage $E_{A,B,C}$ is

$$E_{A,B,C} = \sqrt{2}\pi N_c \phi \omega \tag{4.36}$$

where N_c represents the turns of the stator windings, ω represents the rotational speed and ϕ is the magnetic flux induced by the field current i_F. From the equivalent circuit (Fig. 4.11), we can easily obtain that

$$V_{\Phi A,\Phi B,\Phi C} = E_{A,B,C} - jX_{sA,sB,sC} \cdot i_{A,B,C} - R_{A,B,C} \cdot i_{A,B,C}, \tag{4.37}$$

where $V_{\Phi A,\Phi B,\Phi C}$ and $i_{A,B,C}$ are the generator terminal phase voltage and current. $R_{A,B,C}$ and $X_{sA,sB,sC}$ are the resistance and reactance in the stator phase A, B and C. Note that the reactance including the self-inductance and armature reactance.

From Fig. 4.11 and Equation (4.36), it is clear that by tuning the field voltage V_F, we are able to control the field current i_F, thus inducing the desired magnetic flux ϕ

for the desired induced voltage $E_{A,B,C}$. Then according to (4.37), the desired generator terminal phase voltage $V_{\Phi A,\Phi B,\Phi C}$ can be obtained.

Though there are many methods proposed for the terminal voltage regulation [11, 122, 13, 164, 79], in this chapter the voltage regulator is selected to be a simple PI controller from [131, 30]. It is achieved from a ready-to-use block called '*Excitation System*' provided in the *Simscape* library in Matlab/Simulink. The transfer function from E_F to V_F ('exciter' block in Fig. 4.11) is simplified as [30]:

$$\frac{V_F}{E_F} = \frac{1}{K_e + T_e s},$$

where K_e and T_e are the gain and time constant. The terminal voltage reference V_{Tref} (see Fig. 4.11) is selected to be

$$V_{Tref} = 0.05 \cdot \int_0^{\tau} (Q_{ref} - Q) d\tau. \tag{4.38}$$

where V_{Tref} is expressed in p.u. with respect to the base value setting to be 730 V (line-to-line) and Q_{ref} and Q are also expressed in p.u. with respect to the base value of 5 MVar.

4.3.7 Frequency (active power) control

According to (4.12), τ_{pm} is a key term to stabilise the generator speed (or system frequency) under uncontrollable wind fluctuations and load variations. Hence, we need to compute a reference pump-motor torque τ_{pm}^* to compensate the difference between motor torque and electrical torque, which represents the difference between extracted power and grid request. Then, by proper pump-motor torque control, the real torque will be regulated to track this reference, thus stabilising the system frequency. A PI controller is applied to calculate the required power for the grid:

$$P_{cmd} = D_{cmd} P_{avail} + K_{p_{fc}} \Delta f + K_{I_{fc}} \int \Delta f dt, \tag{4.39}$$

where D_{cmd} is the power de-rating coefficient from the system operator. It can be adjusted due to the wind forecast or load forecast every few hours. We take it as a constant for simplicity in our simulations. Δf is the normalised frequency difference between 1 p.u. (60 Hz) and actual system frequency. $K_{p_{fc}}$ and $K_{I_{fc}}$ are the proportional and integral gain of the PI controller. Then, the pump-motor torque reference is expressed

as:

$$\tau_{pm}^{*} = \tau_{motor} - \frac{P_{cmd}}{\omega_g}. \tag{4.40}$$

It serves as the reference for the PID pump-motor torque controller.

4.4 Simulation studies

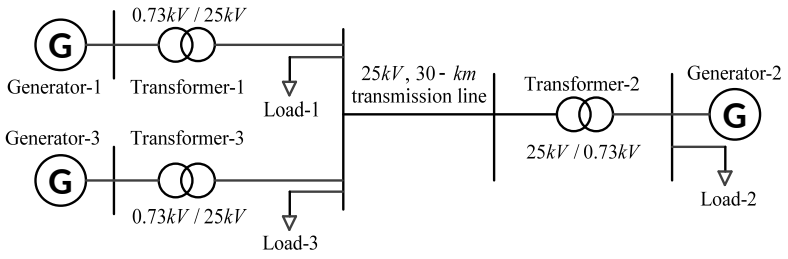

Figure 4.12: Single line diagram of the grid model.

In this section, a 500-second simulation is conducted to test the performances of the control scheme with variable load demand under turbulent wind. NREL Turbism [70] is utilised to generate stochastic, full-field, and turbulent wind flows for simulation studies. The International Electro-technical Commission (IEC) Kaimal spectral NTM (normal turbulence model) in Turbsim is applied to generate the wind condition, with most turbulent characteristics (category A). The mean hub-height longitudinal wind speed is 11.4 m/s and the height of the reference wind turbine is 90 m. The grid frequency is set to be 60 Hz in the simulations due to the default setting from the NREL wind turbine model. Fig. 4.13 shows the turbulent wind, the rotor effective wind speed which is computed by FAST AeroDyn, and its estimations by LIDAR respectively, which implies LIDAR estimated wind tracks the low frequency trajectory of the rotor effective wind speed very well.

In the 5-bus grid model (see Fig. 4.12), the power outputs of generator-2 and generator-3 keep unchanged at 10 MW and 1 MW, to balance the constant load-2 and load-3 which are 10 MVA and 1 MVA respectively. The variation in Load-1 demand should be within the generator rating, namely 5 MVA. We alter load-1 demand every 100 seconds within the range of [2.5, 4.5] MW to demonstrate the control performance of the HWT (see Fig. 4.14). Table 4.1 shows the parameters of the system and controllers. Fig. 4.15-4.21 show the simulation results of the proposed coordinated control strategy.

Fig. 4.15 shows the wind turbine rotor speed in revolution per minute (rpm) together with its reference ω_r^*, which is computed from the previewed wind (see Fig. 4.13) by

Table 4.1: System and control parameters.

Symbol	Value	Unit	Symbol	Value	Unit	Symbol	Value	Unit
System Parameters								
C_{sp}	7.1×10^{-11}	$m^3/(s{\cdot}Pa)$	C_{fp}	0.02	-	f_s	60	Hz
C_{sm}	7.0×10^{-11}	$m^3/(s{\cdot}Pa)$	C_{fm}	0.02	-	ω_r^*	12.1	rpm
D_m	4.1609×10^{-4}	m^3/rad	B_p	50000	Nms	V_0	5	m^3
J_r	38759236	kgm^2	B_m	2.5	Nms	p_0	5	Mpa
J_p	3680	kgm^2	T_p	0.1	sec	$P_{Generator-1}$	5	MW
J_m	534.116	Kgm^2	T_{pm}	0.1	sec	$P_{Generator-2}$	15	MW
J_{pm}	50	kgm^2	η_{Qpm}	0.95	-	$P_{Generator-3}$	1	MW
J_g	50	kgm^2	η_{rpm}	0.98	-	S_{Load-2}	10	MVA
ρ_{sw}	1035	kg/m^3	C_D	0.7	-	S_{Load-3}	1	MVA
ν	1.05×10^{-6}	m^2/s	Re_{cr}	20	-			
Control Parameters								
Pwr_0	5.2966	MW	K_{pSoC}	1×10^8	-	T_f	0.0227	-
K_0	2128618.65	$Nm/(rad/s)^2$	K_{ISoC}	4.42×10^5	-	SoC^*	0.7	-
Q_{ref}	0	p.u.	$K_{pD_{pm}}$	5.63×10^{-7}	-	$K_{p_{fc}}$	7.945×10^8	-
R_{min}	2×10^{-8}	m	$K_{ID_{pm}}$	8.65×10^{-6}	-	$K_{I_{fc}}$	1.589×10^8	-
R_{max}	0.2	m	$K_{DD_{pm}}$	3.84×10^{-9}	-	D_{cmd}	0.6	-

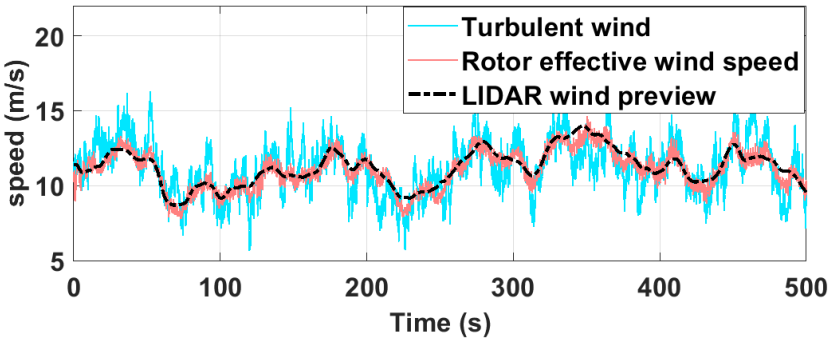

Figure 4.13: Turbulent wind, rotor effective wind and LIDAR wind preview.

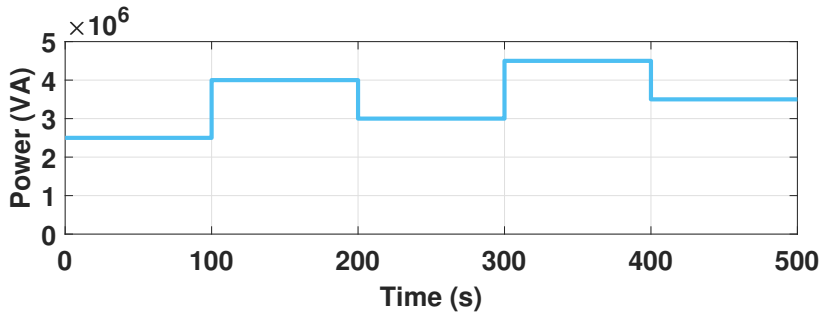

Figure 4.14: Load-1 demand variations.

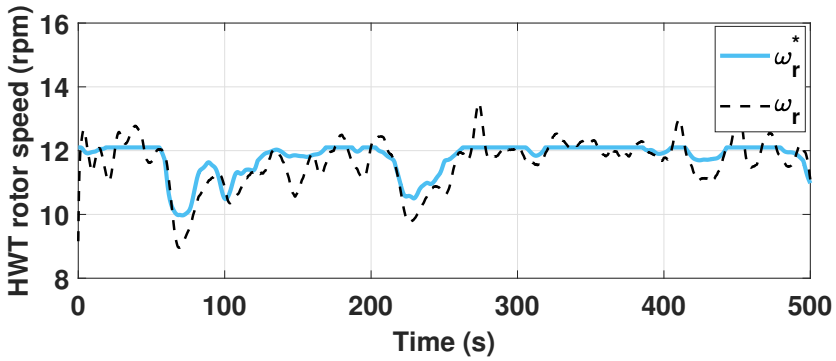

Figure 4.15: Wind turbine rotor speed.

LIDAR due to (4.23). The results indicate that actual wind turbine rotor speed ω_r roughly follows its reference ω_r^* by proper pitch control. The tracking performances of the $\mathcal{H}_\infty$ loopshaping pump torque controller and PID pump-motor torque controller are both excellent, which are shown in Fig. 4.16 and Fig. 4.17 respectively. Fig. 4.18

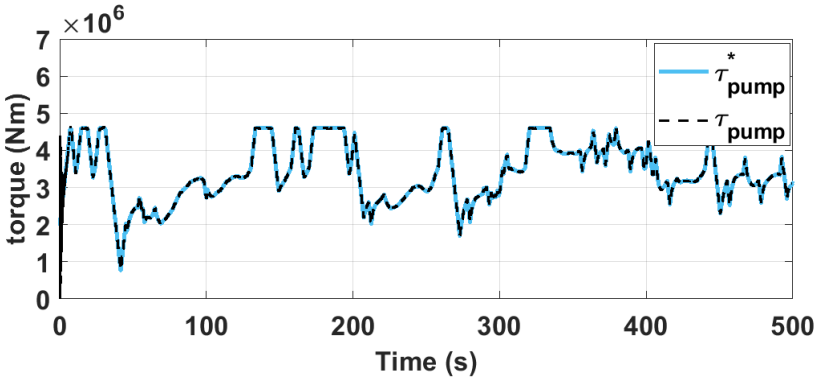

Figure 4.16: Pump torque and its reference.

shows the state-of-charge of the accumulator. It is controlled to stay at a relatively high level (70%) without exceeding its limit (90%). The fluctuation is mainly due to the wind conditions. Fig. 4.19 shows the output reactive power, which keeps at zero due to the effective excitation control. Fig. 4.20 shows the generator-1 power output, load-1 demand, wind turbine power extraction, and power flow in the accumulator. With proper coordination between the power extraction and power storage, the power output matches the load demand very well, indicating the effective regulation performance of the frequency (active power) controller in case of load variation with turbulent wind, see system frequency response in Fig. 4.21.

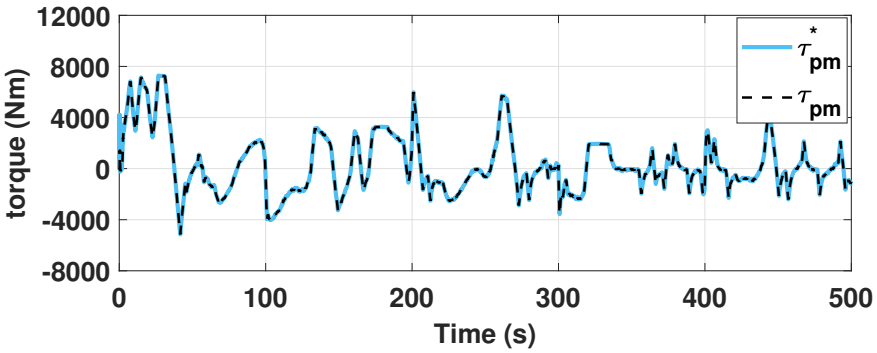

Figure 4.17: Pump-motor torque and its reference.

We now do a test to increase the frequency regulation capability of HWT. We double the size of the accumulator, and increase the power rating of the generator by 20% (from 5 MW to 6 MW), while keeping the turbine's mechanical configuration unchanged (i.e. 5 MW). The increased capacity of generator corresponds to the energy stored in the

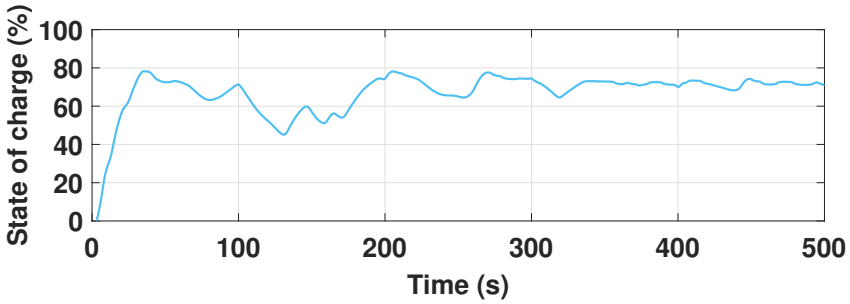

Figure 4.18: State-of-charge (SoC) of the accumulator.

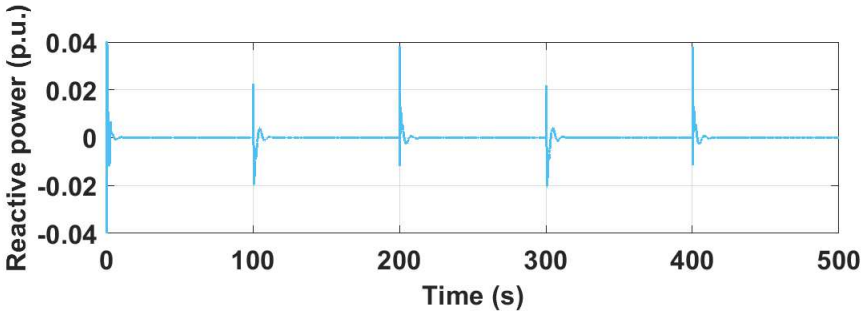

Figure 4.19: Reactive power output of the generator-1.

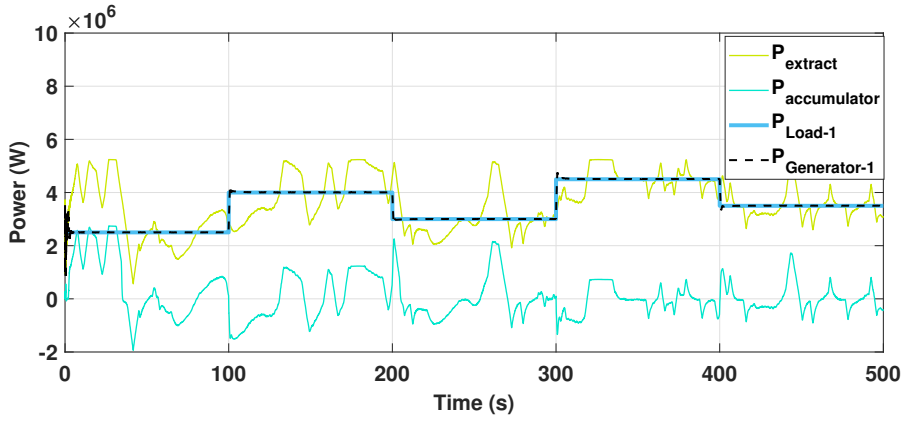

Figure 4.20: Power extraction of wind turbine, power output of generator-1, load-1 demand and power flow of the accumulator.

accumulator. We use the same wind input (see Fig. 4.13) and the same load-1 demand (see Fig. 4.14) as before for simulation test. We cut off generator-3 (whose capacity is 1 MW) during 320 – 380 seconds. To balance the load, HWT is required to output 5.5 MW during this period.

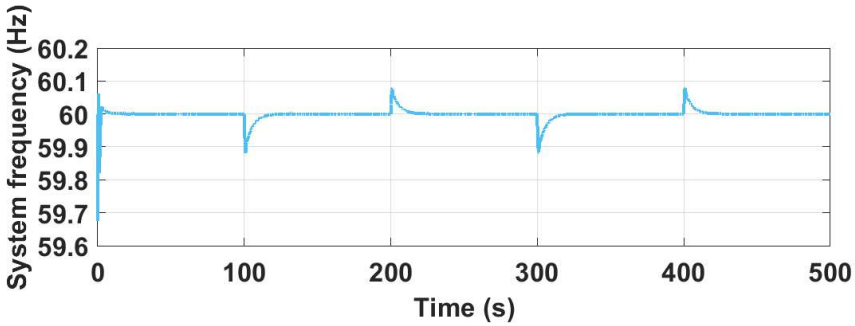

Figure 4.21: System frequency response in Hz.

Fig. 4.22 shows the state-of-charge of the accumulator. There is a clear reduction in SoC during 320 – 380 seconds. The released energy is used to feed the load of generator-3 (S_{load-3}). Fig. 4.23 shows the power output of generator-1, generator-2, generator-3 ($P_{Generator-1}$, $P_{Generator-2}$, $P_{Generator-3}$) and load-1 demand (S_{load-1}). It is clear that during 320 – 380 seconds, generator-1 produces more power when generator-3 is lost. Fig. 4.24 shows that the system frequency is maintained at 60Hz when generator-3 is lost.

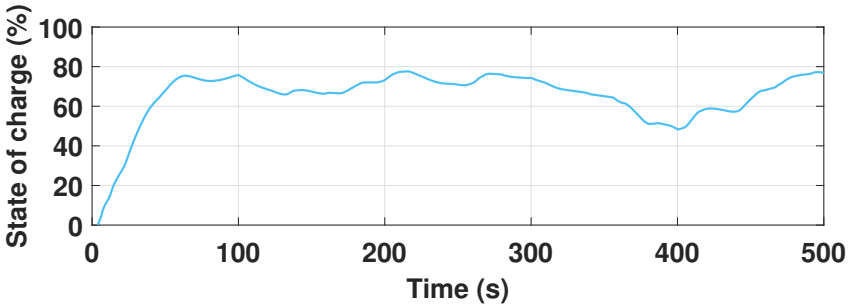

Figure 4.22: State-of-charge (SoC) of the extended hydraulic accumulator.

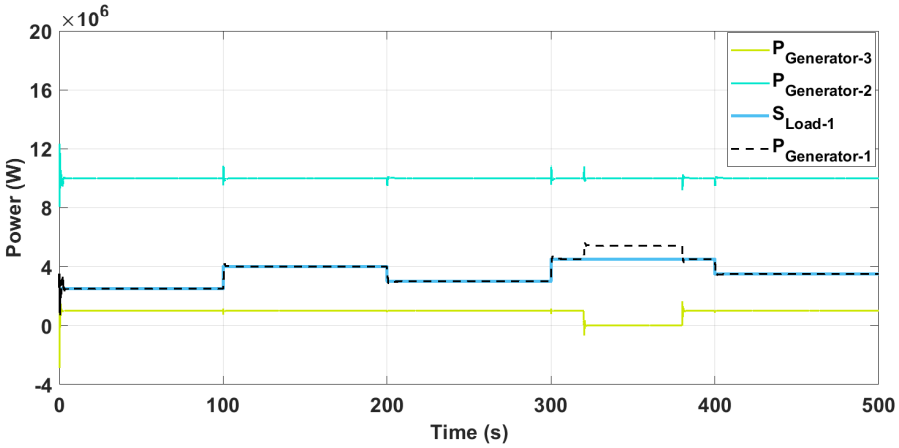

Figure 4.23: power output of generator-1, generator-2, generator-3, and load-1 demand with extended hydraulic accumulator.

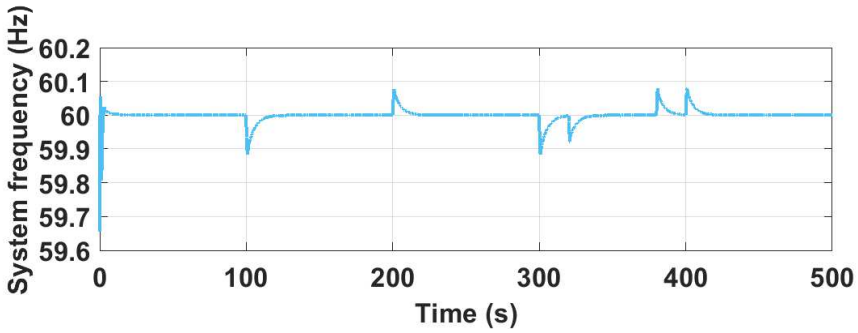

Figure 4.24: System frequency response in Hz with extended hydraulic accumulator.

4.5 Conclusions

In this chapter, we investigated the feasibility of the grid integration of a converter-free hydrostatic wind turbine (HWT) with frequency support capability. The 'continuously variable gearbox ratio' was realised by hydrostatic transmission (HST) with the proposed control strategy and the generator speed was controlled to stay constant. This HWT was connected to the synchronous generator and then directly to the grid without power converters, just like a conventional thermal plant. In this way, it could provide direct inertia support to the system and participate in the grid frequency regulations. The simulations indicated that the proposed coordinated control scheme provided excellent performances under turbulent wind with variable loads, showing that the HWT is a promising solution for the offshore wind power integration.

Chapter 5

Power Generation Control of a Hydrostatic Wind Turbine Implemented by Model-free Adaptive Control Scheme

It has been shown in Chapter 4 that the HWT provides the possibility to remove the fragile and expensive power converters and gearbox, which reduces the maintenance cost in offshore wind power integration system. In this chapter, we will try to further reduce the maintenance cost by applying the advanced model-free adaptive control (MFAC) to achieve better performances in terms of tracking and disturbance rejection in power generations. This aims to extend the fatigue life and improve the operation efficiency.

First an MFAC torque controller is designed to regulate the pump torque in HWT. Then an MFAC pitch controller is designed to regulate the wind turbine blade pitch angles, aiming to stabilise the rotor speed of HWT. The performance of the MFAC torque controller is compared to that of the $\mathcal{H}_\infty$ loopshaping torque controller designed in Section 4.3.2, and the performance of MFAC pitch controller is compared to the gain-scheduling PI pitch controller designed in [77] and the gain-scheduling PI pitch controller with anti-windup designed in [144]. The simulation results indicate that the MFAC torque and pitch controller provide better tracking and disturbance rejection performances, which enhances the power quality and reduces the fatigue loads. All these results imply that MFAC is a promising algorithms for power generation control of the HWT. These results have been drafted to a paper [84].

5.1 Introduction

Generally, the power generation control for conventional wind turbine includes the torque control and pitch control, which is divided into 4 operation regions. When wind speed is above the cut-in speed and below rated speed (i.e. the wind turbine rotor start operating with speed lower than its rating), the wind turbine operates in region 2 to optimise the power capture. Then, if the wind speed is above the rated speed and below cut-out speed (i.e. the wind turbine rotor speed reaches its rating), the wind turbine operates in region 3 and the power extraction should be maintained at its rating. When wind turbine operates in region 1 (below cut-in speed) and region 4 (above cut-out speed), no power will be generated [69, 71]. Similar to the conventional wind turbine, we are only interested in regions 2 and 3 for the torque and pitch control of the HWT.

Firstly, we summarise some of the existing torque control schemes for HWT here. In [37], the displacement of the motor was controlled by a PI controller to track the command of pressure difference across the pump, which is computed from the command of pump torque. However, the PI controller did not provide good tracking performance under turbulent wind. In [118], the PI/PID controller was applied to adjust the displacement of motor, aiming to minimise the torque tracking error like [37] (denoted as $K\omega^2$ law in [118]) or directly optimise the tip-speed ratio (denoted as $DTSRT$ law in [118]). The comparisons are made between these two control schemes, and the effect of the feed-forward schemes are discussed for both control laws. The results indicate that the $K\omega^2$ law performs better than the $DTSRT$ law and that the feed-forward scheme did not provides a distinct advantage under real wind conditions. In [151], model predictive control (MPC) was applied to track the optimal tip-speed ratio, however, it only provided good tracking performance in a limited range of wind speed due to the selection of operating point for plant linearisation. In [144], a $\mathcal{H}_\infty$ loopshaping controller was applied to regulate the motor displacement (similar to Section 4.3.2 where pump displacement is adjusted), which provided outstanding performance. Again, it required the plant linearisation at a certain operating point. Moreover, it is a high-order controller which may not be easily-implemented in industries. In [126], support vector regression (SVR), a model-free control law, was proposed for the HWT torque control. It was applied to predict the optimal reaction torque of the HWT, so that the maximum-power-point-tracking (MPPT) operation could be achieved. However, it is a statistical learning algorithm which requires a large amount of data for training.

Then we listed some of the researches in terms of the pitch control schemes for HWT. A standard PI pitch controller was designed with anti-windup to cancel the neg-

ative angle brought by the integrator in [37]. A pure gain-scheduling integral controller (denoted as I-controller) was proposed to directly regulate the aerodynamic power, in which the pitch angle served as the scheduling parameters [130]. The gain-scheduling PI controller was utilised to stabilise the wind turbine rotor speed with pitch angle employed as the scheduling parameter [77]. Besides, the anti-windup scheme was added to the gain-scheduling PI pitch controller for HWT pitch control [144, 159]. A LPV pitch controller was proposed based on the LIDAR wind preview [144] and it was compared with the gain-scheduling PI controller designed in [77]. The results showed that the LPV with anti-windup provides much better performance than the gain-scheduling PI controller in both rotor speed stabilisation and tower vibration reduction [144]. However, all of these controllers are designed based on the single-DOF linearised models without considering the interaction with other dynamics such as the tower vibration or blade flap oscillations, which may affect control performances in realistic scenarios.

In this chapter, we will employ the model-free adaptive control (MFAC) method to realise torque control and pitch control for the HWT, in order to overcome the disadvantages of the above controllers and improve the control performance. The MFAC is a novel dynamic linearisation method based on real-time system input and output measurement data without the need to establish a mathematical model of the system plant, which improves the robustness to modeling errors caused by the selection of operation points. Besides, it is an easily-applicable control scheme, with low computational burden and strong robustness [57]. The application of MFAC controller in power control systems has already been investigated in some literature, such as the applications of the power control system stabilizer [88], AC/DC microgrid [165], and wind turbine load control [89]. In this chapter, we will apply the MFAC controller to both torque control and pitch control for the HWT. The simulation results indicate that the MFAC controllers can provide much better performance than the $\mathcal{H}_\infty$ torque controller in Section 4.3.2 and the gain-scheduling pitch controller in [77] and [144], which proves to be a promising algorithm for the HWT power generation control.

This chapter is structured as follows: in Section 5.2, we briefly introduce the system structures with its mathematical models. Note that the modeling only used for providing the input and output data without participating the MFAC controller design. In Section 5.3, we expatiate the MFAC algorithms and the design procedure. In Section 5.4, we conduct the simulations and compare the performances of MFAC controller to some of the existing controllers. Finally, Section 5.5 concludes this chapter.

5.2 System modelling for I/O data generation

Different from the HWT system model explained in section 4.2 (Fig. 4.1), in this chapter, we simplify the HST drivetrain to focus only on the power generation control. Note that the model explained in this section is only used for providing the input and output data, which is not applied for the MFAC controller design. As shown in Fig. 5.1, the simplified HST drivetrain configuration is composed of a variable displacement pump and a fixed displacement motor, with a close-loop oil line in-between. The HWT simulation model is constructed based on the NREL 5-MW monopile gearbox-equipped wind turbine.

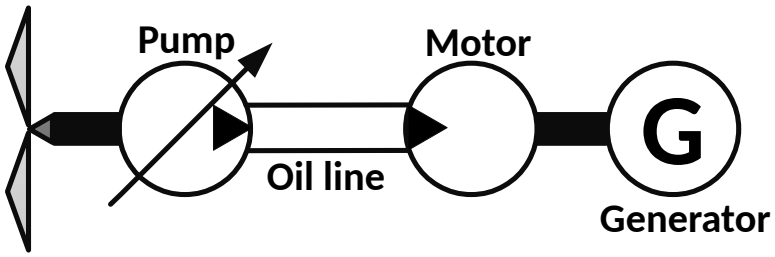

Figure 5.1: Simplified HST drivetrain configuration in a 5-MW HWT with their connections.

Equation (4.1) – (4.7) describe the mathematical model of the HST in Fig. 5.1, and the dynamics of the wind turbine rotor shaft are described as (4.8). The pitch actuator is modelled as

$$\dot{\beta} = \frac{1}{T_\beta} \cdot (\beta^* - \beta), \tag{5.1}$$

where β^* and β are the command and actual blade pitch angles in degree respectively, and T_β is the time constant. The power captured by wind turbine can be expressed as [69]

$$P = \frac{1}{2}\rho_{air}\pi R^2 v_{wind}^3 C_p(\lambda, \beta), \tag{5.2}$$

where ρ_{air} is the air density, R is the blade length and v_{wind} is the wind speed. C_p is the power coefficient, which is a function of tip-speed-ratio λ and pitch angle β. The tip-speed ratio is defined as

$$\lambda = \frac{\omega_r R}{v_{wind}}. \tag{5.3}$$

Thence according to (4.8), (5.2) and (5.3), by properly controlling the pump torque τ_{pump} and pitch angle β, we are able to capture the desired amount of power from wind.

5.3 Control algorithms

In this section, we firstly expatiate the general theory of the model-free adaptive control (MFAC) scheme for a discrete-time single-input-single-output (SISO) nonlinear systems [57, 60, 58, 59], and then we explain its control design procedure and control structure applied for both pump torque control and pitch control in the HWT system.

The discrete-time SISO nonlinear system is written as

$$y(k+1) = f(y(k), ..., y(k-n_y), u(k), ..., u(k-n_u)), \tag{5.4}$$

where $y(\cdot)$ is the system output signal and $u(\cdot)$ is the system input signals. n_y and n_u are the orders for system output and input respectively, and $f(\cdots)$ represents the nonlinear system plant.

Assumption 1 [59]: The partial derivatives of $f(\cdots)$ with respect to the variables $u(k), ..., u(k-L+1)$ are continuous, where L is the linearisation length constant (LLC) for the discrete-time nonlinear system.

Assumption 2 [59]: The system (5.4) is generalised Lipschitz, that is

$$\left|\Delta y(k+1)\right| \leq b \left\|\Delta \boldsymbol{U}_L(k)\right\|,$$

in which b is a positive constant,

$$\Delta \boldsymbol{U}_L(k) = \boldsymbol{U}_L(k) - \boldsymbol{U}_L(k-1),$$

$$\Delta y(k) = y(k) - y(k-1),$$

and

$$\boldsymbol{U}_L(k) = [u(k), ..., u(k-L+1)]^T.$$

The first assumption explicates the condition for the control design of a nonlinear system, and the second one introduces an upper bound for the system output changing rate. We select the partial form dynamic linearisation (PFDL) model [59] to design a MFAC controller. Based on these two assumptions (*Assumption 1* and *2*), the PFDL model of the SISO nonlinear system can be defined (see Theorem 1 below).

Theorem 1 [59]: There must exist a time-varying parameter vector $\boldsymbol{\phi}_L(k)$ for a nonlinear system (5.4) which satisfies the *Assumption 1* and *Assumption 2*, with $\boldsymbol{U}_L(k) \neq 0$ for all k, such that the system (5.4) can be written as the following equivalent PFDL

description:

$$\Delta y(k+1) = \boldsymbol{\phi}_L^T(k)\Delta \boldsymbol{U}_L(k), \tag{5.5}$$

where the vector $\boldsymbol{\phi}_L(k) = [\phi_1(k), ..., \phi_L(k)]^T$ is bounded at any time k. See [57, 59] for the proof of this theorem.

The parameter vector $\boldsymbol{\phi}_L(k)$ in Theorem 1 is called the pseudo gradient (PG) vector. From Theorem 1, it is clear that through estimating this time-varying PG vector, we are able to establish an equivalent linearised model (PFDL model) for the SISO nonlinear system (5.4). Then, the procedures to estimate the PG vector are explained below.

Firstly, the index function for the PG estimation is defined as

$$\begin{aligned} J(\hat{\boldsymbol{\phi}}_L(k)) = &\left| y(k) - y(k-1) - \hat{\boldsymbol{\phi}}_L^T(k)\Delta \boldsymbol{U}_L(k-1) \right|^2 \\ &+ \mu \left\| \hat{\boldsymbol{\phi}}_L(k) - \hat{\boldsymbol{\phi}}_L(k-1) \right\|^2, \end{aligned} \tag{5.6}$$

in which μ is a weighting factor and $\mu > 0$. $\hat{\boldsymbol{\phi}}_L(k)$ denotes the estimation of PG vector $\boldsymbol{\phi}_L(k)$ at time k. We can estimate the PG vector through optimising the index function by setting

$$\frac{\partial J(\boldsymbol{\phi}_L(k))}{\partial \boldsymbol{\phi}_L(k)} = 0. \tag{5.7}$$

That is, combining (5.5), (5.6) and (5.7), the PG estimation can be written as

$$\begin{aligned} \hat{\boldsymbol{\phi}}_L(k) = \hat{\boldsymbol{\phi}}_L(k-1) &+ \eta \Delta \boldsymbol{U}_L(k-1) \\ &\cdot \frac{y(k) - y(k-1) - \hat{\boldsymbol{\phi}}_L^T(k-1)\Delta \boldsymbol{U}_L(k-1)}{\mu + \left\| \Delta \boldsymbol{U}_L(k-1) \right\|^2}, \end{aligned} \tag{5.8}$$

where η is the step-size constant and $\eta \in (0, 2)$.

The procedure to design the control law is similar to the PG estimation. The index function for the control input is selected to be

$$J(u(k)) = \left| y^*(k+1) - y(k+1) \right|^2 + \lambda \left| u(k) - u(k-1) \right|^2, \tag{5.9}$$

where $y^*(\cdot)$ is the desired reference signal. λ is the weighting constant and $\lambda > 0$. We set

$$\frac{\partial J(u(k))}{\partial u(k)} = 0 \tag{5.10}$$

to find out the optimal control law $u(k)$. By considering (5.5), (5.9) and (5.10), we have

$$\begin{aligned} u(k) = u(k-1) &+ \frac{\rho_1 \phi_1(k)(y^*(k+1) - y(k))}{\lambda + \left|\phi_1(k)\right|^2} \\ &- \frac{\phi_1(k) \sum_{i=2}^{L} \rho_i \phi_i(k) \Delta u(k-i+1)}{\lambda + \left|\phi_1(k)\right|^2} \end{aligned} \tag{5.11}$$

where $i = 1, ..., L$, and $\rho_i \in (0, 1]$ is a step-size vector to make (5.11) more general.

Then considering (5.8) and (5.11), the MAFC scheme can be summarised [59] as follows:

$$\begin{aligned} \hat{\boldsymbol{\phi}}_L(k) = \hat{\boldsymbol{\phi}}_L(k-1) &+ \eta \Delta \boldsymbol{U}_L(k-1) \\ &\cdot \frac{y(k) - y(k-1) - \hat{\boldsymbol{\phi}}_L^T(k-1) \Delta \boldsymbol{U}_L(k-1)}{\mu + \left\|\Delta \boldsymbol{U}_L(k-1)\right\|^2}, \end{aligned} \tag{5.12}$$

$$\hat{\boldsymbol{\phi}}_L(k) = \hat{\boldsymbol{\phi}}_L(1), \text{if} \begin{cases} \left\|\hat{\boldsymbol{\phi}}_L(k)\right\| \leq \epsilon, & \text{or} \\ \text{sign}(\hat{\phi}_1(k)) \neq \text{sign}(\hat{\phi}_1(1)), & \text{or} \\ \left\|\Delta \boldsymbol{U}_L(k-1)\right\| \leq \epsilon, \end{cases} \tag{5.13}$$

and

$$\begin{aligned} u(k) = u(k-1) &+ \frac{\rho_1 \hat{\phi}_1(k)(y^*(k+1) - y(k))}{\lambda + \left|\hat{\phi}_1(k)\right|^2} \\ &- \frac{\hat{\phi}_1(k) \sum_{i=2}^{L} \rho_i \hat{\phi}_i(k) \Delta u(k-i+1)}{\lambda + \left|\hat{\phi}_1(k)\right|^2}, \end{aligned} \tag{5.14}$$

where $\mu > 0$, $\lambda > 0$, $\eta \in (0, 2)$. ϵ is a small positive constant and $\hat{\boldsymbol{\phi}}_L(1)$ is the initial of $\hat{\boldsymbol{\phi}}_L(k)$. The reset mechanism (5.13) is added for a strong tracking capability for the time-varying parameter. From (5.12) – (5.14), it is clear that the control law $u(k)$ only depends on the system input and output measurements, which implies model free.

Considering the stability analysis of the MFAC scheme, we have Theorem 2 which is deducted based on *Assumption 3*. Its proof is detailed in [59].

Assumption 3 [59]: The sign of the first element in PG vector $\boldsymbol{\phi}_L(k)$ is assumed to be unchanged for all k with $\left\|\Delta \boldsymbol{U}_L(k)\right\| \neq 0$. That is, $\phi_1(k) > \epsilon > 0$ (or $\phi_1(k) < -\epsilon < 0$), where ϵ is a small positive constant.

Theorem 2 [59]: If the nonlinear system (5.4) satisfies the *Assumption 1, 2, 3* and it is controlled by the MFAC algorithm (5.12) – (5.14), there exists a constant $\lambda_{min} > 0$, such

that for any $\lambda > \lambda_{min}$, the system output tracking error converges to zero asymptotically, and system $y(k)$ and $u(k)$ are bounded for all k, which indicates close-loop system BIBO stable.

Based on the MFAC scheme (5.12) –(5.14), the characteristics of the HWT system including the effect of tower vibration, blade flap oscillations, and turbulent wind, etc., are all integrated into the estimated pseudo gradient (PG). Since Theorem 2 indicates a monotonic change between system output and control input, extra damping terms are required for adjustment of the closed-loop system dynamics to meet the performance specifications in the desired control bandwidth of the HWT power generation system. Besides, the step-size vector $\boldsymbol{\rho}$ serves as the proportional gain of the closed-loop system (see (5.14)), where larger step-size vector contributes to the faster dynamic response. However, without damping effect, increasing proportional gain may lead to the undesirable overshoot, oscillations or even unstable dynamics. Hence, to have a good dynamic response in the desired control bandwidth, it is of great significance to have the extra damping term. Hence, we cascade the MFAC scheme mentioned above (Equation (5.12) – (5.14)) with a proportional term (P_{DD} in Fig. 5.2) to improve the dynamic response of the system. The proportional term P_{DD} serves as a damping gain which suppresses the oscillations in the system output y. The newly established MFAC controller (see Fig. 5.2) is able to provide good dynamic performance without sacrificing the rising time. Note that the damping gain P_{DD} should be properly selected to ensure the system from u^* to y satisfies *Assumption 1* and *Assumption 2*. In the following context, this cascading control scheme is referred as 'MFAC controller' as shown in Fig. 5.2.

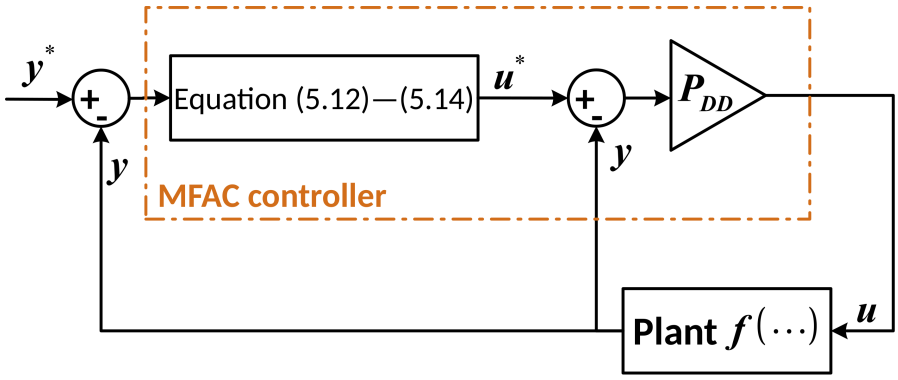

Figure 5.2: MFAC scheme block diagram. Note that in the following of this chapter, 'MFAC controller' is referred to the control scheme in this figure, which includes the MFAC scheme (5.12) – (5.14) together with a constant damping gain P_{DD}.

5.4 Simulation studies

In this section, we utilise the MFAC algorithm to design the torque controller and pitch controller of the HWT system. The system parameters are shown in Table 5.1. The MFAC torque controller is to minimise the tracking error between the pump torque command τ^*_{pump} and pump torque τ_{pump} via regulating the pump volumetric displacement command D^*_p. The performance of MFAC torque controller is compared to the $\mathcal{H}_\infty$ loopshaping torque controller designed in Section 4.3.2. See Fig. 5.3 for the block diagram of the torque control scheme. Then, a MFAC pitch controller is designed to stabilise the wind turbine rotor speed ω_r at its rating in region 3. It is implemented through regulating the blade pitch angle command β^*. Note that the pitch angle is forced to 0° in region 2. We compare the performance of the MFAC pitch controller with the gain-scheduling PI controller in [77] and the gain scheduling PI controller with anti-windup (PIAW) in [144]. See Fig. 5.4 for the block diagram of pitch control scheme. The block diagram of the gain-scheduling PI controller and PIAW controller are shown in Fig. 5.5. The selection of the gain-scheduling PI parameters (K_{pgs} and K_{igs}) and anti-windup coefficient (K_{aw}) follows [77] and [144]:

$$K_{pgs} = -\frac{1.6167}{1+\frac{\beta}{6.302336}}, \quad K_{igs} = -\frac{0.6929}{1+\frac{\beta}{6.302336}}, \quad K_{aw} = 0.5.$$

The control parameters for the MFAC torque and pitch controllers are listed in Table 5.2. Note that the grid frequency is set to be 60 Hz due to the default setting of the NREL wind turbine model.

Table 5.1: Parameters for HWT system [77].

Symbol	**Value**	**Unit**	**Symbol**	**Value**	**Unit**
C_{sp}	7.1×10^{-11}	$m^3/(s{\cdot}Pa)$	C_{fp}	0.02	-
C_{sm}	7.0×10^{-11}	$m^3/(s{\cdot}Pa)$	C_{fm}	0.02	-
D_m	4.1609×10^{-4}	m^3/rad	B_p	50000	Nms
J_r	38759236	kgm^2	B_m	2.5	Nms
J_p	3680	kgm^2	T_p	0.1	sec
ω_g	60	Hz	T_β	0.5	sec
ρ_{air}	1.225	kg/m^3	R	61.5	m

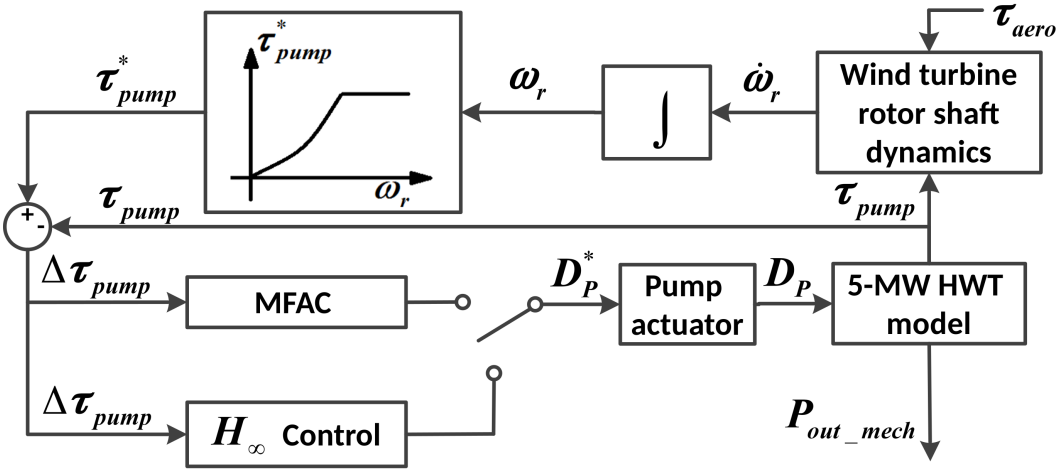

Figure 5.3: Torque control scheme.

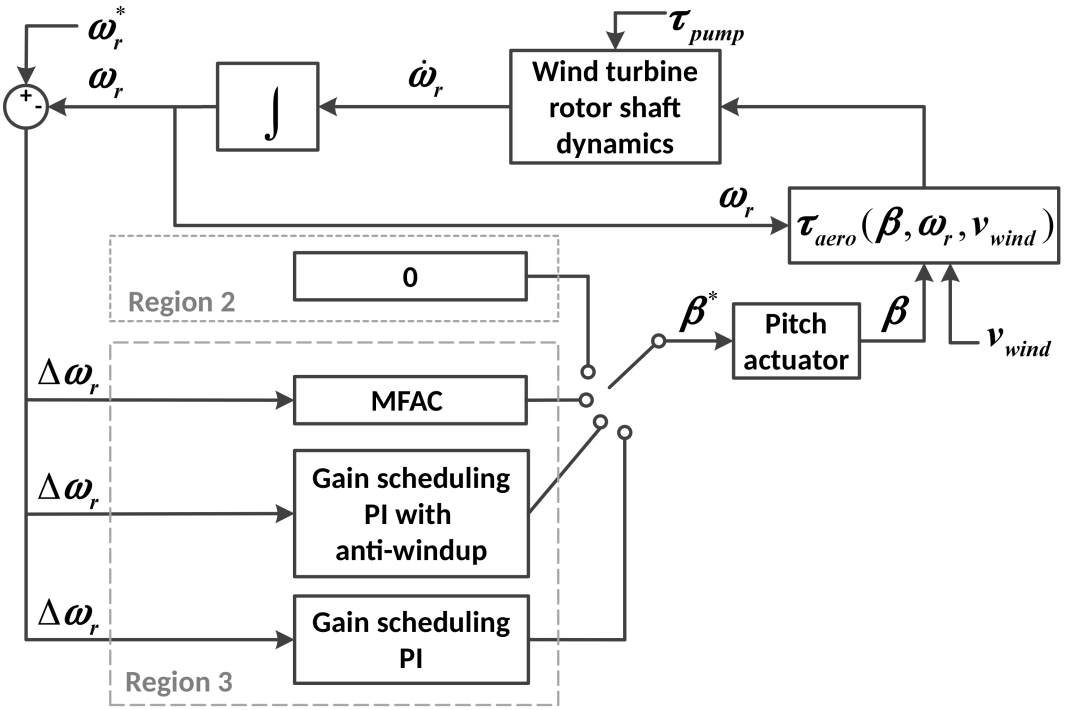

Figure 5.4: Pitch control scheme.

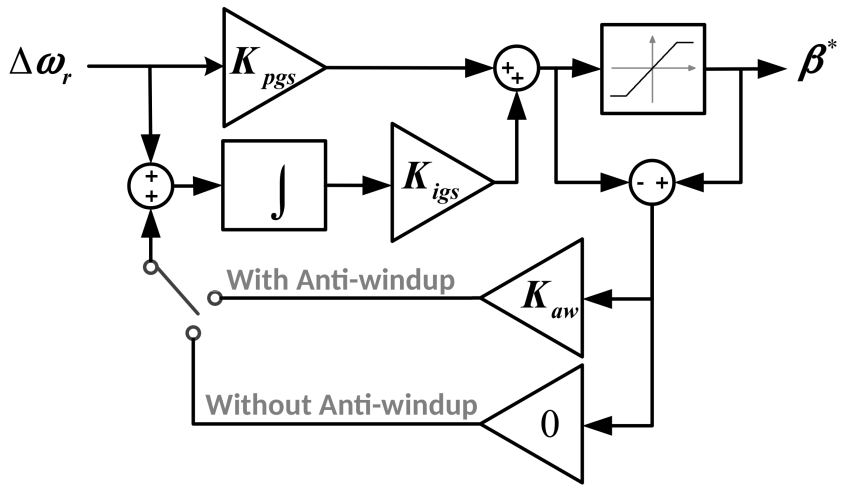

Figure 5.5: Control block diagram of gain-scheduling PI controller and gain-scheduling PI controller with anti-windup (PIAW).

Table 5.2: parameters for MFAC pump torque controller and MFAC blade pitch controller.

	Symbol	**Value**	**Symbol**	**Value**
Pump torque control	λ	6.6×10^{13}	$\rho_{1,2,3}$	0.8424
	$\boldsymbol{\phi}_L(1)$	$[10^7\ 10^7\ 10^7]^T$	η	1
	μ	1	P_{DD}	15
Blade pitch control	λ	0.1	$\rho_{1,2,3}$	1.3867×10^{-5}
	$\boldsymbol{\phi}_L(1)$	$[0.13\ 0.13\ 0.13]^T$	η	1
	μ	1	P_{DD}	-60

The simulations are conducted for 300 seconds under turbulent wind with mean speeds of 8 m/s, 11.4 m/s (rated speed) and 18 m/s respectively. The International Electro-technical Commission (IEC) Kaimal spectral NTM (normal turbulence model) [24, 25] in NREL Turbsim [70] is utilised to generate stochastic, full-field, and turbulent wind flows, with most turbulent characteristics (category A). See Fig. 5.6 for the these turbulent wind inputs.

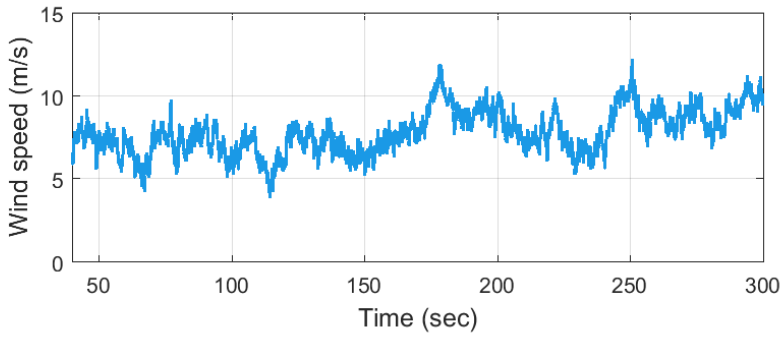

(**a**)Mean wind speed 8 m/s

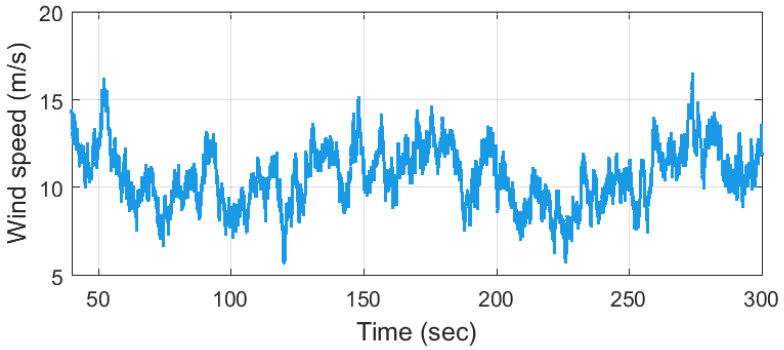

(**b**)Mean wind speed 11.4 m/s

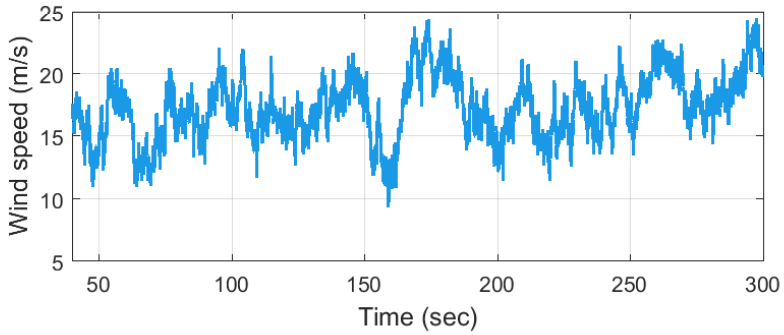

(**c**)Mean wind speed 18 m/s

Figure 5.6: Turbulent wind inputs generated by NREL Turbsim with different mean wind speeds.

5.4.1 Torque control performances

Generally, the pump torque command τ^*_{pump} in region 2 is proportional to the square of the wind turbine rotor speed ω_r, which instructs the wind turbine to maintain the optimal tip-speed ratio, realising MPPT operation [71]. It means that the optimal tip-speed ratio is achieved based on accurate regulation of pump torque, and the accuracy of the regulation will directly influences the amount of power captured from the wind. When wind turbine operates in region 3, the power extraction is more relevant to the pitch angle regulation due to its slow dynamic response. However, good torque control in region 3 can be used to minimise the oscillation in pump torque, which increase the life expectancy of HWT and reduce the maintenance cost. The performance of MFAC torque controller and the pre-proposed $\mathcal{H}_\infty$ torque control (see Section 4.3.2) are compared through the root-mean-square (RMS) value of the tracking error:

$$\mathrm{RMS}_\tau = \sqrt{\frac{1}{300}\int_0^{300}(\tau^*_{pump} - \tau_{pump})^2 dt}. \tag{5.15}$$

We run the torque control simulations under 3 wind inputs displayed in Fig. 5.6. The tracking performances of both the MFAC controller and the $\mathcal{H}_\infty$ controller under 3 different wind inputs are shown in Fig. 5.7, 5.8 and 5.9, respectively. The RMS of tracking error, the average power extraction, and the performance comparisons of two controllers are shown in Table 5.3. Note that we do not provide the power extraction comparison when mean wind speed is 18 m/s, since under this wind input, the wind turbine operates in region 3 and power extraction is more relevant to the pitch control.

From Fig. 5.7 – Fig. 5.9, it is clear that MFAC controller shows higher tracking accuracy with less oscillations than the $\mathcal{H}_\infty$ controller. Moreover, the performance of the MFAC controller has no conspicuous differences under different wind speeds, while there is visible degradation in the performance of $\mathcal{H}_\infty$ controller as the mean wind speed rises. It is because the $\mathcal{H}_\infty$ loopshaping controller is designed based on the model which is linearised at wind speed of 9 m/s (see Section 4.3.2). Thence, as the mean wind speed moves away from 9 m/s, the $\mathcal{H}_\infty$ controller inevitably suffers from the performance degradation. However, the MFAC scheme is a model-free algorithm which dynamically estimates the plant merely exploiting the real-time input and output data. Thus, there is no obvious difference in the performance of MFAC controller under different wind inputs. From Table 5.3, it is clear that the RMS_τ of the MFAC controller is much smaller than that of the $\mathcal{H}_\infty$ controller. Besides, more power is captured in region 2 by the MFAC controller than the $\mathcal{H}_\infty$ controller due to its outstanding tracking performance.

In addition, due to the high order of the $\mathcal{H}_\infty$ controller (16 orders here), it is not easily-applicable in industries, thus the MFAC controller potentially provides a better solution.

Table 5.3: Pump torque control performance implemented by the $\mathcal{H}_\infty$ controller and the MFAC controller. For average wind speed of 11.4 m/s and 18 m/s, the pitch controller is implemented by the gain-scheduling PI controller with anti-windup (see [144]). The comparison is calculated according to $\frac{\text{MFAC}-\mathcal{H}_\infty}{\mathcal{H}_\infty}$.

	Wind	$\mathcal{H}_\infty$ **controller**	**MFAC controller**	**Comparison (%)**
RMS_τ (kN·m)	8 m/s	7.0494	5.7104	−18.99
	11.4 m/s	6.1889	3.9770	−35.74
	18 m/s	12.202	2.5719	−78.92
Power (MW)	8 m/s	1.2173	1.2190	+0.14
	11.4 m/s	3.8541	3.8829	+0.75
	18 m/s	4.7141	4.7142	—

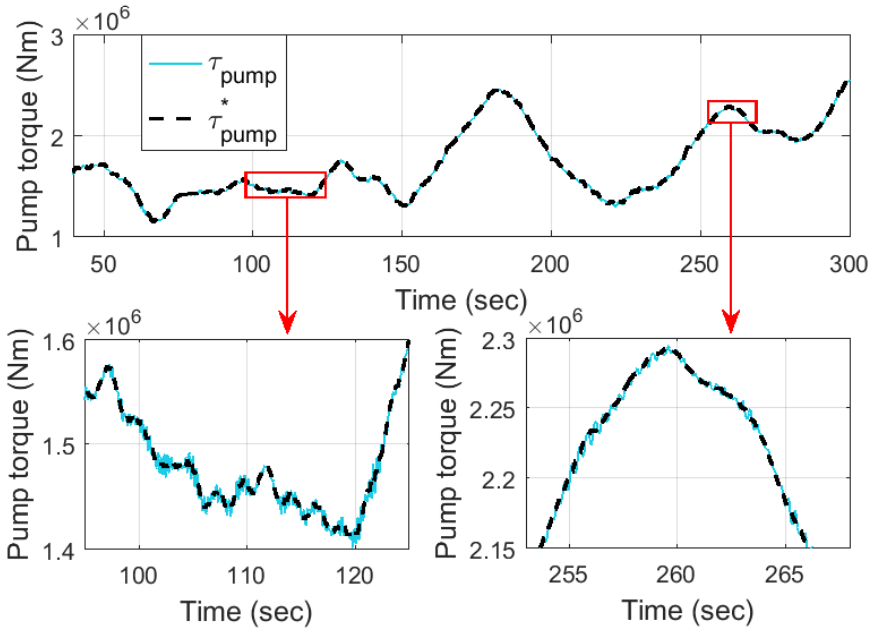

(**a**)MFAC controller

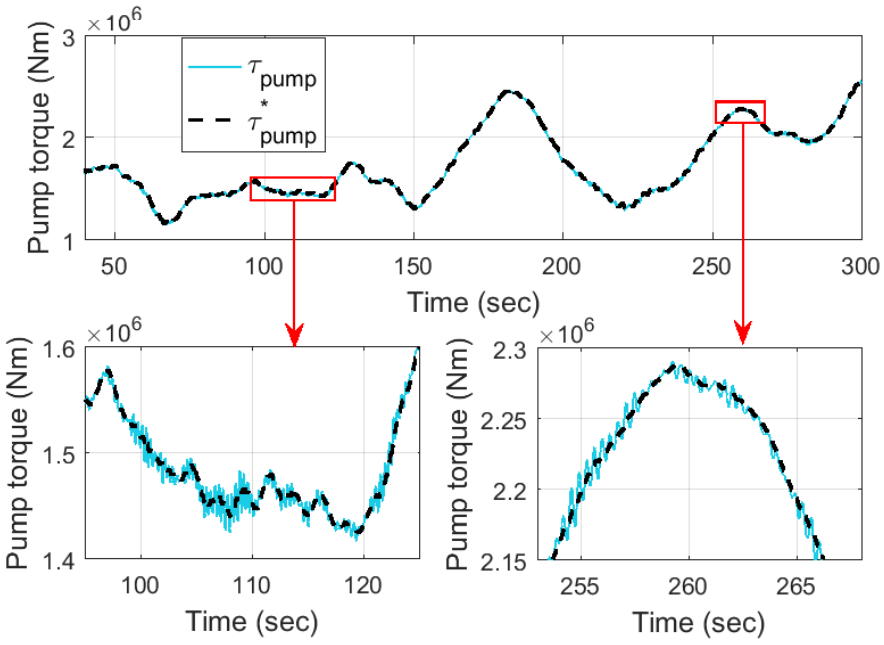

(**b**)$\mathcal{H}_\infty$ controller

Figure 5.7: Pump torque control performance under turbulent wind with mean speed of 8 m/s.

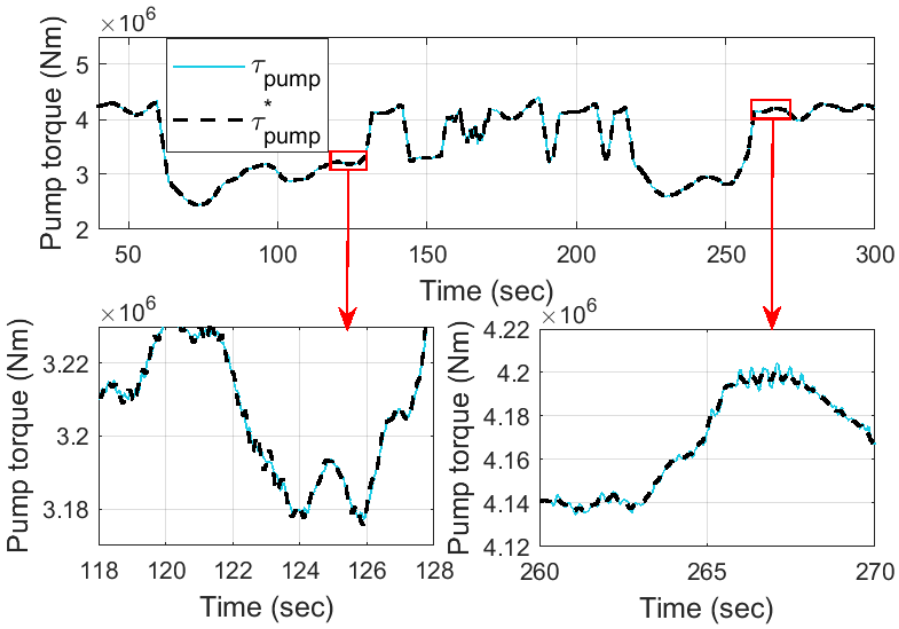

(**a**)MFAC controller

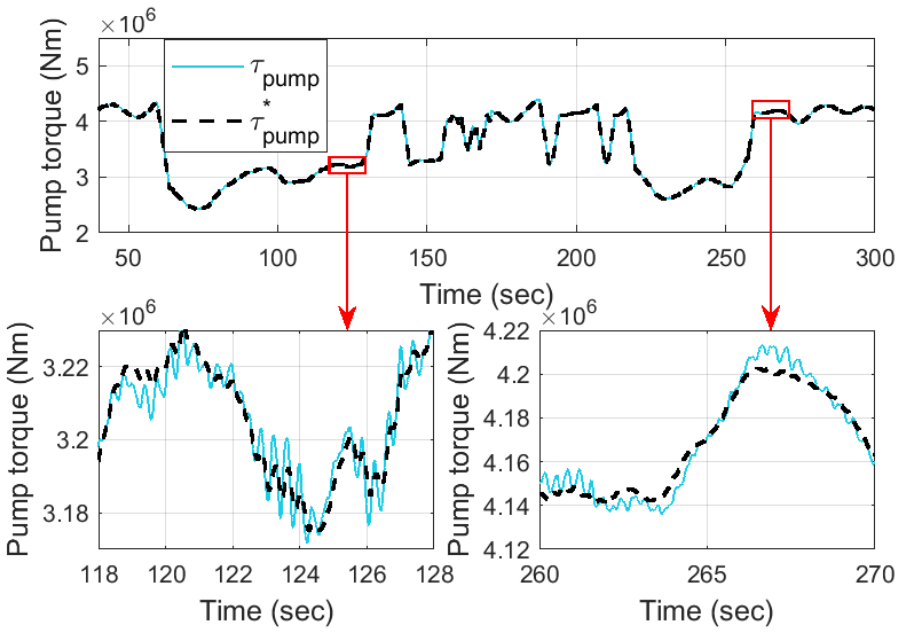

(**b**)$\mathcal{H}_\infty$ controller

Figure 5.8: Pump torque control performance under turbulent wind with mean speed of 11.4 m/s.

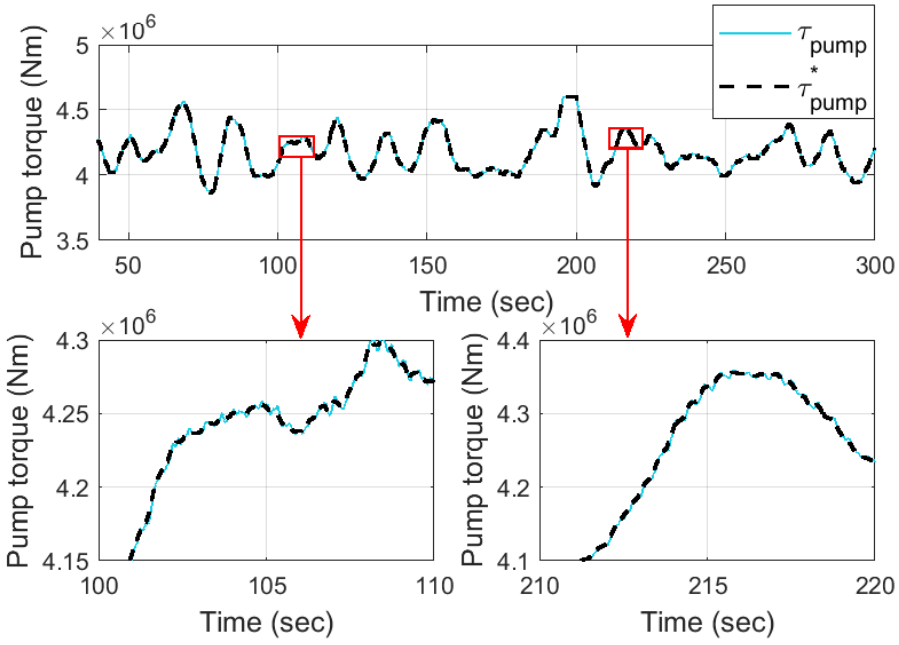

(**a**)MFAC controller

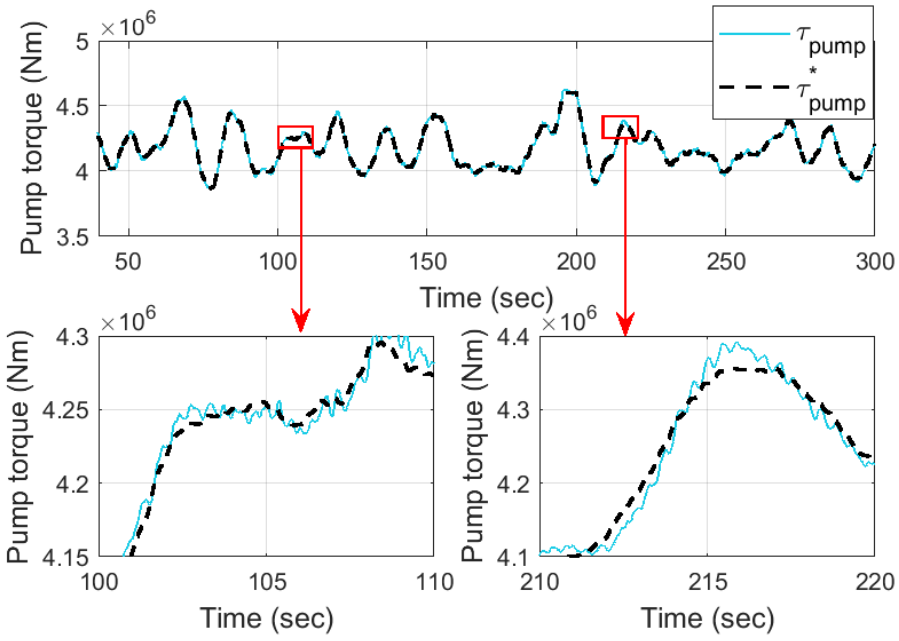

(**b**)$\mathcal{H}_\infty$ controller

Figure 5.9: Pump torque control performance under turbulent wind with mean speed of 18 m/s.

5.4.2 Pitch control performances

As the wind speed rises over 11.4 m/s (rated speed), the wind turbine rotor speed ω_r gradually increases to its rating ω_r^*. During this period, the wind turbine transits its operation region from region 2 to region 3 and the pitch control is enabled to guarantee the steady power extraction, which ends the MPPT operation. A proper control needs to be designed to ensure the smooth transitions with minimal over-speed in ω_r from region 2 to 3 and small variations in ω_r in region 3 regardless of turbulent wind inputs. We also expect the variations in power extraction to be small. Hence, we calculate the root-mean-square value of the wind turbine rotor speed (RMS_{ω_r}) to evaluate the performance by different pitch control schemes:

$$\text{RMS}_{\omega_r} = \sqrt{\frac{1}{300}\int_0^{300} (\omega_r^* - \omega_r)^2 dt}. \tag{5.16}$$

We also estimate the damage-equivalent load (DEL) under different pitch control schemes. The DEL is estimated by the NREL MLife code based on the tower base side-side and fore-aft moment [54, 53]. It is a Matlab-based tool to provide load analysis [54, 53]. The details of the estimation theory will be explained in Appendix B.

We firstly run the simulations under mean wind speed of 11.4 m/s. The performances of MFAC controller, gain-scheduling PI controller [77] and gain-scheduling PI controller with anti-windup (PIAW) [144] are displayed in Fig. 5.10. The anti-windup compensation for gain-scheduling PI controller is designed to mitigate the undesirable system response due to the pitch saturation and cancel the undesirable negative angles brought by the integrator [144]. It is clear that every time the wind turbine transit from region 2 to region 3, the MFAC controller provides fastest rotor speed stabilisation performance without significant deviations from its reference. Fig. 5.11 shows the tower base moment (i.e., the moment caused by side-side and fore-aft forces) in kN·m and the tower up deflection relative to the undeflected position in side-side and fore-aft direction in meters under mean wind speed of 11.4 m/s. Taking an overall view of these results, the MFAC controller provides much better performance during the transitions between region 2 and region 3, with less fatigue load exerted on the wind turbine.

Then the simulation is conducted under mean wind speed of 18 m/s. The wind turbine operates only in region 3 with no pitch saturation. That is, the performance of PIAW controller is exactly the same as gain-scheduling PI controller. Hence, the performance comparisons are made only between gain-scheduling PI controller and MFAC controller. See Fig. 5.12 for the responses of pitch angle, rotor speed and power ex-

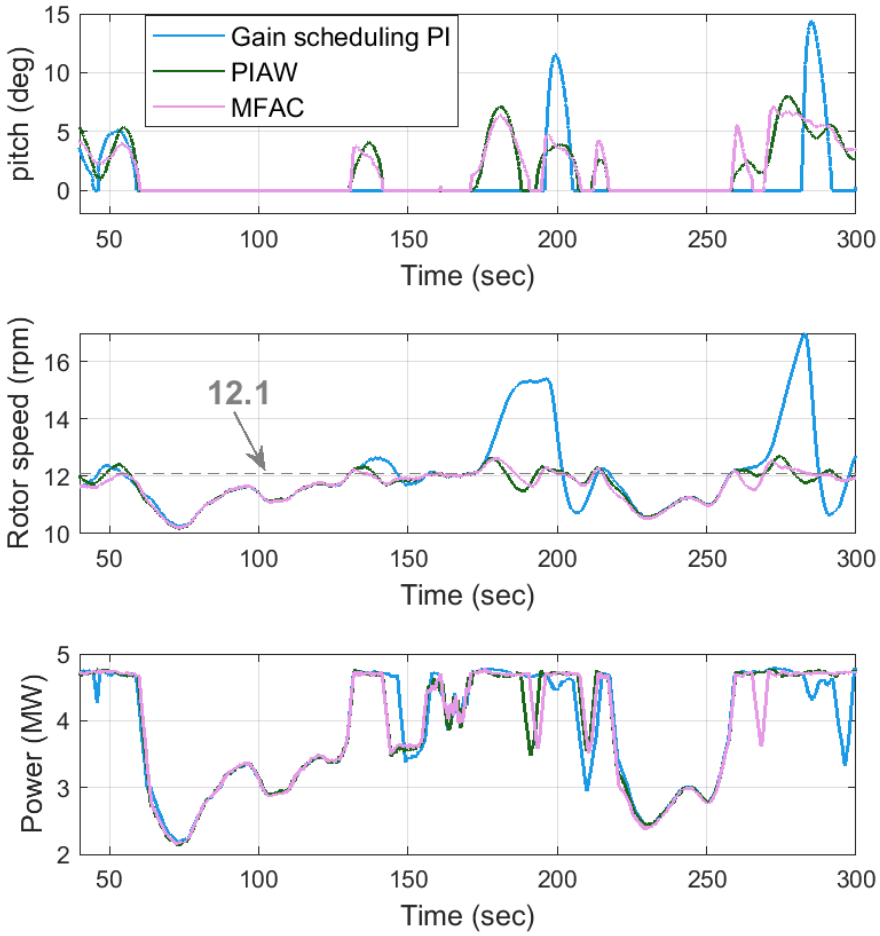

Figure 5.10: Wind turbine blade pitch angle (deg), rotor speed (rpm) and power extraction (MW) under mean wind speed of 11.4 m/s.

tractions under gain-scheduling PI controller and MFAC controller. It is clear that the power extraction by MFAC controller is more steady, and the variation in rotor speed by MFAC controller is much smaller in comparison with the gain-scheduling PI controller, which implies better disturbance rejection performance. Fig. 5.13 shows the tower base moment (i.e., the moment caused by side-side and fore-aft forces) in kN·m and the tower up deflection relative to the undeflected position in side-side and fore-aft direction in meters under mean wind speed of 18 m/s. By taking an overall assessment of these

results, the MFAC controller proves to be a better solution for HWT pitch control with more effective rotor speed stabilisation performance and less fatigue loads exerted on the wind turbine.

Table 5.4 shows the rotor speed RMS, power extraction, DELs in side-side direction and DELs in fore-aft direction under the gain-scheduling PI controller, PIAW controller and MFAC controller with mean wind input of 11.4 m/s and 18 m/s. Note that the calculation of the RMS_{ω_r} under mean wind speed of 11.4 m/s only considers the period when wind turbine is in region 3, that is, the period when pitch angle $\beta \neq 0°$. The procedure to estimate the DEL are detailed in Appendix B. The parameters to estimate the DEL are selected to be 20 for the ultimate load factor (ULF) [93], 60 for number of range bins n^R [137], and 1 Hz for the DEL frequency [54]. The definitions for these parameters are explained in Appendix B. From Table 5.4, it is clear that MFAC controller provides much smaller rotor speed variations and more steady power extraction than the gain-scheduling PI controller and PIAW controller, which implies the better disturbance rejection performance. Besides, more power is extracted by MFAC controller which improves the operation efficiency. Moreover, by taking overall consideration of the performance, the total fatigue loads exerted on the wind turbine tower under the MFAC controller is considered to be smaller. That is, the MFAC proves to be a better algorithm to implement HWT pitch control than the gain-scheduling PI controller in [77] and PIAW controller in [144].

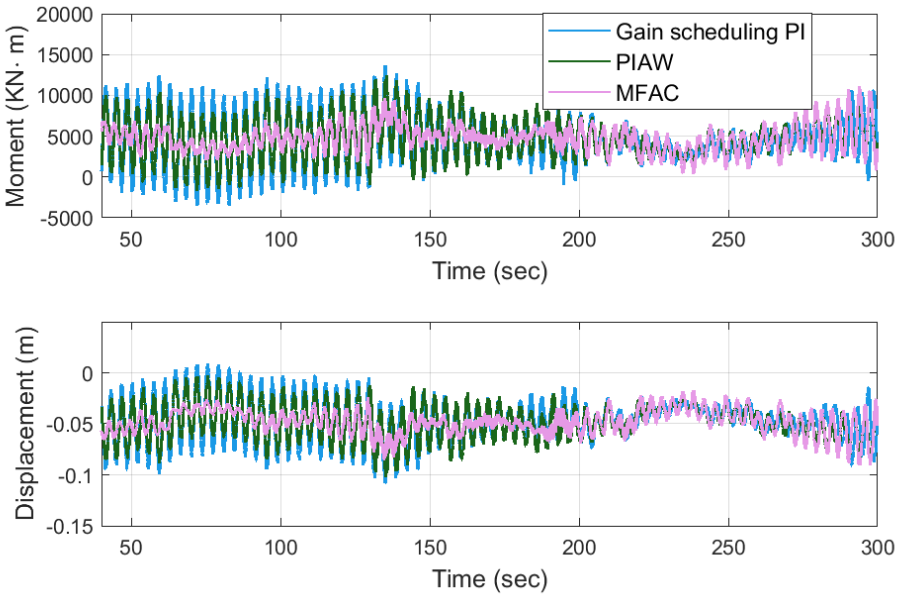

(**a**)Tower base moment and tower top deflection in side-side direction.

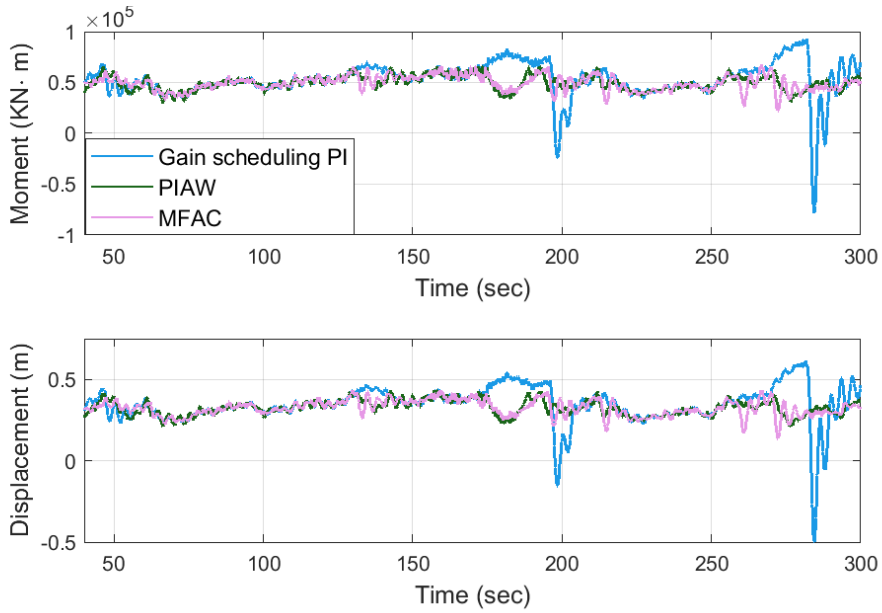

(**b**)Tower base moment and tower top deflection in fore-aft direction.

Figure 5.11: Tower base moment and tower up deflection (relative to the undeflected position) in side-side and fore-aft direction under mean wind speed of 11.4 m/s.

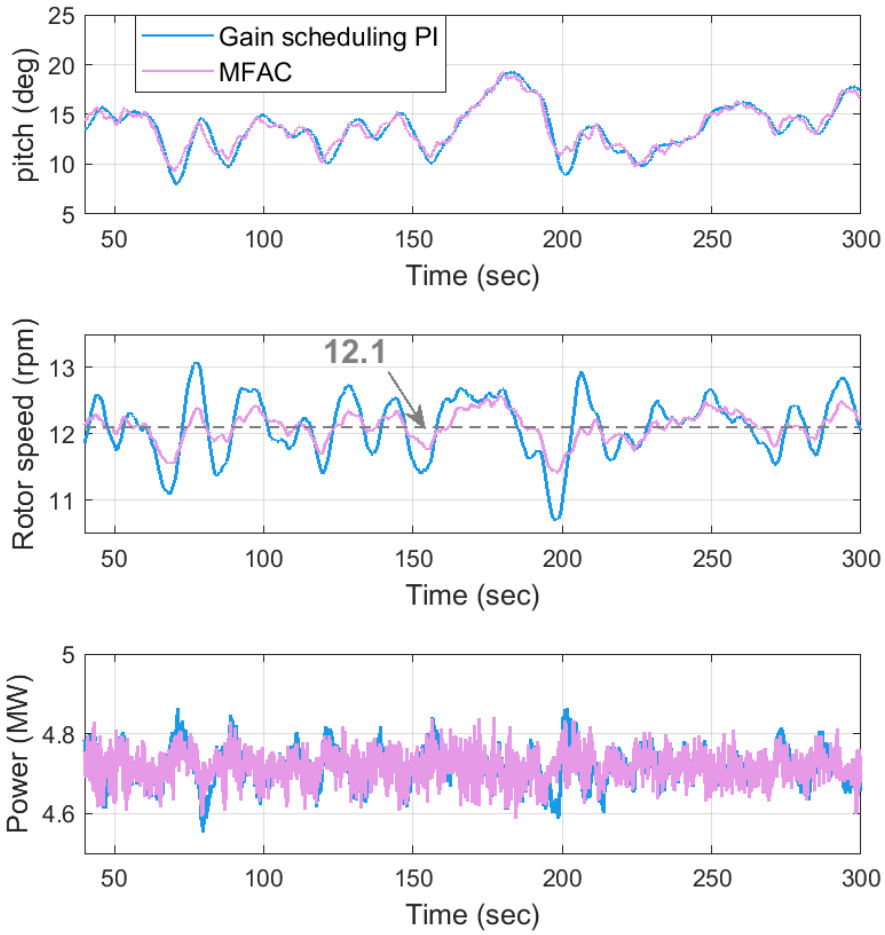

Figure 5.12: Wind turbine blade pitch angle (deg), rotor speed (rpm) and power extraction (MW) under mean wind speed of 18 m/s.

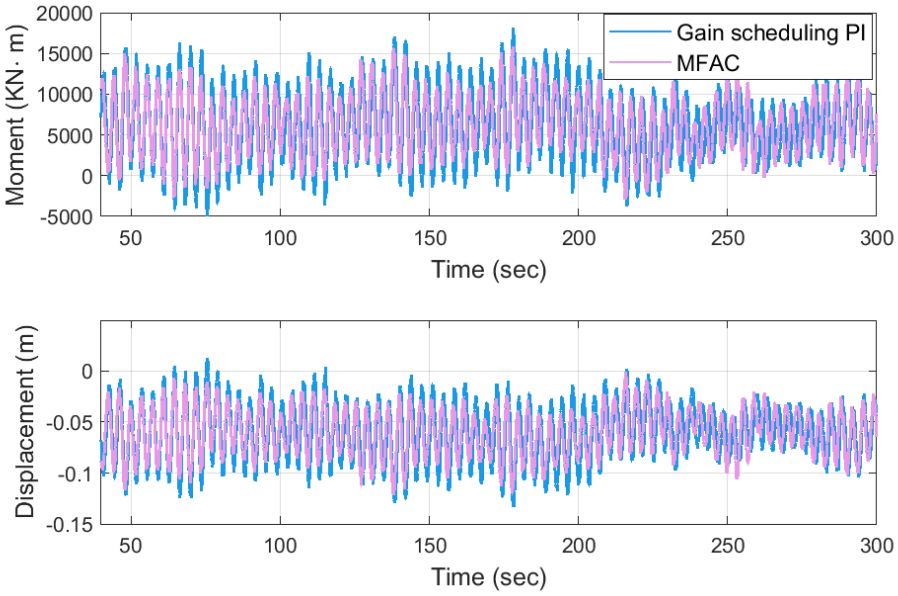

(**a**)Tower base moment and tower top deflection in side-side direction.

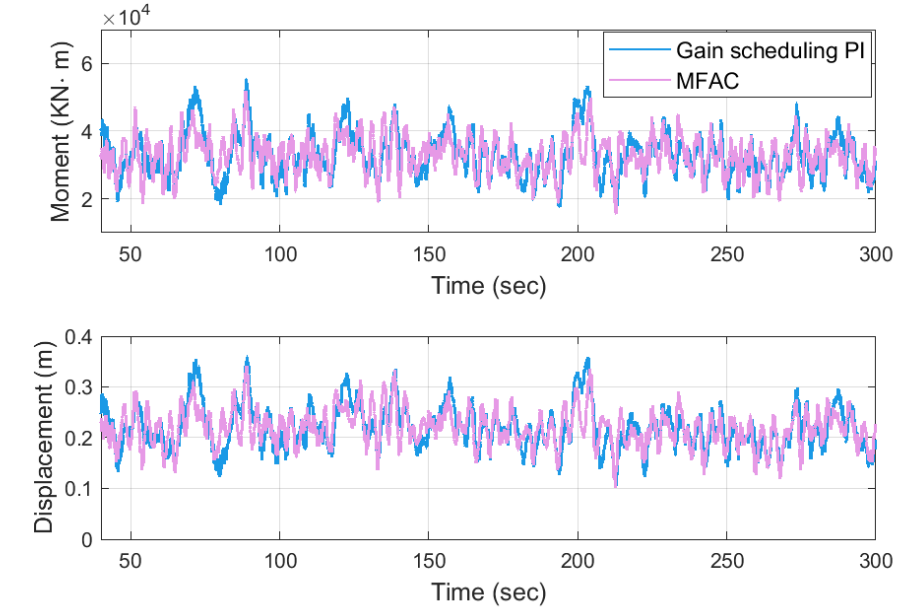

(**b**)Tower base moment and tower top deflection in fore-aft direction.

Figure 5.13: Tower base moment and tower up deflection (relative to the undeflected position) in side-side and fore-aft directions under mean wind speed of 18 m/s.

Table 5.4: Wind turbine blade pitch control performance implemented by the gain-scheduling PI, PIAW and MFAC controller. The pump torque control is implemented by $\mathcal{H}_\infty$ controller explained in Section 4.3.2. The comparison is calculated according to $\frac{\text{MFAC}-\text{PI}}{\text{PI}}$ / $\frac{\text{MFAC}-\text{PIAW}}{\text{PIAW}}$. Note that the performances of PIAW under 18 m/s are exactly the same with that of gain-scheduling PI controller since no pitch saturation occurs.

	Wind (m/s)	**Gain-scheduling PI**	**PIAW**	**MFAC controller**	**Comparison(%) (PIAW/MFAC)**
RMS_{ω_r} (rpm)	11.4	1.5009	0.4495	0.4486	$-70.11/-0.2$
	18	0.4487	—	0.2206	$-50.60/-50.60$
Power (MW)	11.4	3.8446	3.8541	3.8791	$+0.90/+0.65$
	18	4.7141	—	4.7160	$+0.04/+0.04$
DEL(side-side) (MN·m)	11.4	3.34	2.57	1.56	$-53.29/-39.30$
	18	4.64	—	3.60	$-22.41/-22.41$
DEL(fore-aft) (MN·m)	11.4	14.40	4.76	5.58	$-61.25/+17.23$
	18	5.73	—	5.66	$-1.220/-1.220$
DEL(total) (MN·m)	11.4	17.74	7.33	7.14	$-59.75/-2.59$
	18	10.37	—	9.26	$-10.70/-10.70$

5.5 Conclusions

In this chapter, the model-free adaptive control (MFAC) scheme was used for the power generation control of a monopile offshore hydrostatic wind turbine (HWT). It was designed for both pump torque control and the blade pitch control. In simulation studies, the MFAC torque controller was compared with the $\mathcal{H}_\infty$ loopshaping torque controller designed in Section 4.3.2. The MFAC pitch controller was compared with the gain-scheduling PI controller developed in [77] and the gain-scheduling PI controller with anti-windup developed in [144]. The results indicated that the MFAC torque controller provided much better tracking performance than the $\mathcal{H}_\infty$ controller with fast response and little oscillations, and that the MFAC pitch controller showed better rotor speed stabilisation capabilities and more smooth transition between operation region 2 and 3 with less fatigue loads acting on the wind turbine tower. All these showed that MFAC is a promising algorithm for the power generation control of the HWT.

Chapter 6

Conclusions and Future Work

This thesis studied the control of the offshore wind turbine and its grid integrations aiming to reduce the maintenance costs by eliminating the fragile and expensive components (e.g. DC-link capacitor, power converters and gearbox) in wind turbines. We considered two types of the wind turbines, namely the conventional gearbox-equipped wind turbine and the hydrostatic wind turbine (HWT). Chapter 2 and 3 investigated the better alternative for the DC-link capacitor in the grid integration of the conventional gearbox-equipped offshore wind turbine. Chapter 4 and 5 considered the grid integration and power generation control of the offshore HWT.

6.1 Conclusions

In Chapter 2, we investigated the possibility of using the virtual infinite capacitor (VIC) as an alternative for the DC-link capacitor. It is actually a power electronics circuits which functions as a large capacitor for low frequency voltage filtering. We designed a control algorithm for the VIC. We also improved the circuit realisation of the VIC in [163] to realise soft switching. Before we applied the VIC to the wind turbines, we verified it in the simple power factor compensator (PFC) circuit as the output filter capacitor through simulations. The simulation results indicated that the VIC provided outstanding voltage filtering performance. Then we experimentally validated it by directly injecting the DC voltage together with a 50 Hz sinusoidal voltage ripple to the VIC for ripple suppressions. The experiment results showed that the ripple could be greatly eliminated and the performances of VIC in experiment are highly consistent with the corresponding simulation results. This chapter demonstrated the possibility to use VIC to substitute the fragile DC-link capacitor in wind power integration system and to use it in other

industrial systems.

The proposed VIC in Chapter 2 mainly filtered the ripple in the one frequency range, but the DC-link voltage usually included ripples in two distinct frequency range which were required to be removed. Then in Chapter 3, we proposed the concept of the parallel virtual infinite capacitor (PVIC) with new snubber circuit designs. It referred to a low-frequency (LF) virtual infinite capacitor (VIC) and a high-frequency (HF) VIC working on a common DC link and sharing one capacitor, in order to suppress the voltage ripples in a wider frequency band than what one VIC could achieve. It was applied to substitute the DC-link capacitor in the grid integration of a DFIG-based offshore wind turbine (WindPACT 1.5-MW wind turbine). The simulations were conducted under different grid conditions with turbulent wind input. The results showed that the PVIC provided outstanding ripple suppression performance regardless of the LF and HF fluctuations, individually or together. In comparison with an equivalent DC-link capacitor, the PVIC reduced the DC-link voltage ripple by about 30% during normal grid operation, and by approximately 85% during the tested grid disturbances. This demonstrated that PVIC has much better performance than the equivalent DC-link capacitor.

The proposed PVIC in Chapter 3 removed the bulky, vulnerable and expensive DC-link capacitor between two power converters in the wind power integration system. However, the power converters are also fragile and expensive. Besides, the existence of power converters hinders the direct inertia support from the generator to the grid, which imposes great challenges to the modern power system. Hence, in Chapter 4, we investigated the feasibility of the grid integration of a converter-free offshore hydrostatic wind turbine (HWT) with frequency support capability. The 'continuously variable gearbox ratio' was realised by HST with the proposed control strategy and the generator speed was controlled to stay constant. This HWT was connected to the synchronous generator and then directly to the grid without power converters, just like a conventional thermal plant. In this way, it could provide direct inertia support to the system and participate in the grid frequency regulations. The simulations indicated that the proposed coordinated control scheme provided excellent frequency regulation performances under turbulent wind with variable loads, showing that the HWT is a promising solution for the offshore wind power integration.

The HWT proposed in Chapter 4 removed the fragile power converters and gearbox, which offered the reduced maintenance cost for the offshore wind power system. In Chapter 5, we investigated to further cut down the maintenance cost and improve the system performance by designing the power generation control of HWT with a novel

model-free adaptive control (MFAC) scheme. The MFAC scheme was applied for both the torque control and pitch control. In simulation studies, the performance of the MFAC torque controller was compared to the $\mathcal{H}_\infty$ loopshaping torque controller designed in Section 4.3.2. And the performance of the MFAC pitch control scheme was compared to the gain-scheduling PI controller designed in [77] and gain-scheduling PI controller with anti-windup designed in [144]. The results indicated that the MFAC torque control scheme provided much better tracking performance than $\mathcal{H}_\infty$ controller with fast response and little oscillations. The MFAC pitch control scheme showed better disturbance rejection performance and more smooth transition between operation regions 2 and 3 with less fatigue loads to the wind turbine tower in comparison with gain-scheduling PI controller and gain-scheduling PI controller with anti-windup (PIAW). Hence, MFAC proved to be a promising algorithm for the power generation control of the HWT.

6.2 Future work

Below are the recommendations for future studies:

- A tidal turbine (or several small ones) can be coupled to the existing converter-free HWT structure to form a new generation unit, which fully takes advantages of the HST. The design aims to maintain the state of charge (SoC) of the accumulator in case of wind shortage.
- A few generation units can be centralised via HST to drive one large generator, which can improve the wind energy utilisation efficiency.
- The power generation and grid integration for the floating offshore HWTs can be investigated.

Bibliography

[1] Windstats reports. Technical Report Q1-Q4, 2006, 2009 and 2012.

[2] Windstats report. Technical Report 1, 2013.

[3] Chad Abbey and Gza Joos. Supercapacitor energy storage for wind energy applications. *IEEE Transactions on Industry Applications*, 43(3):769–776, 2007.

[4] Atte Aho, Markus Antonietti, Sebastian Arndt, Malte Behrens, Eckhard Bill, Armin Brandner, Gabriele Centi, Peter Claus, Nicholas Cox, Serena DeBeer, et al. *Chemical energy storage*. Walter de Gruyter, 2013.

[5] Jacob Aho, Lucy Pao, and Paul Fleming. An active power control system for wind turbines capable of primary and secondary frequency control for supporting grid reliability. In *51st AIAA Aerospace Sciences Meeting including the New Horizons Forum and Aerospace Exposition*, pages 1–13, Texas, USA, January 2013.

[6] Vladislav Akhmatov. Variable-speed wind turbines with doubly-fed induction generators part III: Model with the back-to-back converters. *Wind Engineering*, 27 (2):79–91, 2003.

[7] DO Akinyele and RK Rayudu. Review of energy storage technologies for sustainable power networks. *Sustainable Energy Technologies and Assessments*, 8:74–91, 2014.

[8] Hijazi Alaa, Bideaux Eric, Venet Pascal, Clerc Guy, Rojat Gerard, et al. Sliding mode control of boost converter: Application to energy storage system via supercapacitors. In *13th European Conference on Power Electronics and Applications (EPE 2009)*, pages 1–10, Barcelona, Spain, September 2009. IEEE.

[9] Bill Andreycak. Zero voltage switching resonant power conversion. In *UNITRODE Power Supply Design Seminar SEM-700*, 1990.

[10] Mathew Aneke and Meihong Wang. Energy storage technologies and real life applications – A state of the art review. *Applied Energy*, 179:350–377, 2016.

[11] Mostafa Asadollahi, Hassan Dehghani, et al. Excitation control of a synchronous generator using a novel fractional-order controller. *IET Generation, Transmission & Distribution*, 9(15):2255–2260, 2015.

[12] Sara L Batley, David Colbourne, PD Fleming, and Paul Urwin. Citizen versus consumer: challenges in the UK green power market. *Energy policy*, 29(6):479–487, 2001.

[13] Francisco Beltran-Carbajal, Antonio Favela-Contreras, Irvin Lopez-Garcia, Antonio Valderrabano-Gonzalez, Julio Cesar Rosas-Caro, and Victor Manuel Sanchez-Huerta. Output feedback dynamic tracking excitation control of synchronous generators. *IET Generation, Transmission & Distribution*, 10(12):3041–3049, 2016.

[14] Frede Blaabjerg, Remus Teodorescu, Marco Liserre, and Adrian V Timbus. Overview of control and grid synchronization for distributed power generation systems. *IEEE Transactions on industrial electronics*, 53(5):1398–1409, 2006.

[15] Andrew Buckspan, Jacob Aho, Paul Fleming, Yunho Jeong, and Lucy Pao. Combining droop curve concepts with control systems for wind turbine active power control. In *Power Electronics and Machines in Wind Applications (PEMWA)*, pages 1–8, Denver, CO, USA, July 2012. IEEE.

[16] Andrew Burke. Ultracapacitors: why, how, and where is the technology. *Journal of power sources*, 91(1):37–50, 2000.

[17] Tony Burton, Nick Jenkins, David Sharpe, and Ervin Bossanyi. *Wind energy handbook*. John Wiley & Sons, 2011.

[18] Maolin Cai, Yixuan Wang, Zongxia Jiao, and Yan Shi. Review of fluid and control technology of hydraulic wind turbines. *Frontiers of Mechanical Engineering*, 12 (3):312–320, 2017.

[19] Wen Cai, Ling Jiang, Bangyin Liu, Shanxu Duan, and Changyue Zou. A power decoupling method based on four-switch three-port DC/DC/AC converter in DC microgrid. *IEEE Transactions on Industry Applications*, 51(1):336–343, 2015.

[20] Xin Cao, Qing-Chang Zhong, and Wen-Long Ming. Ripple eliminator to smooth DC-bus voltage and reduce the total capacitance required. *IEEE Transactions on Industrial Electronics*, 62(4):2224–2235, 2015.

[21] Daniel Chan and John Mo. Life cycle reliability and maintenance analyses of wind turbines. *Energy Procedia*, 110:328–333, 2017.

[22] Le-Ren Chang-Chien, Chih-Che Sun, and Yu-Ju Yeh. Modeling of wind farm participation in AGC. *IEEE Transactions on Power Systems*, 29(3):1204–1211, 2014.

[23] Minjie Chen, Khurram K Afridi, and David J Perreault. Stacked switched capacitor energy buffer architecture. *IEEE Transactions on Power Electronics*, 28(11):5183–5195, 2013.

[24] International Electrotechnical Commission. Wind turbine generator systems—Part 1: Safety requirements, 2nd ed., iec 61400-1. Technical report, International Electrotechnical Commission, Geneva, Switzerland, 1999.

[25] International Electrotechnical Commission. Wind turbine generator systems—Part 1: Safety requirements, 3rd ed. Technical report, International Electrotechnical Commission, Geneva, Switzerland, 2005.

[26] Brian E Conway. *Electrochemical supercapacitors: scientific fundamentals and technological applications*. Springer Science & Business Media, 2013.

[27] World Energy Council. World Energy Scenarios 2017. Available online: `https://www.worldenergy.org/wp-content/uploads/2017/03/LAC-Scenarios_summary-report_English_WEB_2017.05.25.pdf`. Accessed on 30/10/2018.

[28] Pekik Argo Dahono and Diah P. Wulandari. Low-frequency output current ripple minimization by using virtual inductor active ripple energy storage. In *Int. Conf. on Power Electronics and Drive Systems (PEDS)*, Kuala Lumpur, November 2005. IEEE.

[29] Samuel Davoust, Alban Jehu, Michael Bouillet, Mathieu Bardon, Benoist Vercherin, Andrew Scholbrock, Paul Fleming, and Alan Wright. Assessment and optimization of lidar measurement availability for wind turbine control. In *Scientific. Proceedings of EWEA Conference March*, pages 10–13, Barcelona, Spain, March 2014.

[30] FP Demello, RJ Koessler, J Agee, PM Anderson, JH Doudna, JH Fish, PAL Hamm, P Kundur, DC Lee, GJ Rogers, et al. Hydraulic-turbine and turbine control-models for system dynamic studies. *IEEE Transactions on Power Systems*, 7(1):167–179, 1992.

[31] Francisco Díaz-González, Andreas Sumper, Oriol Gomis-Bellmunt, and Roberto Villafáfila-Robles. A review of energy storage technologies for wind power applications. *Renewable and sustainable energy reviews*, 16(4):2154–2171, 2012.

[32] Francisco Díaz-González, Melanie Hau, Andreas Sumper, and Oriol Gomis-Bellmunt. Participation of wind power plants in system frequency control: Review of grid code requirements and control methods. *Renewable and Sustainable Energy Reviews*, 34:551–564, 2014.

[33] KC Divya and Jacob Østergaard. Battery energy storage technology for power systems – An overview. *Electric power systems research*, 79(4):511–520, 2009.

[34] John C Doyle. Lecture notes in advances in multivariable control. In *ONR/Honeywell workshop*, 1984.

[35] Mohammad Dreidy, H Mokhlis, and Saad Mekhilef. Inertia response and frequency control techniques for renewable energy sources: A review. *Renewable and Sustainable Energy Reviews*, 69:144–155, 2017.

[36] F Dunne, E Simley, and Lucy Y Pao. Lidar wind speed measurement analysis and feed-forward blade pitch control for load mitigation in wind turbines: January 2010–january 2011. Technical report, National Renewable Energy Lab.(NREL), Golden, CO (United States), 2011.

[37] Rahul Dutta. Modeling and analysis of short term energy storage for mid-size hydrostatic wind turbine, Master thesis, University of Minnesota. 2012.

[38] Rahul Dutta, Feng Wang, Bradley F Bohlmann, and Kim A Stelson. Analysis of short-term energy storage for midsize hydrostatic wind turbine. *Journal of Dynamic Systems, Measurement, and Control*, 136(1):011007, 2014.

[39] Christopher Edwards and Sarah Spurgeon. *Sliding mode control: theory and applications*. CRC Press, 1998.

[40] Omar Ellabban, Haitham Abu-Rub, and Frede Blaabjerg. Renewable energy resources: Current status, future prospects and their enabling technology. *Renewable and Sustainable Energy Reviews*, 39:748–764, 2014.

[41] GlobalData Energy. Renewable energy to reach 22.5 Available online: `https://www.power-technology.com/comment/renewable-energy-reach-22-5-share-global-power-mix-2020/`. Accessed on 30/10/2018.

[42] ERC for Compact and Efficient Fluid Power. Hydrostatic Transmission to Improve Cost Efficiency and Power Reliability of Wind Power. Available online: `http://erc-assoc.org/content/hydrostatic-transmission-improve-cost-efficiency-and-power-reliability-wind-power`. Accessed on 30/10/2018.

[43] Paolo Fornasiero and Mauro Graziani. *Renewable resources and renewable energy: a global challenge*. CRC Press, 2011.

[44] Wenzhong Gao, Ziping Wu, Jianhui Wang, and Shusheng Gu. A review of inertia and frequency control technologies for variable speed wind turbines. In *25th Chinese Control and Decision Conference (CCDC)*, pages 2527–2533, Guiyang, China, May 2013. IEEE.

[45] Anthony Gee, Francis VP Robinson, and Roderick W Dunn. Sliding-mode control, dynamic assessment and practical implementation of a bidirectional buck/boost DC-to-DC converter. In *14th European Conference on Power Electronics and Applications (EPE 2011)*, pages 1–10, Birmingham, UK, August 2011. IEEE.

[46] Global Wind Energy Council. Global Wind Report, Annual Market Update 2017. Available online: `http://files.gwec.net/files/GWR2017.pdf`. Accessed on 07/10/2018.

[47] Global Wind Energy Council. Offshore Wind. Available online: `http://gwec.net/wp-content/uploads/2018/04/offshore.pdf`. Accessed on 30/10/2018.

[48] Keith Glover and Duncan McFarlane. Robust stabilization of normalized coprime factors: An explicit H_∞ solution. In *American Control Conference*, pages 842–847, Atlanta, USA, June 1988. IEEE.

[49] Keith Glover and Duncan McFarlane. Robust stabilization of normalized coprime factor plant descriptions with H_∞-bounded uncertainty. *IEEE transactions on automatic control*, 34(8):821–830, 1989.

[50] Ioannis Hadjipaschalis, Andreas Poullikkas, and Venizelos Efthimiou. Overview of current and future energy storage technologies for electric power applications. *Renewable and sustainable energy reviews*, 13(6-7):1513–1522, 2009.

[51] Michael Harris, Maureen Hand, and A Wright. Lidar for Turbine Control. Technical report, National Renewable Energy Laboratory, Golden, CO, No. NREL/TP-500-39154, 2006.

[52] Erich Hau and Horst von Renouard. *Wind turbines: fundamentals, technologies, application, economics*. Springer, 2003.

[53] G. J. Hayman. Mlife theory manual for version 1.00. Technical report, National Renewable Energy Laboratory (NREL), Golden, CO., 2012.

[54] G. J. Hayman and Jr M. Buhl. Mlife user's guide for version 1.00. Technical report, National Renewable Energy Laboratory (NREL), Golden, CO., 2012.

[55] Yongxiu He, Yang Xu, Yuexia Pang, Huiying Tian, and Rui Wu. A regulatory policy to promote renewable energy consumption in China: review and future evolutionary path. *Renewable Energy*, 89:695–705, 2016.

[56] GM Joselin Herbert, Selvaraj Iniyan, E Sreevalsan, and S Rajapandian. A review of wind energy technologies. *Renewable and sustainable energy Reviews*, 11(6): 1117–1145, 2007.

[57] Zhongsheng Hou and Shangtai Jin. A novel data-driven control approach for a class of discrete-time nonlinear systems. *IEEE Transactions on Control Systems Technology*, 19(6):1549–1558, 2011.

[58] Zhongsheng Hou and Shangtai Jin. Data-driven model-free adaptive control for a class of MIMO nonlinear discrete-time systems. *IEEE Transactions on Neural Networks*, 22(12):2173–2188, 2011.

[59] Zhongsheng Hou and Shangtai Jin. *Model free adaptive control: theory and applications*. CRC Press, 2013.

[60] Zhongsheng Hou, Ronghu Chi, and Huijun Gao. An overview of dynamic-linearization-based data-driven control and applications. *IEEE Transactions on Industrial Electronics*, 64(5):4076–4090, 2017.

[61] Haibing Hu, Souhib Harb, Nasser Kutkut, Issa Batarseh, and Z John Shen. A review of power decoupling techniques for microinverters with three different decoupling capacitor locations in PV systems. *IEEE Transactions on Power Electronics*, 28(6):2711–2726, 2013.

[62] Y. Hu, Z.Q. Zhu, and M. Odavic. An improved control strategy of limiting the DC-link voltage fluctuation for a doubly fed induction wind generator. *IEEE Transactions Energy Conversion*, 32:1231–1239, 2017.

[63] Hui Huang, Chengxiong Mao, Jiming Lu, and D Wang. Small-signal modelling and analysis of wind turbine with direct drive permanent magnet synchronous generator connected to power grid. *IET Renewable Power Generation*, 6(1):48–58, 2012.

[64] DA Hullender. Model representation for fluid transmission line dynamics. In *International Symposium on Fluid Control and Measurement, SICE, Tokyo, Japan*, page 93, 1985.

[65] Hussein Ibrahim, Adrian Ilinca, and Jean Perron. Energy storage systems – characteristics and comparisons. *Renewable and sustainable energy reviews*, 12(5): 1221–1250, 2008.

[66] American Geosciences Institute. What are the advantages and disadvantages of offshore wind farms? Available online: `https://www.americangeosciences.org/critical-issues/faq/what-are-advantages-and-disadvantages-offshore-wind-farms`. Accessed on 30/10/2018.

[67] International Energy Agency. World Energy Outlook 2012: Executive Summary. Available online: `https://www.iea.org/publications/freepublications/publication/English.pdf`, . Accessed on 09/11/2018.

[68] International Energy Agency. World Energy Outlook 2017: Executive Summary. Available online: `https://www.iea.org/publications/freepublications/publication/WEO_2017_Executive_Summary_English_version.pdf`, . Accessed on 30/10/2018.

[69] Kathryn E Johnson, Lucy Y Pao, Mark J Balas, and Lee J Fingersh. Control of variable-speed wind turbines: standard and adaptive techniques for maximizing energy capture. *IEEE control systems*, 26(3):70–81, 2006.

[70] Bonnie J Jonkman. TurbSim user's guide: Version 1.50. Technical report, National Renewable Energy Laboratory, CO, USA, 2009.

[71] Jason Jonkman, Sandy Butterfield, Walter Musial, and George Scott. Definition of a 5-MW reference wind turbine for offshore system development. Technical report, National Renewable Energy Laboratory, Golden, CO, No. NREL/TP-500-38060, 2009.

[72] Jason M. Jonkman and Marshall L. Buhl Jr. Fast user's guide. Technical report, National Renewable Energy Laboratory, Golden, CO, No. NREL/EL-500-38230, 2005.

[73] J.G. Kassakian, M.F. Schlecht, and G.C. vVerghese. *Principles of Power Electronics*. MA: Addison-Wesley, 1992.

[74] Steven Keeping. A review of Zero-Voltage Switching and its Importance to Voltage Regulation. Available online: `http://www.digikey.co.uk/en/articles/techzone/2014/aug/a-review-of-zero-voltage-switching-and-its-importance-to-voltage-regulation`. Accessed on 05/08/2014.

[75] R Kötz and M Carlen. Principles and applications of electrochemical capacitors. *Electrochimica acta*, 45(15-16):2483–2498, 2000.

[76] Prabha Kundur, Neal J Balu, and Mark G Lauby. *Power system stability and control*, volume 7. McGraw-hill New York, 1994.

[77] Antonio Jarquin Laguna. Modeling and analysis of an offshore wind turbine with fluid power transmission for centralized electricity generation. *Journal of Computational and Nonlinear dynamics*, 10(4):041002, 2015.

[78] VX Le and MG Safonov. Rational matrix GCDs and the design of squaring-down compensators – a state-space theory. *IEEE Transactions on Automatic Control*, 37(3):384–392, 1992.

[79] AE Leon, JA Solsona, and Maria Ines Valla. Comparison among nonlinear excitation control strategies used for damping power system oscillations. *Energy Conversion and Management*, 53(1):55–67, 2012.

[80] Jiaqi Liang, Santiago Grijalva, and Ronald G Harley. Increased wind revenue and system security by trading wind power in energy and regulation reserve markets. *IEEE Transactions on Sustainable Energy*, 2(3):340–347, 2011.

[81] Jun Lin and George Weiss. Plug-and-play realization of the virtual infinite capacitor. In *2017 International Symposium on Power Electronics (Ee)*, pages 1–6, Novi Sad, Serbia, October 2017. IEEE.

[82] Shuyue Lin, Jun Lin, George Weiss, and Xiaowei Zhao. Control of a virtual infinite capacitor used to stabilize the output voltage of a PFC. In *IEEE International Conference on the Science of Electrical Engineering (ICSEE)*, pages 1–5, Eilat,Israel, November 2016. IEEE.

[83] Shuyue Lin, Pengyuan Qi, Jun Lin, Xiaowei Zhao, George Weiss, and Li Ran. Experimental Ripple Suppression Performance of a Virtual Infinite Capacitor. In *2017 22nd International Conference on Applied Electronics (AE)*, Pilsen, Czech Republic, September 2017. IEEE.

[84] Shuyue Lin, Pengyuan Qi, and Xiaowei Zhao. Power generation control of a hydrostatic wind turbine implemented by model-free adaptive control scheme. under review, 2018.

[85] Shuyue Lin, Xin Tong, Xiaowei Zhao, and George Weiss. The Parallel Virtual Infinite Capacitor Applied to DC-link Voltage Filtering for Wind Turbines. *Energies*, 11(7):1649, 2018.

[86] Shuyue Lin, Xin Tong, Xiaowei Zhao, and George Weiss. Application of a parallel virtual infinite capacitor to dc-link voltage filtering for a doubly fed induction wind generator. In *2018 IEEE International Conference on Environment and Electrical Engineering and 2018 IEEE Industrial and Commercial Power Systems Europe (EEEIC/I&CPS Europe)*, pages 1–6, Palermo, Italy, June 2018. IEEE.

[87] Shuyue Lin, Xiaowei Zhao, and Xin Tong. Feasibility Studies of a Converter-free Grid-connected Hydrostatic Wind Turbine. under review, 2018.

[88] Chao Lu, Yi Zhao, Kun Men, Liang Tu, and Yingduo Han. Wide-area power system stabiliser based on model-free adaptive control. *IET Control Theory & Applications*, 9(13):1996–2007, 2015.

[89] XP Lu, W Li, and YG Lin. Load control of wind turbine based on model-free adaptive controller. *Transactions of Chinese Society for Agricultural Machinery*, 10:109–119, 2011.

[90] Jari Mäkinen, Robert Piche, and Asko Ellman. Fluid transmission line modeling using a variational method. *Journal of dynamic systems, measurement, and control*, 122(1):153–162, 2000.

[91] DJ Malcolm and AC Hansen. WindPACT turbine rotor design study: June 2000–june 2002 (revised). Technical report, National Renewable Energy Laboratory (NREL), Golden, CO., 2006.

[92] Marine Renewables Infrastructure Network. Collation of European grid codes. Technical report, 2013.

[93] Denis Matha. Model development and loads analysis of an offshore wind turbine on a tension leg platform with a comparison to other floating turbine concepts: April 2009. Technical report, National Renewable Energy Lab.(NREL), Golden, CO (United States), 2010.

[94] De MeFarlane and K Glover. A loop shaping design procedure using H_∞ synthesis. *IEEE Transactions on Automatic Control*, 37(6):759–769, 1992.

[95] Lu Miao, Jinyu Wen, Hailian Xie, Chengyan Yue, and Wei-Jen Lee. Coordinated control strategy of wind turbine generator and energy storage equipment for frequency support. *IEEE Transactions on Industry Applications*, 51(4):2732–2742, 2015.

[96] Nicholas W Miller, William W Price, and Juan J Sanchez-Gasca. Dynamic modeling of GE 1.5 and 3.6 wind turbine-generators. Technical report, GE-Power Systems Energy Consulting,General Electric International, Inc., USA, 2003.

[97] N.W. Miller, J.J. Sanchez-Gasca, W.W. Price, and R.W. Delmerico. Dynamic modeling of GE 1.5 and 3.6 MW wind turbine generators for stability simulations. In *2003 IEEE Power Engineering Society General Meeting*, Toronto, ON, Canada, July 2003. IEEE.

[98] J Mohammadi, S Afsharnia, and S Vaez-Zadeh. Efficient fault-ride-through control strategy of DFIG-based wind turbines during the grid faults. *Energy conversion and management*, 78:88–95, 2014.

[99] Johan Morren, Sjoerd WH De Haan, Wil L Kling, and JA Ferreira. Wind turbines emulating inertia and supporting primary frequency control. *IEEE Transactions on power systems*, 21(1):433–434, 2006.

[100] Jennifer F Newman, Andrew Clifton, Matthew J Churchfield, and Petra Klein. Improving lidar turbulence estimates for wind energy. *Journal of Physics: Conference Series*, 753(7):072010, 2016.

[101] Yu Ni, Saad Pervaiz, Minjie Chen, and Khurram K Afridi. Energy density enhancement of stacked switched capacitor energy buffers through capacitance ratio optimization. *IEEE Transactions on Power Electronics*, 32(8):6363–6380, 2017.

[102] Michael Kenward OBE. Bringing electronic control to hydraulic. Available online: `https://www.ingenia.org.uk/getattachment/Ingenia/Issue-64/Bringing-electronic-controls-to-hydraulics/caldwell.pdf`. Accessed on 30/10/2018.

[103] Bereau of Ocean Energy Management. Offshore Wind Energy. Available online: `https://www.boem.gov/Renewable-Energy-Program/Renewable-Energy-Guide/Offshore-Wind-Energy.aspx`. Accessed on 30/10/2018.

[104] X.F.S. Onge, K. McDonald, C. Richard, and S.A. Saleh. A new multi-port active DC-link for PMG-based WECSs. In *IEEE/IAS 54th Industrial and Commercial Power Systems Technical Conference (I&CPS)*, Niagara Falls, ON, Canada, May 2018. IEEE.

[105] Jean-Claude Ossyra. Reliable, lightweight transmissions for off-shore, utility scale wind turbines. Technical report, Eaton Corporation, 2012.

[106] Wilfrid Perruquetti and Jean-Pierre Barbot. *Sliding mode control in engineering*. CRC Press, 2002.

[107] Saad Pervaiz, Yu Ni, Minjie Chen, and Khurram K. Afridi. An electrolytic-free offline LED driver with a ceramic-capacitor-based compact stacked switched capacitor (SSC) energy buffer using virtual inductor active ripple energy storage. In *Energy Conversion Congress and Exposition (ECCE)*, Pittsburgh, PA, September 2014. IEEE.

[108] V Peters, A Ogilvie, and C Bond. Crew database: Wind plant reliability benchmark. *SAND 2012–7328*, 2012.

[109] L Pettersson, JO Andersson, C Orbert, and S Skagerman. RAMS-database for wind turbines: Pre-study. *Elforsk report*, 10:67, 2010.

[110] IG Piña Rodriguez. Hydraulic drivetrains for wind turbines: Radial piston digital machines, Master thesis, Delft University of Technology. 2012.

[111] Henk Polinder, Frank FA Van der Pijl, G-J De Vilder, and Peter J Tavner. Comparison of direct-drive and geared generator concepts for wind turbines. *IEEE Transactions on energy conversion*, 21(3):725–733, 2006.

[112] Henk Polinder, Jan Abraham Ferreira, Bogi Bech Jensen, Asger B Abrahamsen, Kais Atallah, and Richard A McMahon. Trends in wind turbine generator systems. *IEEE Journal of emerging and selected topics in power electronics*, 1(3):174–185, 2013.

[113] Wind Power Program. The Betz limit - and the maximum efficiency for horizontal axis wind turbines. Available online: `http://www.wind-power-program.com/betz.htm`. Accessed on 30/10/2018.

[114] Shibin Qin, Yutian Lei, Christopher Barth, Wen-Chuen Liu, and Robert C.N. Pilawa-Podgurski. Architecture and control of a high energy density buffer for power pulsation decoupling in grid-interfaced applications. In *16th IEEE Workshop on Control and Modeling for Power Electronics (COMPEL)*, Vancouver, Canada, July 2015. IEEE.

[115] Shibin Qin, Yutian Lei, Christopher Barth, Wen-Chuen Liu, and Robert CN Pilawa-Podgurski. A high power density series-stacked energy buffer for power pulsation decoupling in single-phase converters. *IEEE Transactions on Power Electronics*, 32(6):4905–4924, 2017.

[116] Danop Rajabhandharaks. Control of hydrostatic transmission wind turbine, Master thesis, San Jose State University. 2014.

[117] Win Rampen et al. Gearless transmissions of large wind turbines-the history and future of hydraulic drives. *Artemis IP Ltd., Midlothian, UK*, 2006.

[118] Joel Rapp and Jonatan Turesson. Hydrostatic transmission in wind turbines: Development of test platform, Master thesis, Linköping University. 2015.

[119] Johan Ribrant and Lina Bertling. Survey of failures in wind power systems with focus on swedish wind power plants during 1997-2005. In *Power Engineering Society General Meeting, 2007. IEEE*, pages 1–8, Tampa, USA, June 2007. IEEE.

[120] J. Rinker and K. Dykes. WindPACT Reference Wind Turbines, National Renewable Energy Laboratory (NREL): Golden, CO, USA, 2018. Available online: `https://www.nrel.gov/docs/fy18osti/67667.pdf`. Accessed on 30/10/2018.

[121] S Rodrigues, C Restrepo, E Kontos, R Teixeira Pinto, and P Bauer. Trends of offshore wind projects. *Renewable and Sustainable Energy Reviews*, 49:1114–1135, 2015.

[122] TK Roy, MA Mahmud, Weixiang Shen, and AMT Oo. Nonlinear excitation control of synchronous generators based on adaptive backstepping method. In *Industrial Electronics and Applications (ICIEA), 2015 IEEE 10th Conference on*, pages 11–16, Auckland, New Zealand, June 2015. IEEE.

[123] SC Rybak. Description of the 3 MW SWT-3 wind turbine at San Gorgonio Pass, California. *NASA. Lewis Research Center Large Horizontal-Axis Wind Turbines*, pages 575–588, 1982.

[124] David Schlipf, Po Wen Cheng, and Jakob Mann. Model of the correlation between Lidar systems and wind turbines for Lidar-assisted control. *Journal of Atmospheric and Oceanic Technology*, 30(10):2233–2240, 2013.

[125] David Schlipf, Eric Simley, Frank Lemmer, Lucy Pao, and Po Wen Cheng. Collective pitch feedforward control of floating wind turbines using Lidar. In *Proceedings of the 25th (2015) International Ocean and Polar Engineering Conference*, pages 324–331, Hawaii, USA, June 2015. International Society of Offshore and Polar Engineers (ISOPE).

[126] Shahaboddin Shamshirband, Dalibor Petković, Amineh Amini, Nor Badrul Anuar, Vlastimir Nikolić, Žarko Ćojbašić, Miss Laiha Mat Kiah, and Abdullah Gani. Support vector regression methodology for wind turbine reaction torque prediction with power-split hydrostatic continuous variable transmission. *Energy*, 67:623–630, 2014.

[127] Shuangwen Sheng. Report on wind turbine subsystem reliability—a survey of various databases. Technical report, National Renewable Energy Laboratory, Golden, CO, No. NREL/PR-5000-59111, 2013.

[128] Paolo Silva, Antonio Giuffrida, Nicola Fergnani, Ennio Macchi, Matteo Cantù, Roberto Suffredini, Massimo Schiavetti, and Gianluca Gigliucci. Performance pre-

diction of a multi-MW wind turbine adopting an advanced hydrostatic transmission. *Energy*, 64:450–461, 2014.

[129] Mohit Singh, E Muljadi, J Jonkman, V Gevorgian, I Girsang, and J Dhupia. Simulation for wind turbine generators—with FAST and MATLAB-simulink modules. Technical report, National Renewable Energy Laboratory, Golden, CO, No. NREL/TP-5D00-59195, 2014.

[130] Bjørn Skaare, Bo Hörnsten, and Finn Gunnar Nielsen. Modeling, simulation and control of a wind turbine with a hydraulic transmission system. *Wind Energy*, 16 (8):1259–1276, 2013.

[131] IEEE Power Engineering Society. Recommended practice for excitation system models for power system stability studies. *IEEE Std 421.5-1992*, 1992.

[132] David A. Spera. *Wind turbines technology: fundamental concepts of wind turbine engineering,second edition*. ASME, 2009.

[133] F Spinato, Peter J Tavner, GJW Van Bussel, and E Koutoulakos. Reliability of wind turbine subassemblies. *IET Renewable Power Generation*, 3(4):387–401, 2009.

[134] Jacek S Stecki and DC Davis. Fluid transmission lines—distributed parameter models part 2: Comparison of models. *Proceedings of the institution of mechanical engineers, part a: power and process engineering*, 200(4):229–236, 1986.

[135] Daniel-Ioan Stroe, Vaclav Knap, Maciej Swierczynski, Ana-Irina Stroe, and Remus Teodorescu. Operation of a grid-connected lithium-ion battery energy storage system for primary frequency regulation: A battery lifetime perspective. *IEEE transactions on industry applications*, 53(1):430–438, 2017.

[136] Yao Sun, Yonglu Liu, Mei Su, Wenjing Xiong, and Jian Yang. Review of active power decoupling topologies in single-phase systems. *IEEE Transactions on Power Electronics*, 31(7):4778–4794, 2016.

[137] Herbert J Sutherland. On the fatigue analysis of wind turbines. Technical report, Sandia National Labs., Albuquerque, NM (US); Sandia National Labs., Livermore, CA (US), 1999.

[138] Siew-Chong Tan, Yuk-Ming Lai, and Chi Kong Tse. General design issues of sliding-mode controllers in DC-DC converters. *IEEE Transactions on Industrial Electronics*, 55(3):1160–1174, 2008.

[139] Siew-Chong Tan, Yuk-Ming Lai, and Chi-Kong Tse. *Sliding mode control of switching power converters: techniques and implementation*. CRC Press, 2011.

[140] P Tavner. How are we going to make offshore wind farms more reliable? In *2011 SUPERGEN Wind General Assembly*, Durham University, United Kingdom, March 2011.

[141] PJ Tavner, Fabio Spinato, GJW Van Bussel, and Efstathios Koutoulakos. Reliability of different wind turbine concepts with relevance to offshore application. In *Proceedings of European Wind Energy Conference, Brussels, Belgium, March*, Mar. 2008.

[142] Jamie TAYLOR, Win RAMPEN, Alasdair ROBERTSON, and Niall CALDWELL. Digital displacement® hydraulic hybrids. In *Presented at the JSAE Annual Congress on*, 2011.

[143] Infineon Technologies. CoolMOS benefits in both hard and soft switching SMPS topologies, Infineon product description. Available online: `https://www.infineon.com/dgdl/Infineon-ProductBrochure_CoolMOS_Benefits_in_Hard_Soft_Switching-BC-v07_01-EN.pdf?fileId=db3a3043338c8ac80133aca62ba63047`. Accessed on 05/08/2014.

[144] Xin Tong and Xiaowei Zhao. Power generation control of a monopile hydrostatic wind turbine using an H_∞ loop-shaping torque controller and an LPV pitch controller. *IEEE Transactions on Control Systems Technology*, 26(6), 2018.

[145] Maria Lorena Tuballa and Michael Lochinvar Abundo. A review of the development of Smart Grid technologies. *Renewable and Sustainable Energy Reviews*, 59: 710–725, 2016.

[146] John Twidell and Tony Weir. *Renewable energy resources*. Routledge, 2015.

[147] Vadim Utkin. Variable structure systems with sliding modes. *IEEE Transactions on Automatic control*, 22(2):212–222, 1977.

[148] Vadim Utkin, Jürgen Guldner, and Jingxin Shi. *Sliding mode control in electromechanical systems*. CRC Press, 2009.

[149] M Vidyasagar and H Kimura. Robust controllers for uncertain linear multivariable systems. *Automatica*, 22(1):85–94, 1986.

[150] Rong-Jong Wai and Li-Chung Shih. Design of voltage tracking control for DC-DC boost converter via total sliding-mode technique. *IEEE Transactions on Industrial Electronics*, 58(6):2502–2511, 2011.

[151] Feng Wang and Kim A Stelson. Model predictive control for power optimization in a hydrostatic wind turbine. In *13th Scandinavian International Conference on Fluid Power*, number 092, pages 155–160, Linköping; Sweden, June 2013. Linköping University Electronic Press.

[152] Ruxi Wang, Fred Wang, Dushan Boroyevich, Rolando Burgos, Rixin Lai, Puqi Ning, and Kaushik Rajashekara. A high power density single-phase PWM rectifier with active ripple energy storage. *IEEE Transactions on Power Electronics*, 26 (5):1430–1443, 2011.

[153] Siying Wang, Jiabing Hu, Shuo Wang, Haiyan Tang, and Yongning Chi. Comparative study on primary frequency control schemes for variable-speed wind turbines. *The Journal of Engineering*, 2017(13):1332–1337, 2017.

[154] Ye Wang, Gauthier Delille, Herman Bayem, Xavier Guillaud, and Bruno Francois. High wind power penetration in isolated power systems — assessment of wind inertial and primary frequency responses. *IEEE Transactions on Power Systems*, 28(3):2412–2420, 2013.

[155] Felipe Wilches-Bernal, Joe H Chow, and Juan J Sanchez-Gasca. A fundamental study of applying wind turbines for power system frequency control. *IEEE Transactions on Power Systems*, 31(2):1496–1505, 2016.

[156] M Wilkinson, B Hendriks, and P Tavner. Report on wind turbine reliability profiles. *GL-GH for Reliawind FP7-ENERGY-2007-1-RTD Deliverable D-1*, 3, 2011.

[157] U.S. Department of Energy Wind Energy Technologies Office. Advantages and Challenges of Wind Energy. Available online: `https://www.energy.gov/eere/wind/advantages-and-challenges-wind-energy`. Accessed on 30/10/2018.

[158] World Wind Energy Association. Wind Power Capacity Reaches 539GW, 52.6GW Added in 2017. Available online: `http://www.wwindea.org/2017-statistics/`. Accessed on 07/10/2018.

[159] Allan D Wright and LJ Fingersh. Advanced control design for wind turbines; part i: control design, implementation, and initial tests. Technical report, National Renewable Energy Lab.(NREL), Golden, CO (United States), 2008.

[160] Yinglai Xia and Raja Ayyanar. Adaptive DC link voltage control scheme for single phase inverters with dynamic power decoupling. In *2016 IEEE Energy Conversion Congress and Exposition (ECCE)*, pages 1–7, Milwaukee, WI, USA, September 2016. IEEE.

[161] Jun Yao, Hui Li, Yong Liao, and Zhe Chen. An improved control strategy of limiting the DC-link voltage fluctuation for a doubly fed induction wind generator. *IEEE transactions on power electronics*, 23(3):1205–1213, 2008.

[162] Guy Yona and George Weiss. Zero-voltage switching implementation of a virtual infinite capacitor. In *2015 IEEE 5th International Conference on Power Engineering, Energy and Electrical Drives (POWERENG)*, pages 157–163, Riga, Latvia, May 2015. IEEE.

[163] Guy Yona and George Weiss. The virtual infinite capacitor. *International Journal of Control*, 90(1):78–89, 2017.

[164] Hassan A Yousef, Mohamed Hamdy, and Muhammad Shafiq. Flatness-based adaptive fuzzy output tracking excitation control for power system generators. *Journal of the Franklin Institute*, 350(8):2334–2353, 2013.

[165] Huaguang Zhang, Jianguo Zhou, Qiuye Sun, Josep M Guerrero, and Dazhong Ma. Data-driven control for interlinked AC/DC microgrids via model-free adaptive control and dual-droop control. *IEEE Transactions on Smart Grid*, 8(2):557–571, 2017.

[166] Haoran Zhao, Qiuwei Wu, Shuju Hu, Honghua Xu, and Claus Nygaard Rasmussen. Review of energy storage system for wind power integration support. *Applied Energy*, 137:545–553, 2015.

[167] Qing-Chang Zhong, Wen-Long Ming, Xin Cao, and Miroslav Krstic. Reduction of DC-bus voltage ripples and capacitors for single-phase PWM-controlled rectifiers. In *IECON 2012-38th Annual Conference on IEEE Industrial Electronics Society*, pages 708–713, Montreal, QC, Canada, October 2012. IEEE.

[168] Qing-Chang Zhong, Wen-Long Ming, Xin Cao, and Miroslav Krstic. Control of ripple eliminators to improve the power quality of dc systems and reduce the usage of electrolytic capacitors. *IEEE Access*, 4:2177–2187, 2016.

Appendix A: Schematic Diagram of VIC PCB Design

Grid connection and relay

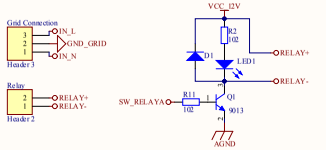

i_g sensor

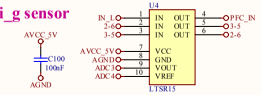

PFC connection header

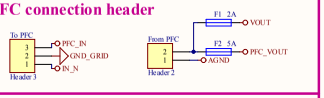

Voltage regulators

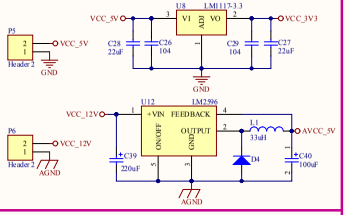

Isolated DC-DC converter for current sensors

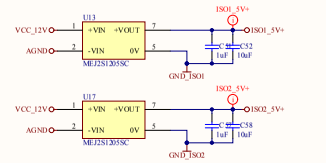

Ground isolation

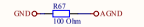

Reference voltage generators

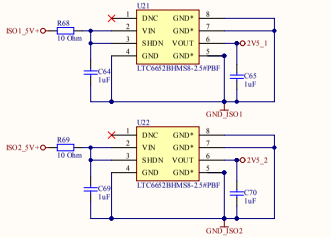

Current/voltage sensors

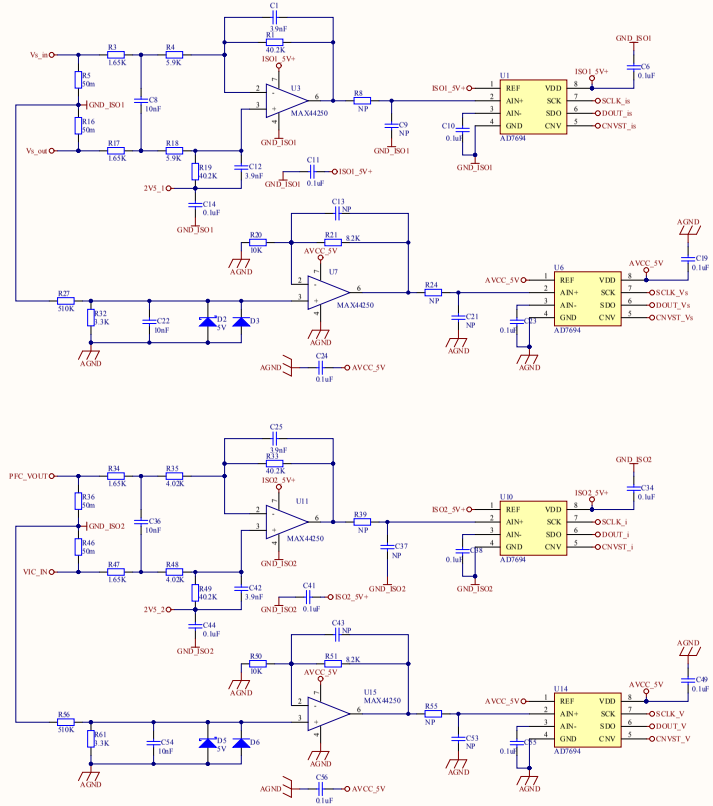

VIC circuit

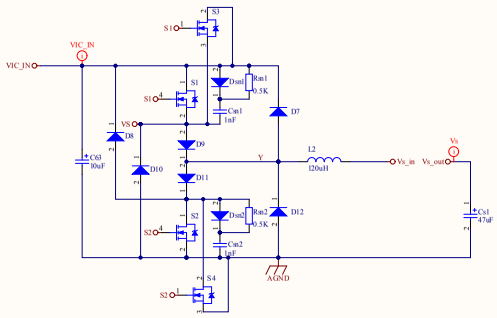

Measurement signal isolation

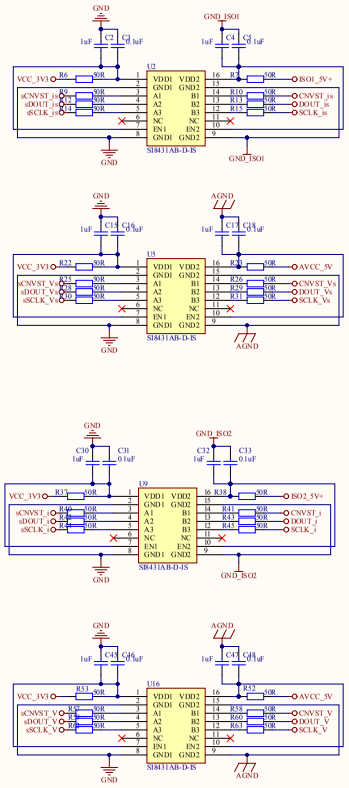

Relay/ VIC switch signal isolation

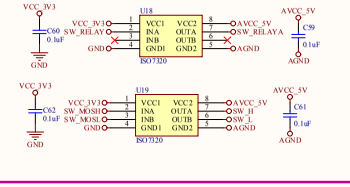

VIC switch driver

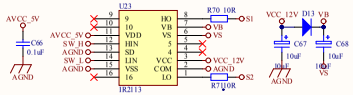

DSP connection (Concerto)

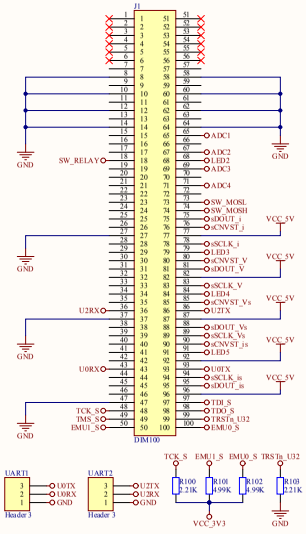

Fault/power on indicate LED

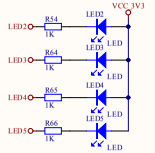

i_out sensor and Load connection

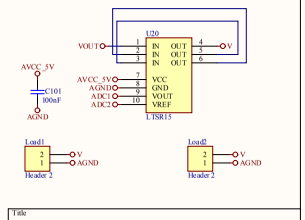

Title		
Size	Number	Revision
A2		
Date:	05/09/2017	Sheet of
File:	E:\your 2...\vic.SchDoc	Drawn By:

Appendix B: Fatigue estimations — MLife

Fatigue estimations — MLife

We now introduce the detailed estimation theory for the short-term damage-equivalent load (DEL), which is a constant-amplitude fatigue loads that occurs at a fixed load-mean and frequency and produces the equivalent damage as the variable spectrum loads [53]. The loads are broken down into individual hysteresis cycles which is characterised by load mean and load range. It is implemented by matching the local minima with local maxima in time series. The i-th cycle load range L_i^{RF} is

$$L_i^{RF} = L_i^R \left(\frac{L^{ult} - \left| L^{MF} \right|}{L^{ult} - \left| L_i^M \right|} \right), \tag{1}$$

where L^{ult} is the ultimate design load of the component, L^{MF} is the fixed load mean, L_i^M is the i-th cycle load mean and L_i^R is the i-th cycle load range [53]. The ultimate design load of the component L^{ult} is the product of ultimate load factor (ULF) and the maxima in time series.

The MLife will bin the individual cycle counts according to the load range. The number of range bins n^R is defined by users to compute the width of each bin Δ^R:

$$\Delta^R = \frac{L_{max}^R}{n^R}, \tag{2}$$

where L_{max}^R is the maximum load range in rainflow cycles across all input time series. Note that it is also applicable to select the maximum width of each range bin Δ_{max}^R and

then compute the number of bins by

$$n^R = \left\lceil \frac{L^R_{max}}{\Delta^R_{max}} \right\rceil, \tag{3}$$

where $\lceil \cdot \rceil$ denotes the ceiling function. It maps the input to the least integer which equals to or larger than the input.

The load bin k is defined as the ceiling function of the load range value L^{RF}_{ji} over the number of range bins n^R for the i-th cycle in j-th time series:

$$k = \left\lceil \frac{L^R_{ji}}{\Delta^R} \right\rceil, \tag{4}$$

and the value of the load range for bin k is defined as

$$L^R_k = (k - 0.5)\Delta^R. \tag{5}$$

Then, the binned short-term damage-equivalent load DEL^{ST}_j is defined as

$$\mathrm{DEL}^{ST}_j = \left(\frac{\sum_k (n^F_{jk} (L^R_k)^m)}{n^{STeq}_j} \right)^{\frac{1}{m}}, \tag{6}$$

in which

$$n^{STeq}_j = f^{eq} T_j. \tag{7}$$

f^{eq} is the DEL frequency, T_j is the elapsed time of the time series j, n^{STeq}_j is the total equivalent fatigue counts for time series j, and n^F_{jk} is the total number of cycle counts from time series j whose load range L^{RF}_i falls into bin k.